New Materials for Chalcogenide Based Solar Cells

A THESIS
SUBMITTED TO THE FACULTY OF
UNIVERSITY OF MINNESOTA
BY

Banu Selin Tosun

IN PARTIAL FULFULLMENT OF THE
REQUIREMENTS FOR THE DEGREE OF
DOCTOR OF PHILOSOPHY

Adviser: Eray S. Aydil

June, 2013

ACKNOWLEDGEMENTS

First and foremost, I would like to thank to my adviser, Eray S. Aydil, not only for his invaluable guidance in science, but also for his encouragement. I am very grateful for his assistance and patience through the course of my graduate years. As previously said, Eray has perfected the art of being an adviser and he is a great role model both professionally and personally.

I would also like to thank all the Aydil group members. Particularly, I am grateful for Dr. Ankur Khare, Melissa Johnson, Boris Chernomordik, Brian Meritt, Xin Zhang, Jonathan Hubbard, Dr. Micheal Manno, Dr. Joel Abrahamson, and Dr. Elijah Thimsen for their invaluable help in my research and for all the fruitful discussions. I am also very thankful to remaining group members Sriharsha Jayanti, Dr. Rebecca Anthony, Nancy Trejo, and Elliot Combs for creating such a lively and enjoyable workplace. In addition, I would like to thank to my friend and collaborator, Aloysius A. Gunawan, for his efforts with the transmission electron microscope. It has been a great pleasure to work with you all.

I am very grateful to committee Prof. Stephen A. Campbell, Prof. K. Andre Mkhoyan, and Prof. Chris Leighton for their scientific and professional advice, and research opportunities they provided.

I also would like to thank to Burak Himmetoglu, for his never-ending moral support and physics tutoring when I needed through this journey in graduate school. I am very grateful for all my friends, especially the ones in Minnesota for all their support and making life so enjoyable. Finally, I would like to thank my family; my mom for flying to Minneapolis many times without any hesitation; my grandma for her constant love; my aunts and uncles for their constant support. Without them, I would not be where I am today.

To my Family

ABSTRACT

Thin film solar cells based on copper indium gallium diselenide (CIGS) have achieved efficiencies exceeding 20 %. The p-n junction in these solar cells is formed between a p-type CIGS absorber layer and a composite n-type film that consists of a 50-100 nm thin n-type CdS followed by a 50-200 nm thin n-type ZnO. This dissertation focuses on developing materials for replacing CdS, ZnO and CIGS films for minimizing the use of Cd, to improve the damp-heat stability of the solar cells, and to develop environmentally benign solar absorber materials.

Specifically, I demonstrate a new CIGS solar cell with better damp heat stability wherein the ZnO layer is replaced with SnO_2. The efficiency of solar cells made with SnO_2 decreased less than 5 % after 120 hours at 85 ^{o}C and 85 % relative humidity while the efficiency of solar cells made with ZnO declined by more than 70 %. Moreover, I showed that a SnO_2 film deposited on top of completed CIGS solar cells significantly increased the device lifetime by forming a barrier against water diffusion. Semicrystalline SnO_2 films deposited at room temperature had nanocrystals embedded in an amorphous matrix, which resulted in films without grain boundaries. These films exhibited better damp-heat stability than ZnO and crystalline SnO_2 films deposited at higher temperature and this difference is attributed to the lack of grain boundary water diffusion.

In addition, I study CBD of $Zn_{1-x}Cd_xS$ from aqueous solutions of thiourea, ethylenediaminetetraacetic acid and zinc and cadmium sulfate. I demonstrate that films with varying composition (x) can be deposited through CBD and study the structure and composition variation along the films' thickness. However, this traditional chemical bath deposition (CBD) approach heats the entire solution and wastes most of the chemicals by homogenous particle formation. To overcome this problem, I design and develop a continuous-flow CBD approach to utilize the chemicals efficiently and to eliminate homogenous particle formation. Only the substrate is heated to the deposition temperature while the CBD solution is rapidly circulated between the bath and a chilled reservoir. We have demonstrated $Zn_{1-x}Cd_xS$ films for a variety of (x) values, with and without varying (x) across film thickness.

Finally, I study on water-dispersed Cu_2ZnSnS_4 nanocrystal inks for the depositions of absorber layers. CZTS thin films from nanocrystal ink has been developed

by several groups, however all these methods produce nanocrystals capped with long alkyl ligands, and thus they are dispersed in organic solvents. Aqueous dispersions of nanocrystals are preferred for environmentally friendly and low cost deposition methods. Thus, I extract CZTS nanocrystals capped with long alkyl chains into polar solvents using K_2S. The nanocrystals are dispersed in water phase, and thin films are deposited from water-based inks by drop casting. Abnormal grain growth (~ 4 μm) is observed when annealed under S and SnS vapor.

TABLE OF CONTENTS

LIST OF TABLES

LIST OF FIGURES

CHAPTER 1

Introduction

United States Energy Information Administration estimated that the global energy consumption will increase by approximately 50 % in the next 30 years.[1] Currently, the majority of the world's energy demand is met by burning fossil fuels, which generates carbon dioxide, a green house gas that contributes to global warming. The light from the sun is a clean, abundant and carbon-free source of energy. Solar cells convert sunlight to electrical energy. Covering only 0.1 % of the earth's surface with 10 % efficient solar cells can supply the entire globe's energy demand. However, in 2010, solar cells provided only 0.005 % of the total energy production in US.[2] The high cost of solar cells is one of the major reasons that limits their wide-spread use.[3] Global photovoltaic production has been doubling in capacity approximately every 2.5 years (Figure 1.1). However, to stay on this aggressive growth trajectory, solar cells must continue to decrease in cost in order to compete with conventional fossil fuel based energy sources.[4-6]

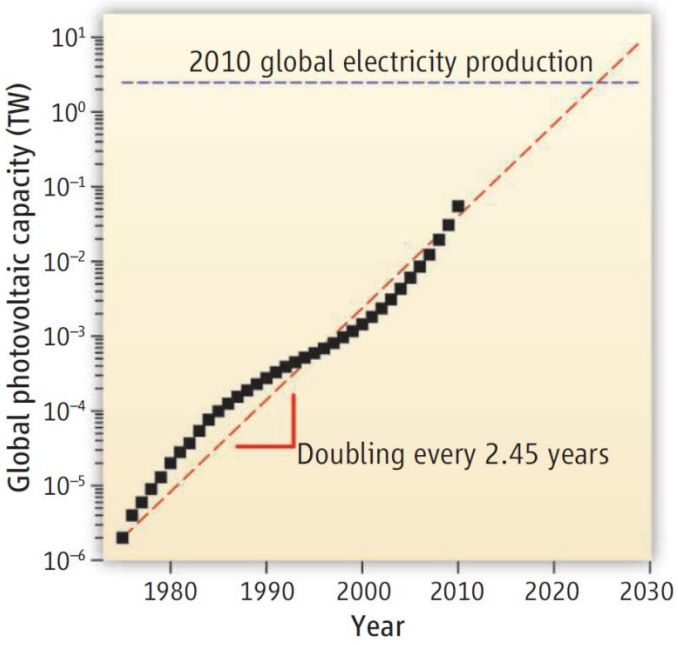

Figure 1.1. Moore's law for solar cells as the accumulated solar cell production since 1975 to 2010.[5] The red dashed line is a linear fit to show the doubling capacity in every 2.5 years, as a comparison with the global electricity production[6] shown in blue dashed line. (Figure reprinted from reference 3)

Currently, the photovoltaic market is dominated by solar cells based on expensive high purity, single-crystal silicon (c-Si) wafers, which are produced using high temperature processing. Solar cells that are based on thin films of semiconductors have the potential to cost less to manufacture than c-Si solar cells partially because their production consumes less energy and less material. For example, a typical absorption coefficient for thin film absorbers is approximately 100 times larger than c-Si and, therefore, 100 times less material (~1 μm) can absorb the same amount of solar energy than ~100 μm c-Si. Moreover, the high purity and high crystallinity requirements in thin film solar cells are less stringent than in c-Si solar cells. It is believed that grain boundaries in thin film solar absorber materials enhance the charge separation and transport because of the electric field at the p-n junction.[7]

1.1. Thin Film Solar Cells

Thin film based solar cells are emerging as an alternative to c-Si solar cells. Among different types of thin film solar cells, those based on copper indium gallium diselenide (CIGS) have the distinction of having the highest overall conversion efficiencies (~20 %), almost as high as c-Si (20-25 %). For this reason, CIGS solar cell market share increased from 0.5 % to 6 % during the last seven years and innovative products are emerging rapidly. For example, in 2010, Dow Solar announced a roof shingle that is also a solar cell made of CIGS (Figure 1.2). Such products are expected to become more widespread in the coming decades.

Figure 1.2. Dow Solar Shingles is a roof material that is reliable under extreme weather conditions while protecting the homes from asphalt shingles.[8] (This figure is reprinted from reference 8).

Thin film CIGS solar cells are built layer by layer on substrates such as soda-lime glass or flexible steel foil through a series of thin-film deposition processes. The scanning electron microscope image, in Figure 1.3, shows the layers that comprise a characteristic CIGS solar cell. In a typical solar cell production, substrates are coated with ~1 μm thick molybdenum layer by DC magnetron sputtering. This is followed by ~2 μm thick light-absorbing CIGS film, most commonly deposited by coevaporation though other methods have also been used.[9,10] Subsequently, a ~70 nm thin cadmium sulfide (CdS) film is deposited, preferably through chemical bath deposition (CBD), to form the p-n junction.

The photo-generated carriers are separated at the CIGS-CdS interface to create electric current. This CdS film is often referred to as the buffer layer. The state-of-art high-efficiency solar cells are obtained only with CBD of CdS. The CBD of CdS is desired for many reasons, one of which is the surface doping of CIGS, which leads to a buried homojunction in the subsurface of the CIGS layer. CBD of CdS also protects the absorber layer against physical damage during the following sputtering steps. The solar cells are completed by RF magnetron sputtering a ~100 nm thin zinc oxide (ZnO) layer, and followed by RF (or DC) magnetron sputtering of a ~200 nm thin conductive transparent tin-doped indium oxide (ITO) film. The ZnO film is also referred to as the window layer. Finally, nickel-aluminum (Ni/Al) grid top contacts are deposited by DC magnetron sputtering or e-beam evaporation techniques.

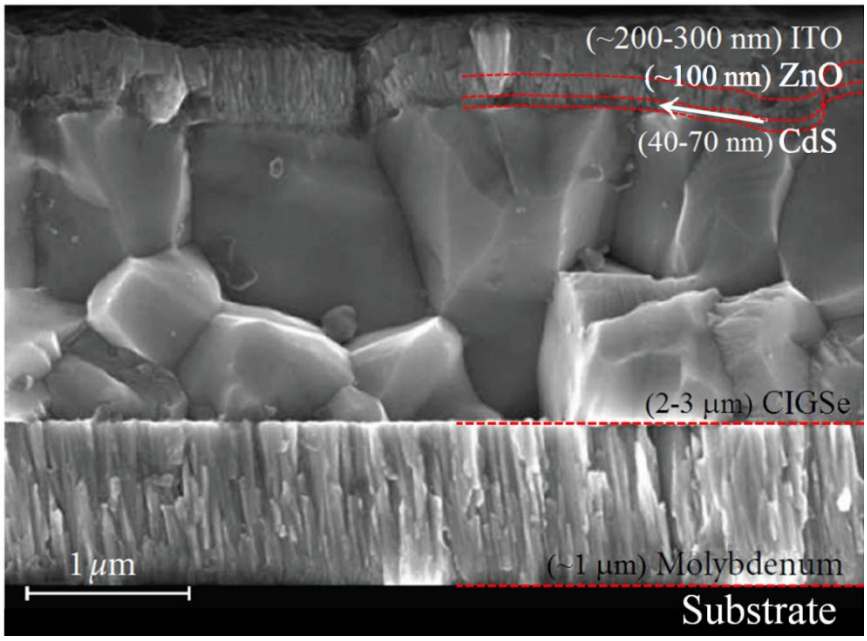

Figure 1.3. Scanning electron microscopy image of a CIGS solar cell. The cross-sectional scanning electron microscopy image shows the stacked layers on a soda-lime glass substrate: From the bottom, ~1 μm thick DC magnetron sputtered Mo back contact, ~2 μm thick co-evaporated CIGS solar absorber, ~50 nm thick chemical bath deposited CdS buffer layer, ~100 nm thick RF-sputtered ZnO window layer, and ~250 nm thick RF sputtered ITO conductive oxide layer. The top Ni/Al grid contacts are not shown in this micrograph.[11] (This figure is reproduced from reference 11).

Although the CIGS solar cells are the highest efficiency thin film solar cells in the market today, their cost per watt ($/W) still needs improvement. One of the major costs is the hermetic sealing between two glass plates, which is crucial to prevent cell degradation due to moisture.[12-16] The solar cell is sealed by sandwiching it between polymer encapsulants such as ethylvinyl acetate (EVA) and two glass layers, one of which is typically the substrate. This increases the weight and the material and labor costs.[17] Another major cost is due to high price of scarce elements that are also in high demand. For instance, indium (In) is used widely in flat panel displays and consequently, its price has risen from 49.90 $/lb in 1995 to 471.74 $/lb in 2005.[18] Replacing In with more abundant elements, such as zinc (Zn) and tin (Sn), is expected to change cost per watt. The cost per watt value for thin film solar cells can be decreased also by increasing the conversion efficiencies. This can be done in two ways. First, replacing the CdS buffer layer with wide band gap $Zn_xCd_{1-x}S$ buffer layers increases the quantum efficiency of the devices. Second, multi-junction photovoltaic device architectures can be used to exceed the Schottky-Queisser limit (33.7 %) for single junction solar cells.

1.2. New Materials for Chalcogenide Based Thin Film Solar Cells

1.2.1. Alternative Window Layers

CIGS solar cells degrade when water diffuses to the CIGS–CdS–ZnO heterojunction. The water diffusion is believed to be through the columnar grain boundaries of ZnO.[12-16] More specifically, this water diffusion results in cracks and reduced n-type carrier concentration in the ZnO layer, and thus the conductivity decreases. As water reaches the CIGS absorber layer, it also reduces the p-type carrier concentration in this layer. The drop in n-type carriers in ZnO window layer and p-type absorber layers reduce the open circuit voltage (V_{OC}) of the device. Moreover, the accumulation of the water in the grain boundaries of CIGS decreases the shunt resistance (R_{Sh}).[15,16,19] Finally, the corrosion of Mo back contact is also observed.[15,16,19]

Thin film amorphous metal-oxides may be used as a glass overlayer for covering the entire device and protecting it against water permeation.[20-22] Such a metal-oxide semiconductor may also be a candidate for replacing the columnar structured wide band gap zinc oxide window layer to stop water diffusion through this layer and improve the long-term device reliability. The film properties required by these two applications are different. Amorphous films have superior water permeation resistance while polycrystalline films generally have better charge carrier transport properties. Thus, it is important to understand how to tune the structure of metal-oxide films between amorphous and polycrystalline. This is one of topics that will be addressed in this thesis.

1.2.2. Alternative Buffer Layers

Even though CBD of CdS provides the highest efficiencies in the laboratory scale CIGS-based solar cells, there has always been an interest to reduce or to eliminate the Cd usage by either alloying or finding alternatives for this buffer layer. The narrow band gap of CdS (E_g ~ 2.41 eV) reduces the quantum efficiency of solar cell devices by blocking the high-energy photon transmission to underneath absorber layer. Zinc sulfide (ZnS) buffer layers can reduce this photon energy loss in the blue region because its band gap (E_g ~ 3.7 eV) is wider than that of CdS. However, using ZnS buffer layers in CIGS-based solar cells resulted in lower efficiencies, which have been attributed to the band misalignment. Hence, tailoring the band gap and its variation across the buffer layer thickness by growing $Zn_xCd_{1-x}S$ though CBD has attracted interest.[23-37]

There is also a problem with the current approach to CBD. In the traditional CBD approach, the entire solution is heated. The reaction results in CdS thin films on the substrate surface, however most of the reactants are consumed by homogenous particle formation. Thus, in the traditional CBD approach, most of the reaction product is toxic waste. In addition, uniform film deposition on larger area substrates is necessary for module manufacturing, but it is challenging with the traditional CBD approach.[38,39] Thus, a new CBD approach to utilize the chemicals efficiently for large-scale uniform film

deposition is necessary. These two approaches, traditional CBD and continuous-flow CBD, are another topic that this thesis will focus on.

1.2.3. Alternative Absorber Layers

One well-known earth abundant alternative for CIGS is copper zinc tin sulfide (Cu_2ZnSnS_4 or CZTS).[40,41] CZTS has a direct band gap of ~ 1.5 eV with high absorption coefficient ($>10^4$ cm^{-1}) and solar cells based on this material can convert solar energy into electricity with only a few micron thick CZTS film.[42] Moreover, the raw material cost for the manufacturing of the CZTS (0.0049 cents/W) is much less than CIGS (0.023 cents/W).[43]

The CZTS films can be deposited by various methods such as coevaporation[44] and *ex-situ* sulfidation[45] of a stack of thin metal films. Alternatively, thin films can be deposited via casting from colloidal CZTS nanocrystal inks at relatively low cost.[46] Although, these nanocrystal inks have been used for high-throughput roll-to-roll processes; the manufacturing cost can be reduced even more by reducing the high usage of organic solvents.[47,48] The replacement of organic solvents with polar solvents, especially with water will be the final discussion in the thesis.

1.3. Thesis Organization

Decreasing the cost per watt of the thin film Chalcogenide-based solar cells can be achieved in many ways. One approach is to use alternative materials that improve the efficiency, long-term reliability or materials cost. Another approach is to improve chemical utilization and reduce hazardous waste created during processing. This thesis addresses a number of approaches all aim towards this end. In chapters 2-4, we present studies on an alternative window material tin dioxide (SnO_2). In chapters 5-7, we describe our studies on zinc-cadmium sulfide ($Zn_xCd_{1-x}S$) for buffer layer through traditional CBD, and through continuous-flow CBD, an alternative approach for improved chemical utilization and large-scale uniform film deposition. In chapters 8 and

9, we present our studies on water-dispersed copper zinc tin sulfide (Cu_2ZnSnS_4, or CZTS) inks for absorber materials.

Chapter two describes deposition of semicrystalline SnO_2 films. We have studied the structure and electrical properties of tin dioxide films deposited by magnetron sputtering as a function of deposition temperature, sputtering power, feed gas composition and film thickness.[20] This study has been published as B. Selin Tosun, Rebekah K. Feist, Aloysius Gunawan, K. Andre Mkhoyan, Stephen A. Campbell, and Eray S. Aydil, "Sputter deposition of semicrystalline tin dioxide films", *Thin Solid Films* **520**, 2554-2561 (2012).

Chapter three describes that SnO_2 layers deposited on top of completed CIGS solar cells can significantly increase the device life time by forming a barrier against water diffusion. Specifically, in accelerated damp-heat tests, our best results showed that the initial peak efficiencies did not decay even after 240 h at 85 °C and 85 % relative humidity.[21] This study has been published as B. Selin Tosun, Rebekah K. Feist, Aloysius Gunawan, K. Andre Mkhoyan, Stephen A. Campbell, and Eray S. Aydil, "Improving the damp-heat stability of copper indium gallium diselenide solar cells with semicrystalline tin dioxide overlayer", *Sol. Energy Mater. Sol. Cells* **101**, 270-276 (2012).

Chapter four describes the results from solar cell architectures by replacing the polycrystalline zinc oxide window layer with semicrystalline tin dioxide. Solar cells made with SnO_2 window layer exhibit the same overall power conversion efficiencies as those made with ZnO and significantly better damp heat stability when compared with same cells completed with ZnO window layers.[22] This study has been published as B. Selin Tosun, Rebekah K. Feist, Stephen A. Campbell, and Eray S. Aydil, "Tin dioxide as an alternative window layer for improving the damp-heat stability of copper indium gallium diselenide solar cells", *J. Vac. Sci. Technol. A* **30(4)**, 04D101 (2012).

Chapter five focuses on the alternative buffer layers $Zn_xCd_{1-x}S$ via classical chemical bath deposition (CBD). We investigate the fundamental factors that govern the evolution of the composition as a function of depth in the film. By changing the initial

concentrations of Zn and Cd salts in the bath, the entire range of overall compositions ranging from primarily cubic ZnS to primarily hexagonal CdS could be deposited.[37] This study is published as B. Selin Tosun, Chelsea Pettit, Stephen A. Campbell, and Eray S. Aydil, "Structure and Composition of $Zn_xCd_{1-x}S$ Films Synthesized through Chemical Bath Deposition", *ACS Appl. Mater. Interfaces* **4**, 3676-3684 (2012).

Chapter six describes the design of the continuous-flow chemical bath deposition (CF-CBD) reactor for efficient utilization of chemicals during CdS film deposition. By chilling the deposition solution, CF-CBD system can highly eliminate the homogenous nucleation that wastes a significant fraction of the reactants.[38] This study is accepted for publication as B. Selin Tosun, Joel T. Abrahamson, Christopher Cheng, Stephen A. Campbell, and Eray S. Aydil, "Efficient Continuous-Flow Chemical Bath Deposition of CdS Films as Buffer Layers for Chalcogenide-Based Solar Cells", *39th Photovoltaic Specialist's Conference Proceedings* (June 17th-21th, 2013).

Chapter seven expounds on the continuous-flow chemical bath deposition reactor and extends it to $Zn_xCd_{1-x}S$ deposition.[39] This study has been submitted as B. Selin Tosun, Joel T. Abrahamson, Christopher Cheng, Stephen A. Campbell, and Eray S. Aydil, "Characteristics of $Zn_xCd_{1-x}S$ Films Deposited with Continuous-Flow Chemical Bath Deposition and a Comparison with Classical Chemical Bath Deposition", for publication.

Chapter eight concentrates on the extraction of oleic acid capped CZTS nanoparticles into polar solvents, specifically into water. Cu_2ZnSnS_4 (CZTS) nanocrystals sterically stabilized with oleic acid and oleylamine ligands and dispersed in nonpolar organic liquids have been extracted into, and electrostatically stabilized in, polar liquids by covering their surfaces with S^{2-}.[47] This study has been published as B. Selin Tosun, Boris D. Chernomordik, Aloysius A. Gunawan, Bryce Williams, K. Andre Mkhoyan, Lorraine F. Francis, and Eray S. Aydil, "Cu_2ZnSnS_4 Nanocrystal Dispersions in Polar Liquids", *Chem. Comm.* **49**, 3549 (2013).

Chapter nine discusses the annealing of CZTS coatings cast from colloidal dispersions in water. Specifically, this chapter focuses on the effects of tin sulfide (P_{SnS}) and sulfur (P_S) vapor pressures on the microstructure evolution during annealing.[48] This study has been prepared for submission as B. Selin Tosun, Boris D. Chernomordik, and Eray S. Aydil, "Effect of SnS Vapor Pressure on Cu_2ZnSnS_4 Thin Film Microstructure from Water-Based Nanocrystal Inks".

CHAPTER 2

Sputter Deposition of Semicrystalline Tin Dioxide Films

In this chapter, we studied the structural and electrical properties of RF magnetron sputtered tin dioxide (SnO_2) films. The effects of deposition conditions, such as substrate temperature, RF plasma power, the feed gas composition and the film thickness, on film properties are investigated. Films deposited at room temperature are semicrystalline with nanometer size crystals embedded in an amorphous matrix. Film crystallinity increases with deposition temperature. When the films are crystalline, the X-ray diffraction intensity pattern is different than that of the powder diffraction pattern indicating that the films are textured with (101) and (211) directions oriented parallel to the surface normal. This texturing is observed on a variety of substrates including soda–lime glass (SLG), Mo-coated soda–lime glass and (100) silicon. Addition of oxygen to the sputtering gas, argon, increases the crystallinity and changes the orientation of the tin dioxide grains: (110) XRD intensity increases relative to the (101) and (211) diffraction peaks and this effect is observed both on Mo-coated SLG and (100) silicon wafers. Films with resistivities ranging between 8 mΩ cm and 800 mΩ cm could be deposited. The films are

n-type with carrier concentrations in the 3×10^{18} cm^{-3} to 3×10^{20} cm^{-3} range. Carrier concentration decreases when the oxygen concentration in the feed gas is above 5%. Electron mobilities range from 1 to 7 cm^2/V s and increase with increasing film thickness, oxygen addition to the feed gas and film crystallinity. Electron mobilities in the 1–3 cm^2/V s range can be obtained even in semicrystalline films. Initial deposition rates range from 4 nm/min at low sputtering power to 11 nm/min at higher powers. However, deposition rate decreases with deposition time by as much as 30%

2.1. Introduction

Thin tin dioxide (SnO_2) films find applications in a wide variety of devices such as sensors and solar cell.[49-52] SnO_2 is a wide band gap (3.8 eV) semiconductor that crystallizes in tetragonal Cassiterrite crystal structure with lattice parameters a=b=4.737 Å and c=3.185 Å. Although, SnO_2 thin films have been used in gas sensors and as transparent conducting electrodes, its high chemical stability also makes it an attractive replacement for wide band gap semiconductor oxides such as ZnO. Tin dioxide has been deposited on various substrates including Si,[49,53] glass slides,[50,53-57] quartz,[58] InSb,[51] and InP[52]. Many techniques such as sol–gel deposition,[59] chemical bath deposition from $SnCl_4$,[60] chemical vapor deposition,[61] spray pyrolysis,[62] electron beam evaporation,[57,63] thermal evaporation,[64] and sputtering[49-56,58,65-67] have been used to deposit SnO_2 films. In most studies where intrinsic SnO_2 was studied, the films have been deposited by reactive sputtering of metallic tin (Sn) target under O_2/Ar atmosphere.[49,51–52] Films deposited at low O_2 concentration in the feed gas show metallic characteristics.[49] In high power DC sputtering, the films consist mostly of the monoxide phase[49,54,56]. Most of the research on sputtered SnO_2 films focused on depositing n-type films with high conductivity by doping with Sb.[54–56,58,66,67] SnO_2:Sb has been studied both with reactive sputtering of Sn:Sb (95.5% weight purity) metallic targets using Ar/O_2 gas[54,56] and with RF sputtering of SnO_2 ceramic targets with Ar gas.[55,58,66,67] Increase in deposition rates, grain sizes, carrier concentration and carrier mobility have been observed with increasing sputtering power and decreasing working pressure.[55] The lowest resistivity achieved with SnO_2:Sb

films in these studies was 2 mΩ cm. SnO_2 has also been deposited in nitrogen ambient to form p-type SnO_2:N.[65]

In some applications, it is desirable to use SnO_2 instead of crystalline ZnO. While sputtered ZnO films are almost always crystalline with (0002) axis of the grains oriented normal to the substrate, sputtered SnO_2 films can be crystalline or amorphous with comparable charge densities and mobilities to sputtered ZnO. Since ZnO and SnO_2 also have similar band gaps, amorphous SnO_2 may be a potential replacement for ZnO in copper indium gallium diselenide (CIGS) solar cells. Amorphous SnO_2 may be preferred in applications where water penetration into the layers under the oxide layer reduces the long term reliability of the devices as is the case in CIGS thin film solar cells. Polycrystalline ZnO is susceptible to water penetration through grain boundary diffusion of water whereas amorphous SnO_2 can act as a barrier. Mixture of amorphous and nanocrystalline SnO_2 where nanocrystals are embedded in amorphous matrix without forming grain boundaries may even achieve better charge transport properties without sacrificing the barrier properties. Thus, it is important to be able to control the structure of SnO_2 films between amorphous and polycrystalline.

In this chapter, we explain the deposition of SnO_2 films using radio frequency (RF) magnetron sputtering and the effects of RF power, substrate temperature, film thickness and oxygen concentration in the feed gas on the electrical and structural properties of the deposited films. The films' crystal structure was studied by X-ray diffraction (XRD) and transmission electron microscopy (TEM) while electrical properties were determined using a combination of room temperature Hall effect and four-point probe measurements. This study was conducted to find the sputtering conditions that yield semi-crystalline films where nanocrystals of SnO_2 are prevalent but do not about against each other to form grain boundaries.

2.2. Experimental details

Tin dioxide films were sputtered from a 3" diameter wide and 0.25" thick SnO_2 (99.99% purity) ceramic target in a AJA-ATC-2000 sputtering system. The substrates were either polycrystalline Mo (250 nm) coated 1 mm thick glass (Mo-SLG) substrates or bare 1 mm thick soda–lime glass (SLG) slides. In some experiments (100) Si wafers were also used. All substrates were cleaned ultrasonically in a deionized water, acetone and isopropanol mixture (1:1:1 ratio by volume) and dried by blowing compressed air across the substrate. The target surface was cleaned for 3 min by pre-sputtering prior to all depositions while a shutter that protects the substrate was closed. The base pressure in the sputtering chamber was around 2.7×10^{-4} Pa and sputtering was started only after reaching this pressure or lower for each experiment. The sputtering pressure was kept constant at 0.67 Pa, which was maintained by flowing 20 sccm of sputtering gasses (Ar or Ar/O_2) into the chamber. The sputtering guns are aligned at an angle of 23.58° with respect to the vertical axis which is normal to the substrate surface. Target to substrate distance was 19.5 cm. The substrate platen was rotated at 20 rpm throughout the deposition and heated using tungsten–halogen infrared lamps beneath the platen.

The RF power and the O_2 concentration in the feed gas were varied for sputtering between 100Wand 250W from 0% to 15%, respectively. Films were deposited for different time periods to yield different thicknesses: specifically, we deposited and studied films that were 200±20 nm, 300±20 nm and 500±20 nm thick. In the experiments where O_2 is used, the total flow rate of Ar and O_2 was kept constant at 20 sccm. In the experiments where the substrates were heated to 150 °C, the substrates were kept at 150 °C for 10 min prior to starting the plasma and the deposition.

Film thicknesses were measured using a surface profilometer by scanning through a step between the film and the substrate. This step was created by partially covering the substrate prior to the deposition. Cu-Kα radiation (λ=0.154056 nm) was used to record XRD from the films and to study the structural properties. A Bruker–AXS microdiffractometer equipped with a 2.2 kW sealed Cu source and a two dimensional Hi-

Star detector was used. The 2D detector improves the signal to noise ratio via the collection of both specular and non-specular diffracted X-rays. The X-ray beam spot size was 800 μm. The sheet resistance of the films was determined by both a linear four-point probe system and Hall-effect measurements using the Van-der-Pauw configuration at room temperature. The electrical measurements were done on films deposited on SLG substrates. Transmission electron microscopy (TEM) analysis was conducted using an FEI Tecnai F-30 microscope with a Schottky field-emission electron gun operated at 300 keV.[68]

2.3. Results and Discussion

2.3.1. Effect of RF power on the films' electrical and structural properties

As expected, the film deposition rate increases with increasing RF power. Figure 2.1 shows the average deposition rates determined by dividing the film thickness by the deposition time. This increase with increasing RF power is due to increasing argon ion (Ar^+) density and the ensuing increase in the sputtering rate. However, the deposition rate decreases with elapsed deposition time. For example, Figure 2.1 shows that the average deposition rate is lower when depositing a 500 nm thick film than when depositing a 200 nm thick film. Figure 2.1 also shows that the deposition rate is insensitive to the substrate temperature. This rules out heating of the substrates as the cause for the deposition time dependence of the deposition rate. There could be numerous reasons for sputtering time dependence including heating of the target or changes in the structure and surface of the film, which may affect the sticking properties but this is not a focus of this study.

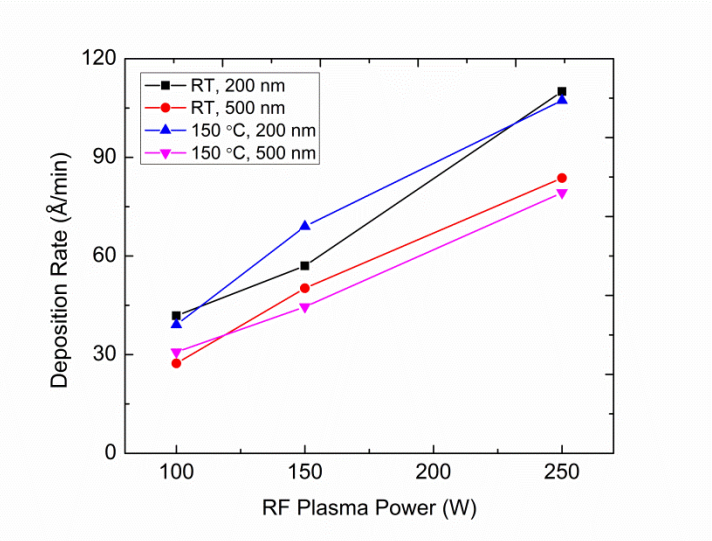

Figure 2.1. Time-averaged SnO_2 film deposition rate as a function of RF sputtering

Figure 2.2 shows the XRD from films deposited under a variety of conditions on Mo-coated soda–lime glass. XRD from (110), (101) and (211) Cassiterrite planes are clearly detectable superimposed on broader peaks in some films but are completely absent in others indicating that the crystallinity of the film depends on sputtering conditions and film thickness. First obvious trend is that thicker films tend to appear more crystalline than the thinner films regardless of the deposition temperature. The 200 nm thick films, Figure 2.2(a) and (b), show amorphous diffraction pattern with very weak (101) and (211) peaks, while the 500 nm films show distinct (101) and (211) peaks, Figure 2.2(c) and (d). Second, increasing the substrate temperature from room temperature to 150 °C also increases crystallinity. In Figure 2.2(d), which shows the XRD from a 500 nm thick film deposited at 150 °C, the (110), (101) and (210) peak intensities are all much more intense than those in Figure 2.2(c), the XRD for a 500 nm thick film deposited at room temperature. Third, increasing the RF plasma power also appears to increase the crystallinity, though this effect is much less obvious than the changes due to film thickness and substrate temperature.

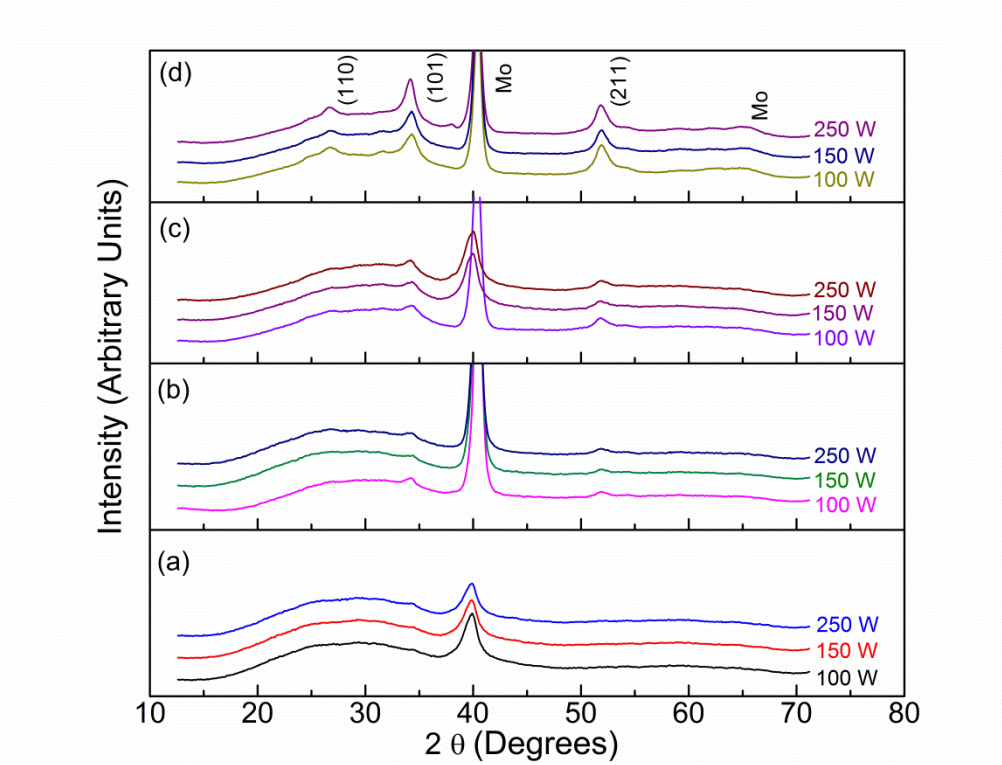

Figure 2.2. X-ray diffraction pattern from SnO_2 films deposited using different RF sputtering powers. XRD from 200 nm thick SnO_2 films deposited (a) at room temperature and (b) at 150 °C. XRD from 500 nm thick SnO_2 films deposited (c) at room temperature and (d) at 150 °C. The SnO_2 diffractions are labeled with Miller indices whereas the Mo (110) peak at 40.5° is labeled as Mo.

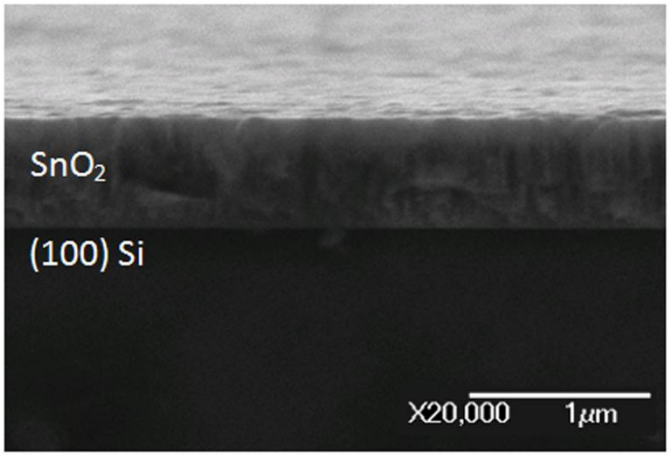

Figure 2.3. Scanning electron micrograph of SnO_2 films deposited on Si (100) substrates at 250 W RF power and at 150 °C.

Figure 2.3 shows the scanning electron micrograph (SEM) of the 500 nm thick SnO_2 film deposited using 250W RF power at 150 °C. The film was grown on (100) Si substrates. The columnar grains of the film are aligned along the (101) plane normal to the (100) Si surface. As it is clear from the SEM micrograph, the deposited film is smooth and continuous over the substrate. Other films also showed similar characteristics.

The broad diffraction spanning the range 20° to 37° is present on films deposited on all the substrates (SLG, Mo-SLG and (100) Si) and increases with increasing SnO_2 thickness suggesting that it is due to SnO_2. Such broad diffraction can originate from amorphous glasses. We attribute absence of sharper diffractions but presence of this broad peak to the presence of amorphous SnO_2 in the film. Thus, we conclude that thin (200 nm or less) films deposited at low

RF powers and low temperatures tend to contain amorphous SnO_2 but the film crystallinity increases with increasing film thickness, substrate temperature and RF power. Whether crystalline regions exist in films deposited at room temperature and in 200 nm thin films cannot be concluded from XRD alone. The diffraction peak from the nanocrystals overlaps with the broad amorphous feature. To address this issue we examined the films using cross sectional TEM. We found that the 200 nm thick films deposited at room temperature consisted of 5–10 nm SnO_2 nanocrystals embedded in an amorphous SnO_2 matrix. The nanocrystals are surrounded by amorphous SnO_2 and do not abut against each other. Thus, despite its nanocrystalline structure the films do not contain any grain boundaries. Figure 2.4(a) and (b) shows high-resolution TEM images of the SnO_2 films grown using 250W RF at room temperature and 250WRF at 150 °C. These films were deposited on native oxide covered Si substrates to facilitate TEM while approximating deposition on glass substrates. The selected area electron diffraction (SAED) patterns obtained from the films confirm the presence of both amorphous and crystalline components in both films. The film grown using 250WRF at 150 °C exhibits more intense polycrystalline-like diffraction ring indicative of higher crystalline content than that of 250W RF at room temperature.

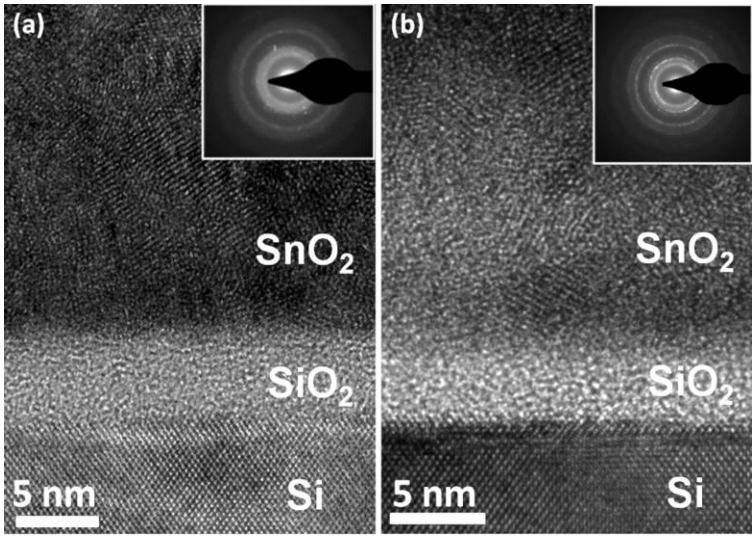

Figure 2.4. High Resolution TEM image of SnO_2 films deposited in Si/SiO_2 substrate using 250 W RF power at room temperature **(a)** and at 150 °C **(b)**. The insets show the SAED patterns obtained from approximately 4 x 10^{-3} μm^3 volume of films.

The grain sizes, determined from the full width at half maximum of the XRD peaks using Scherer analysis are shown in Figure 2.5 as a function of RF power for different substrate temperatures and film thicknesses. These grain sizes are consistent with the range of grain sizes observed using TEM. The grain size is a strong function of the SnO_2 film thickness suggesting that SnO_2 crystals nucleate and grow during deposition. It seems that the films start out amorphous and SnO_2 crystallites nucleate and grow as the deposition proceeds. Grains are also larger at 150 °C substrate temperature than at room temperature.

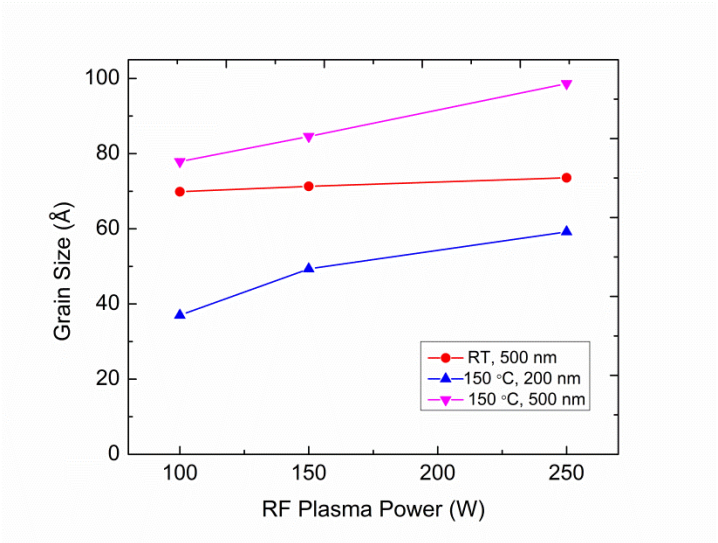

Figure 2.5. Grain size in SnO_2 films deposited on Mo-coated SLG substrates estimated from Scherer analysis.

Table 2.1 lists the electrical resistivity, the carrier mobility and the carrier density of the SnO_2 films deposited on glass substrate. The resistivity of the films decreases with increasing RF power. This decrease is partially due to an increase in the carrier concentration and partially due to an increase in the mobility. The general trend in increasing mobility may be explained by better film crystallinity at higher RF powers. While it is possible that this increase may be brought about by unintentional heating of the substrate at higher sputtering powers, the platen temperature did not rise during sputtering. Increasing carrier concentration with RF power indicates an increase in the concentration of defects that dope SnO_2 n-type. These are thought to be O-vacancies.[56] Temperature is the other deposition parameter that affects the resistivity. Increasing the temperature can affect the film resistivity in two ways. First, increasing the temperature can increase the crystallinity and improve mobility, which would decrease the resistivity. On the other hand, increasing the temperature can anneal oxygen vacancies and defects, which are thought to dope the film.[56] This, in contrast, would increase the resistivity. For example, the carrier concentration decreases from $5.7\times10^{19}cm^{-3}$ to $3.2\times10^{19}cm^{-3}$ when the deposition temperature is increased from room temperature to 150 °C for the 500 nm thick film deposited using 150W RF power. These effects compete to determine the film

resistivity and which trend dominates depend on other deposition parameters. Indeed, depending on the RF power we observe both trends in resistivity. Focusing on 500 nm thick films deposited at 100 W, we observe that the film resistivity increases (from 0.25 Ω cm to 0.77 Ω cm) as the temperature is increased from room temperature to 150 °C. In contrast, the resistivity of the films deposited at higher RF powers decrease with increasing deposition temperature. In general, mobilities increase with increasing deposition temperature. The lower mobility for the highest conductivity film deposited at 250W and 150 °C may be due to scattering from the high concentration of defects that dope the films. Indeed, the carrier concentration of this film is very high.

Table 2.1. Electrical resistivity, carrier concentration and hall mobility of SnO_2 films sputtered under different RF powers and with different thicknesses.

RF Power	Thickness	Temp.	ρ (Ω cm)	n (x 10^{19} cm^{-3})	μ (cm^2/V s)
100 W	200 nm	Room temp.	N/A	N/A	N/A
150 W	200 nm	Room temp.	0.70	N/A	N/A
250 W	200 nm	Room temp.	0.16	3.6	1.1
100 W	500 nm	Room temp.	0.25	N/A	N/A
150 W	500 nm	Room temp.	0.20	5.7	0.5
250 W	500 nm	Room temp.	0.009	16.3	4.5
100 W	200 nm	150 °C	0.35	N/A	N/A
150 W	200 nm	150 °C	0.17	4.2	0.9
250 W	200 nm	150 °C	0.011	8.9	6.5
100 W	500 nm	150 °C	0.77	1.8	0.4
150 W	500 nm	150 °C	0.05	3.2	3.9
250 W	500 nm	150 °C	0.008	35.9	2.1

2.3.2. Effect of the film thickness on electrical and structural properties

Figure 2.6 shows the effect of film thickness on the XRD patterns from SnO_2 films deposited at room temperature, Figure 2.6(a), and at 150 °C, Figure 2.6(b). This figure clearly shows the effect of the deposition time on the films' crystallinity. The 200 nm thick films deposited at room temperature exhibit mostly an amorphous diffraction pattern whereas thicker films begin to show larger XRD peaks from (101) planes. The XRD peaks are larger partly because there is more material in thicker films. Indeed, TEM shows that even the 200 nm thick films contain nanocrystals embedded in amorphous SnO_2. However, the intensity of the diffraction from the (101) planes relative to the broad

diffraction from amorphous tin dioxide also increases with film thickness indicating that the film structure becomes more crystalline. The effect of film thickness on the film structure is most obvious for films deposited at 150 °C as the intensity of the (101) XRD peak increases steadily as the film thickness increases from 200 nm to 500 nm. Also, Figure 2.5 shows that the crystal sizes in thicker films are substantially larger.

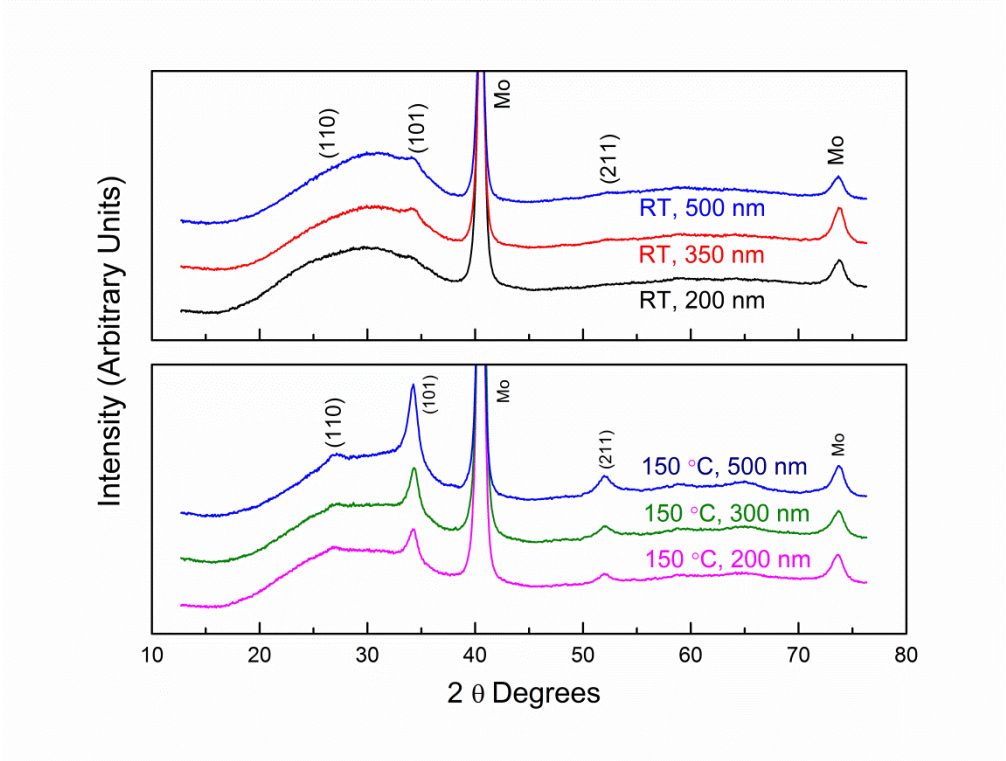

Figure 2.6. X-ray diffraction from different thickness SnO_2 films deposited on Mo-coated SLG substrates **(a)** at room temperature, **(b)** at 150 °C using 250 W RF sputtering power.

Figure 2.7(a) and (b) shows the resistivity, the mobility and the carrier density in SnO_2 films as a function of thickness at room temperature and at 150 °C, respectively. As the films get thicker, the film resistivity decreases but reaches a constant value. At room temperature, this decrease is due to an increase in higher carrier concentration because mobility remains approximately constant at 1–2 cm^2/V s. At 150 °C, the decrease in resistivity is mainly due to an increase in mobility while the carrier concentration remains constant with film thickness. The mobility in the film deposited at 150 °C is higher as

expected. These trends are consisted with the XRD data shown in Figure 2.6: thinner films consist of nanocrystals embedded in amorphous SnO_2 and mobility is approximately at 1–2 cm^2/V s. In contrast at 150 °C, the mobility increases due to higher film crystallinity.

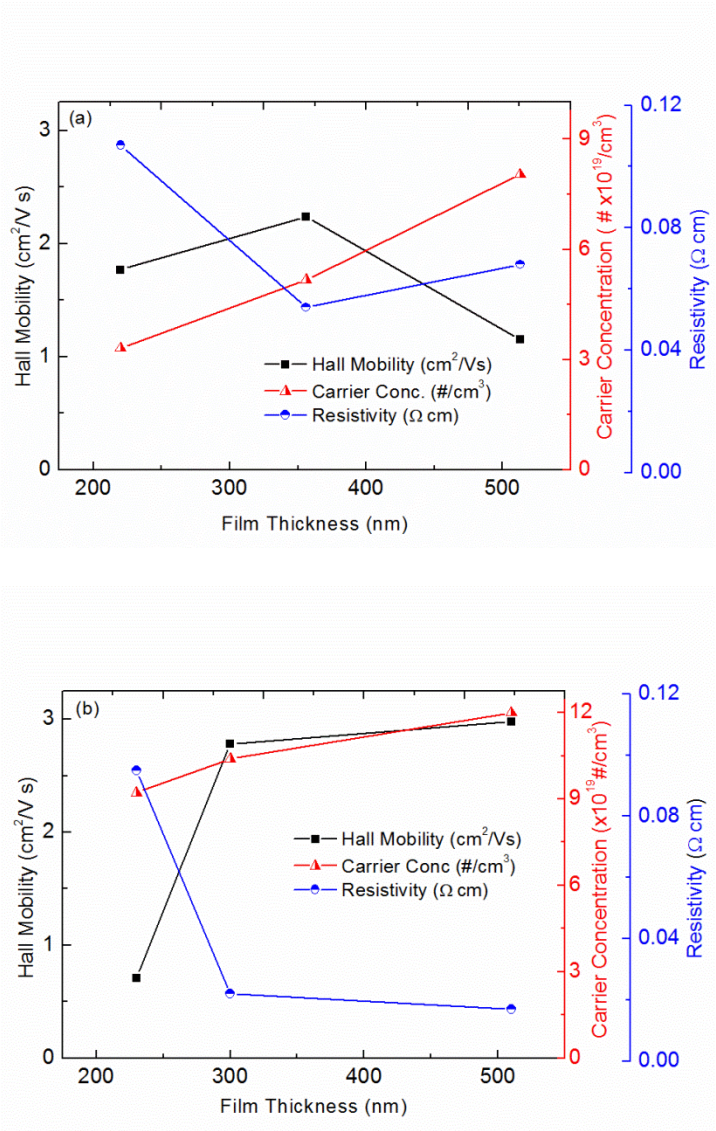

Figure 2.7. Electrical resistivity, carrier concentration and Hall mobility of SnO_2 films on SLG substrates as a function of film thickness. Films were deposited **(a)** at room temperature and **(b)** at 150 °C using 250 W RF sputtering power.

2.3.3. Effect of O_2 concentration in the feed gas on electrical and structural properties

Figure 2.8 shows the effect of O_2 concentration in the feed gas on the SnO_2 deposition rate. During the experiments, the RF power was kept constant at 250 W. These films were approximately 350 nm thick. The O_2 concentration in the feed gas was varied between 0% and 15%. Only a slight decrease in deposition rate is observed when O_2 concentration is increased beyond 10% but the deposition rate remains approximately constant up to 10% O_2 addition.

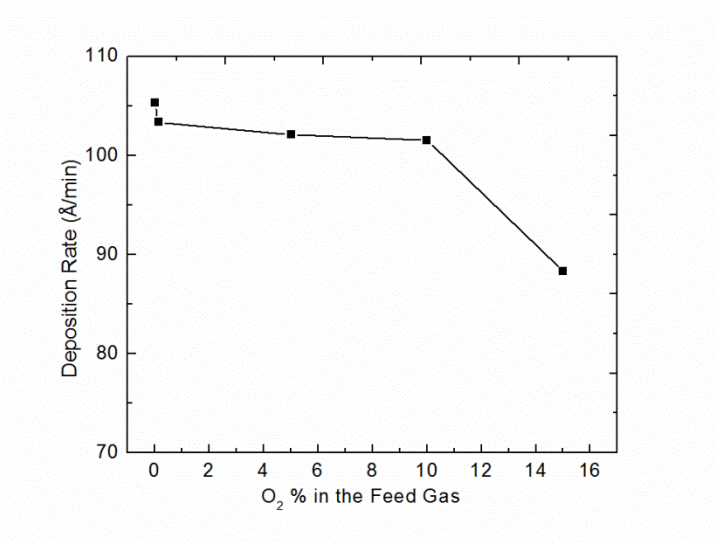

Figure 2.8. Average deposition rates of SnO_2 films as a function of O_2 % in the feed gas. Films were 350 nm thick and were deposited using 250 W RF sputtering power.

Figure 2.9(a) and (b) shows the effect of O_2 concentration in the feed gas on the crystallinity of the films deposited on Mo-coated SLG and (100) Si wafers, respectively. The films were deposited at room temperature using 250W RF power. As the O_2 concentration in the feed gas increases, the intensity of the (110), (101) and (211) XRD peaks increase indicating that the films become more crystalline. Films deposited at low O_2 concentrations show that XRD from (101) planes is dominant despite the fact that (110) diffractions should be the largest for a powder diffraction pattern. The films deposited at low O_2 mole fractions show that films are textured with (101) planes

oriented normal to the substrate surface but the intensity of the (110) peak grows steadily with increasing O_2 concentration. When the O_2 concentration in the chamber reaches 10%, the film structure changes from a textured film where the [101] axis of the grains are oriented normal to the surface to more randomly oriented grain structure. A continuous increase in the (211) peak intensity with increasing O_2% in the feed gas is also observed. In contrast, at high O_2 concentrations in the feed gas, the deposited film XRD shows an intensity distribution closer to the powder diffraction pattern.

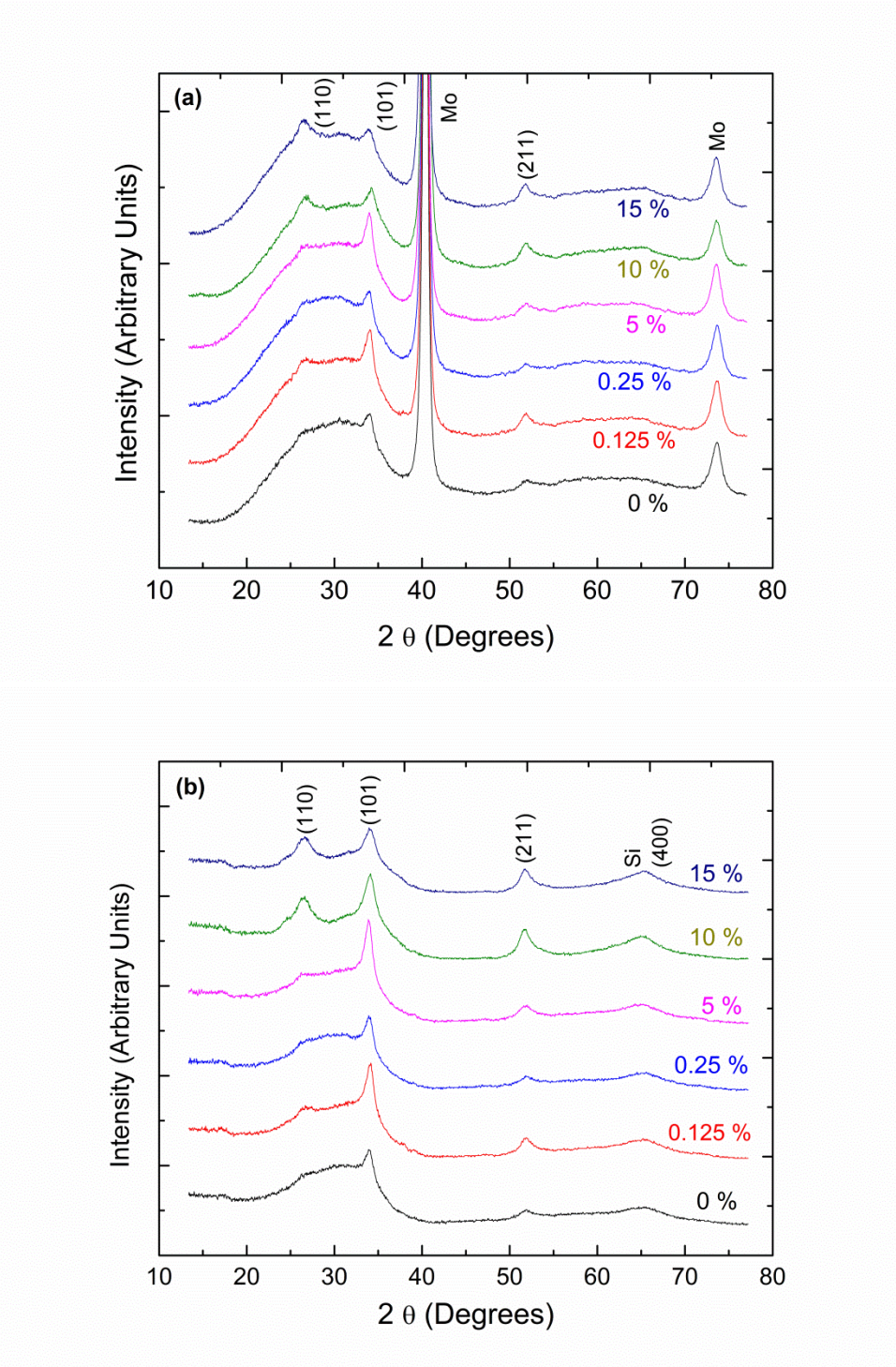

Figure 2.9. X-ray diffraction from the SnO_2 films deposited using different O_2 % in the feed gas **(a)** on Mo-coated SLG and **(b)** on (100) Si substrates.

Clearly, the mobility is determined by the microstructure and orientation of the grains. Figure 2.10 shows the resistivity, the mobility and the carrier concentration in SnO_2 films deposited at room temperature using 250W RF power. The resistivity increases as O_2 concentration in the feed gas increases. This is partially due to decreasing mobility and partially due to decreasing carrier concentration. The decrease in carrier concentration is attributed to the reduction in O vacancies with increasing O_2 in the feed gas. With small addition of O_2, the film crystallinity improves as revealed by the increasing XRD peak along the (101) direction. Thereafter the carrier mobility decreases with O_2 concentration because the films become less textured: the (110) XRD peak grows in as the (101) XRD peak decreases. The film's XRD pattern becomes more like that of a powder diffraction pattern. As the O_2 concentration in the feed gas is increased above 10%, the preferred orientation of the film changes from (101) to (110) and the mobility begins to increase again as the film become textured again, albeit in another direction (110).

2.3.4. Optical properties

Figures 2.11 and 2.12 show the optical transmission and Tauc plots for SnO_2 films, respectively. The films were transparent in the visible region of the optical spectrum but begin to absorb below ~400 nm. The extrapolation of Tauc plots yielded band gaps ranging from 3.4 eV to 3.65 eV. While there is a systematic increase in the band gap with decreasing sputtering power, the Tauc extrapolation method is sensitive to the details of the extrapolation and accurate to about 0.1 eV. The small differences (~0.05 eV) between 200 nm and 500 nm thick films are within the accuracy of the Tauc method: the band gap should not be a function of the film thickness. Band gap of SnO_2 has been suggested to shift to lower values than 3.6 eV with increasing oxygen vacancies.[69] This hypothesis is consistent both with our optical and electrical characterization data. Increasing the sputtering power decreases the band gap and carrier concentration and both of these effects have been hypothesized to be due to increasing oxygen vacancies in the film.[56,69] The index of refraction extracted from the visible (500–700 nm)

transmission using methods described in reference 22 ranged between 1.8 and 1.9. This is slightly lower than the index of refraction of bulk SnO_2[70] and we attribute this lower value to internal voids, which were also observed in low-resolution TEM images.

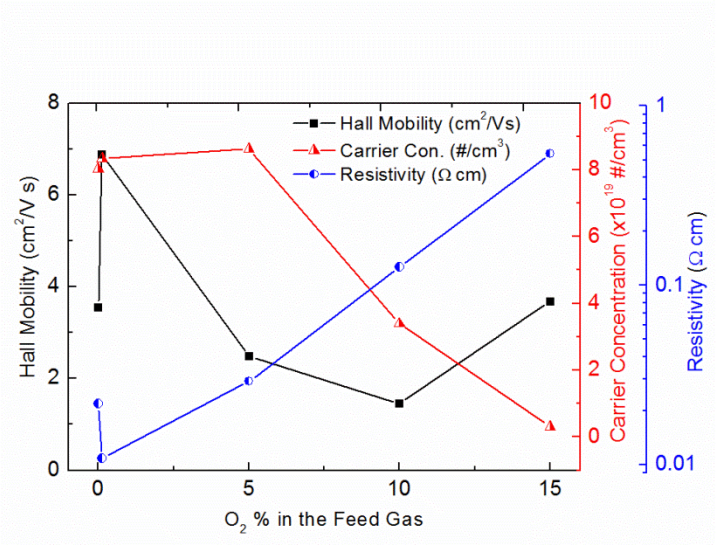

Figure 2.10. The resistivity, the carrier concentration and the Hall mobility of SnO_2 films on SLG substrates as a function of O_2 % in the feed gas.

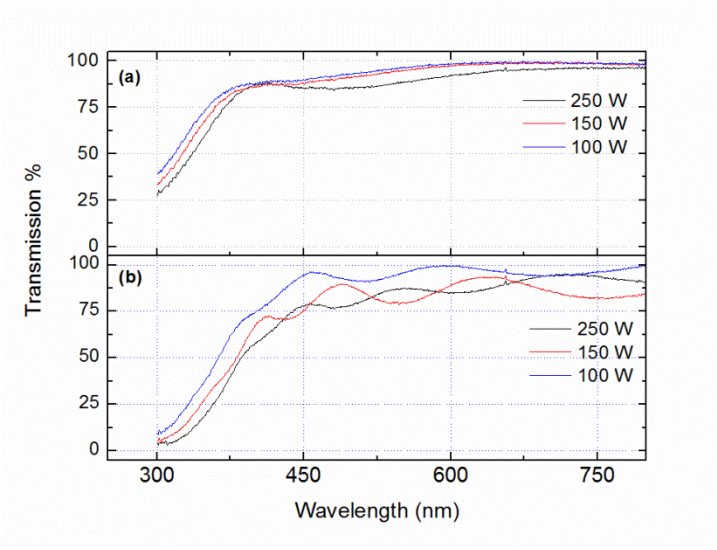

Figure 2.11. Optical transmission of nominally **(a)** 200 nm and **(b)** 500 nm thick SnO_2 films sputtered at various RF powers at room temperature.

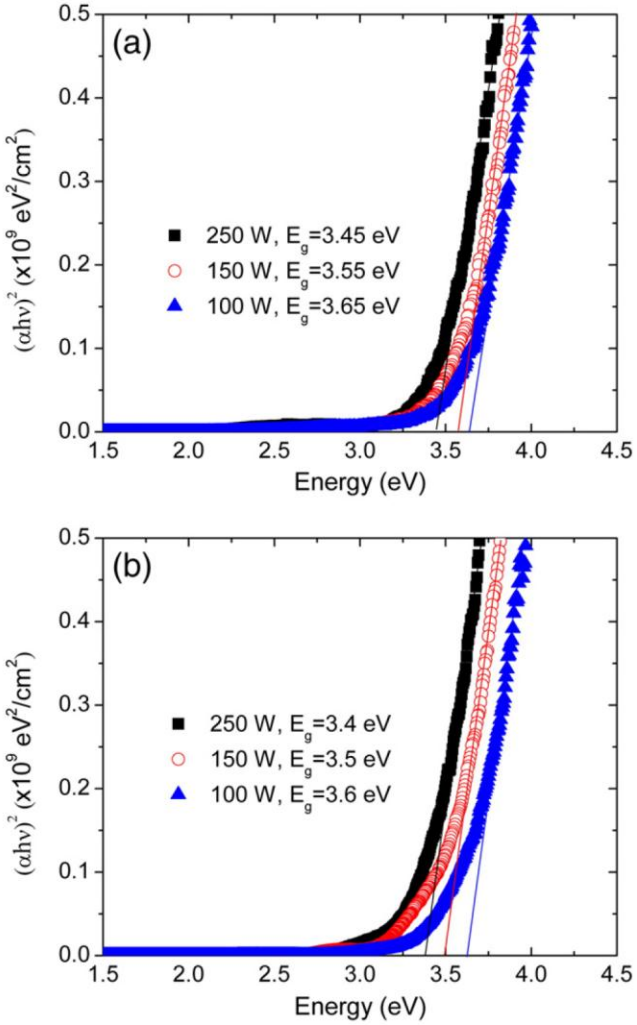

Figure 2.12. Tauc Plots for **(a)** 200 nm and **(b)** 500 nm thick SnO_2 films sputtered at various RF powers at room temperature. Extrapolated values of the band gap are in the legend.

2.4. Conclusions

Sputtered SnO_2 films become more crystalline with increasing RF power, film thickness and substrate temperature. A small amount of O_2 (0.125%) in the feed gas also increases the crystallinity of the films. The SnO_2 film electrical resistivity decreases with increasing RF power, film thickness and substrate temperature. The lowest resistivity, 8 mΩ cm, is achieved at 150 °C and using 250W RF power in a 500 nm thick film. The highest carrier concentration, 3.6×1020 cm^{-3}, is achieved with 250W RF power and 150

°C substrate temperature in 500 nm thick SnO_2 films. A decrease in carrier concentration from 1020 cm^{-3} to 1018 cm^{-3} is observed when O_2 is added into the feed gas. The carrier mobility of the films increases with increasing RF power, film thickness and substrate temperature. Semicrystalline SnO_2 thin films can have mobilities of the order of 1–3 cm^2/Vs. This is only slightly lower than the mobilities achieved in polycrystalline SnO_2 and ZnO films (5–35 cm^2/Vs)[71-75] and our highest crystallinity films deposited by sputtering (6.8 cm^2/Vs). We recently showed that the semicrystalline films have superior water barrier properties as compared to polycrystalline SnO_2 and ZnO films. We were also able to assemble CIGS solar cells with semicrystaline SnO_2 films with no sacrifice in the solar cell efficiency as compared to films made with polycrystalline ZnO: these results will be reported elsewhere. Thus, while there is some sacrifice in the carrier mobility of the semicrystalline SnO_2 films in comparison to polycrystalline SnO_2 and ZnO, it is not significant to cause degradation of device characteristics. However, their barrier penetration properties are significantly improved. At the 150 °C substrate temperature, 250W RF power and 500 nm thick films, the carrier mobility is achieved lower than what is expected. This is attributed to increasing defect scattering with increasing carrier density. The highest carrier mobility is achieved as 6.8 cm^2/V s with 250W RF power and 350 nm thick films with 0.125% of O_2 in the feed gas. While the trends discussed above are reproducible, the absolute values are sensitive to chamber base pressure, sputtering target and sputtering target age. For example, the films in Table 2.1 and Figure 2.7 were deposited using different targets.

CHAPTER 3

Improving the Damp-Heat Stability of Copper Indium Gallium Diselenide Solar Cells with a Semicrystalline Tin Dioxide Overlayer

While copper indium gallium diselenide (CIGS) thin film solar cells with laboratory efficiencies exceeding 20% have been reported, these high efficiencies may degrade with time as the devices are exposed to humid environments. The degradation is known to be due to the water penetration through the CIGS-CdS-ZnO layers. This water penetration must be reduced or stopped to increase the solar cell lifetime. In this chapter, we demonstrate significantly improved lifetime by using diffusion barrier. Under accelerated damp-heat test condition, which is 85 ºC and 85 % relative humidity, the solar cells without the tin dioxide layer lost nearly 80 % of the initial efficiency, within 24 h after commencing the test. On the other hand, solar cells that are coated with semi-amorphous SnO_2 films deposited at room temperature sustained their initial efficiency for 240 hours under identical conditions. The semicrystalline films exhibited better damp-heat stability than crystalline films deposited at higher temperature. We infer from the slow open circuit voltage decay that water permeation to the p–n junction is reduced

when semicrystalline SnO_2 over layers are used to protect the solar cell. We attribute this difference in damp heat stability to the lack of grain boundary water diffusion in semicrystalline SnO_2 films.

3.1. Introduction

Laboratory scale power conversion efficiency of copper indium gallium diselenide (CIGS) thin film solar cells is 20%[44], but the long-term stability still needs improvement. Typically, the long-term stability of solar cells is studied in accelerated damp-heat (DH) tests at 85 °C and 85% relative humidity (RH). It is now well established that the water penetration into the solar cell is the culprit because the dry heat tests do not cause any major changes in the cell performance while damp-heat tests degrade the solar cell dramatically.[14,15] Under damp-heat conditions, unprotected CIGS solar cell efficiencies degrade very rapidly to less than 50 % of the initial efficiency.[14,16–18] This degradation is due to several factors including changes in the window and absorber layers as well as the corrosion of the metals.[17-19] The changes in window and absorber layers decrease both the open circuit voltage (Voc) and the fill factor (FF), but do not affect the short circuit current density (Jsc) significantly.[17–19] The fill factor is thought to decrease because the resistance of the ZnO and/or the transparent conducting oxide layers (e.g.,Al doped ZnO or Sn doped In_2O_3) increases.[14,17,18,76-82] The open circuit voltage is thought to decrease because the Fermi level in the CIGS near the CdS–CIGS interface increases.[14,17,18,76-78,82]

The lifetimes of CIGS solar cell are increased by covering and encapsulating them in glass adding both weight and cost. Block copolymers such as ethylvinyl acetate (EVA) may also be used but it is difficult to make organic encapsulants with comparable performance to inorganic glasses. Organic encapsulants may be more effective if changes in the solar cell can be made that decrease the burden on the encapsulant. Herein, we show that a thin tin dioxide (SnO_2) coating on the CIGS solar cell increases the solar cell life time in damp heat tests without an encapsulant layer. We believe that high resistance

of SnO_2 to moisture permeation retards the degradation of the solar cells. We report the evolution of SnO_2 over-coated CIGS solar cell power conversion efficiencies, FF, V_{OC}, and J_{SC} as a function of time in damp humidity tests and compare these results to those for uncoated CIGS solar cells.

3.2. Experimental Details

CIGS solar cells, [Figure 3.1(a)], were fabricated on stainless steel foil by co-evaporation at 550 °C. The CIGS layer was approximately 2 mm thick. Following, 80nm thick CdS was deposited on the CIGS film through chemical bath deposition. A 50nm thick insulating layer of ZnO and a 150 nm thick tin doped indium oxide (ITO), were deposited on CdS by RF magnetron sputtering. Contact to the ITO was made with an evaporated Ni/Ag grid pattern that is connected to a thicker bus bar at the edge of the foil for electrical contact. The back contact was made with sputtered Mo on the stainless steel substrate and beneath the CIGS absorber layer. Transmission electron microscopy (TEM) analysis was conducted using an FEI Tecnai F-30 microscope with a Schottky field-emission electron gun operated at 300 keV.[68]

Tin dioxide thin films with varying thickness were deposited on completed CIGS solar cells using RF magnetron sputtering. The film thickness was changed between 200 nm ± 20 nm and 500 nm ± 20 nm. The films were deposited at the RF power levels, 100 W, 150 W, and 250 W and at two different substrate temperatures, room temperature and 150 °C. For the films deposited at 150 °C, the substrates were kept at 150 °C for 10 minutes before starting the deposition. Prior to all depositions, the target surface was cleaned for 3 minutes by presputtering while a shutter protected the substrate. The base pressure in the sputtering chamber was 2×10^{-6} Torr and deposition sequence was started only after reaching this pressure or lower for each experiment. The sputtering pressure was kept constant at 5 mTorr, which was maintained by flowing 20 sccm of sputtering gas (Ar) into the chamber. The sputtering guns were at a 23.58° with respect to the

substrate normal. The electronic and structural properties of the SnO_2 films as a function of deposition conditions were published in a previous study.[20]

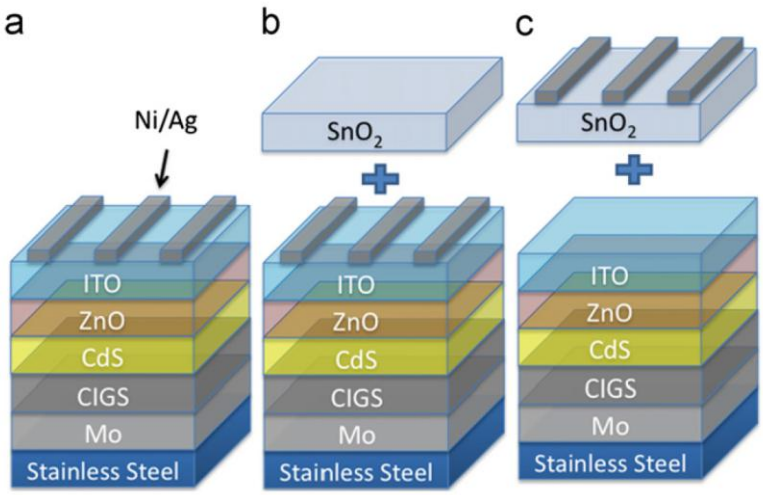

Figure 3.1. (a) Conventional CIGS solar cell configuration. **(b)** CIGS solar cell configuration with SnO_2 coating above the top collection grid. **(c)** CIGS solar cell configuration with SnO_2 coating between the top collection grid and the window layer.

The damp heat tests were conducted in a temperature and humidity controlled chamber at 85 °C and 85 % relative humidity. The solar cells were taken out from the test chamber every 24 hours and their current-voltage characteristics were measured. The control solar cells were tested under damp-heat conditions for 168 hours, while the SnO_2-film-coated cells were tested under identical conditions for 240 hours. The current-voltage characteristics of the solar cells were recorded periodically, under 100 mW/cm^2 (AM 1.5) illumination generated by a solar simulator equipped with a Xe-arc lamp. The solar cell figures of merit, the fill factor (*FF*), the open circuit voltage (V_{oc}), the short circuit current density (J_{sc}), and the cell efficiency ($\eta = FF \times J_{sc} \times V_{oc}$) were measured outside the damp-heat test chamber under ambient conditions (~ 25 °C). The shunt (R_{sh}) and the series (R_{sr}) resistances of the cells were also determined as a function of the damp-heat test exposure time.

Table 3.1. SnO_2 deposition conditions for the second CIGS solar cells set.

Solar Cell Sample Name	SnO_2 Deposition Conditions		
	RF Power	$T_{substate}$ (°C)	Thickness
1	150 W	Room temp.	200 nm
2	150 W	Room temp.	200 nm
3	250 W	Room temp.	500 nm
4	150 W	Room temp.	500 nm
5	100 W	Room temp.	500 nm
6	250 W	150 °C	200 nm

Two types of tests were conducted. In one set of the experiments, SnO_2 films were deposited on complete CIGS solar cells over the metal current collecting grid as shown in Figure 3.1(b). This set of solar cells was used to screen the most suitable SnO_2 sputtering conditions for improving stability. In the second set of experiments, SnO_2 films were deposited on the ITO layer beneath the metal collection electrodes as shown in Figure 3.1(c). The deposition conditions of the SnO_2 thin films for these solar cells are given in Table 3.1. In this second set, the SnO_2 deposition conditions were chosen from those that yielded promising results in the first set of experiments. Unlike in other studies, no encapsulation was used.[18] Identical CIGS solar cells without the SnO_2 layer were used as the control samples and exposed to the same damp-heat testing for comparison. These cells are referred as the control solar cells in this article.

3.3. Results and Discussion

Figure 3.2 shows the results from the first set of experiments where the SnO_2 films were deposited on completed solar cells [Figure 3.1(b)]. The SnO_2 films were deposited under twelve different sputtering conditions. Figure 3.2(a) shows the efficiency of the solar cells, normalized to their initial efficiency, after 144 and 216 hours of damp-heat testing. Figure 3.2(b) shows the absolute values of the efficiencies after 144 and 216 hours in the damp-heat testing chamber. The results are also compared with the unprotected CIGS solar cells, named as “Control” in the Figures 3.2(a) and 3.2(b). To see if there is a trend with respect to the SnO_2 film properties and deposition conditions, we rank ordered the data in Figure 3.2(a) in decreasing performance after 216 hours. First, it

is obvious that SnO_2 films help increase the damp-heat durability of the CIGS solar cells because significant fraction of the SnO_2-coated cells performed better than the control sample after 216 hours in the damp-heat test chamber. Second, the solar cells coated with SnO_2 films sputtered at room temperature show better durability than the solar cells coated with SnO_2 sputtered at 150 °C. For example, the top three films in Figure 3.2(a) are all deposited at room temperature and retain approximately 70 % of their initial efficiency as compared to the control solar cell whose efficiency has decayed to 30 % of the initial value. The solar cell coated with 200 nm thick SnO_2 film deposited using 150 W RF plasma power at room temperature showed the best reliability. The SnO_2 films deposited at room temperature were a mixture of amorphous SnO_2 and nanocrystalline SnO_2 with nanometer size grains embedded in an amorphous matrix (semicrystalline).[20] For example, Figure 3.3 shows low- and high- resolution TEMs of SnO_2 films deposited under the same conditions, at room temperature using sputtering power of 150 W. Here we used a SiO_2-covered Si substrate for deposition of SnO_2. Semicrystalline nature of the SnO_2 film is apparent. The TEM images show nanocrystalline SnO_2 embedded in amorphous SnO_2. In these films there are no grain boundaries to facilitate water diffusion. Based on the sizes of the crystalline grains and the thickness of the electron transparent sample, we estimated that the fraction of the crystalline grains is 25-30% of the total film. In contrast, films deposited at 150 °C tended to be more crystalline with grains abutted against each other.[20] The better protection performance of the semicrystalline films compared to polycrystalline films is attributed to the lack of grains and therefore lack of the grain boundary diffusion of water. The fraction of crystalline grains was calculated by estimating the average grain size and number of grains from TEM images, including one presented in Figure 3.3. From low-loss EELS data the thicknesses of the sample was measured to be ~60 nm.[83,84] The volume fraction of the crystalline grains was then computed to be 25-30 %, which also takes into account that depending on the location of the grain within a specimen some of the grains will not be visible.[85]

Figure 3.4 shows the changes in the power conversion efficiency, fill factor, open circuit voltage, and short circuit current density as well as the changes in the shunt and series resistances as a function of damp-heat testing time for the unprotected control solar cells. Each substrate had eight solar cells. The results in Figure 3.4 are from those cells on each substrate, which showed the best performance under damp heat test conditions. The power conversion efficiencies of the unprotected solar cells decreased rapidly from 8 - 12 % to less than 3 % within 48 hours as a function of damp-heat test time. Similarly, the fill factor for these control cells decreased within 48 hours from ~ 70 % to ~ 25 % [Figure 3.4(b)]. Figure 3.4(c) shows the evolution of the open circuit voltage of these control solar cells as a function of damp-heat test time. The open circuit voltage dropped by approximately 50% from ~ 0.65 V in the first 24 - 48 hours and then decayed more slowly to ~ 0.12 V. Figure 3.4(d) shows that the short circuit current density, J_{sc}, only lost 10 % of its initial value, a noticeable but otherwise insignificant decrease when compared to other solar cell figures of merit. Figures 3.4(e) and 3.4(f) show the evolution of the series and the shunt resistances, respectively, as a function of damp-heat test time. The series resistance increased from ~ 5 Ω to 10 - 30 Ω within the first 48 hours but eventually saturated at approximately 10±2 Ω after 168 hours of DH exposure. More dramatic changes in the shunt resistance were observed. The shunt resistance decreased exponentially with damp-heat testing time by three orders of magnitude during the first 72 hours and saturated after reaching approximately 5 - 20 Ω. Figure 3.5 shows the evolution of the current-voltage (*J-V*) characteristics of a typical control solar cell. The fill factor decreases without a significant drop in the J_{sc} and the *J-V* characteristic degrades by pivoting around (0, J_{sc}) point. This shows that the dramatic drop in the shunt resistance is responsible for the decrease in the fill factor and the effect of the changing series resistance is small in comparison.

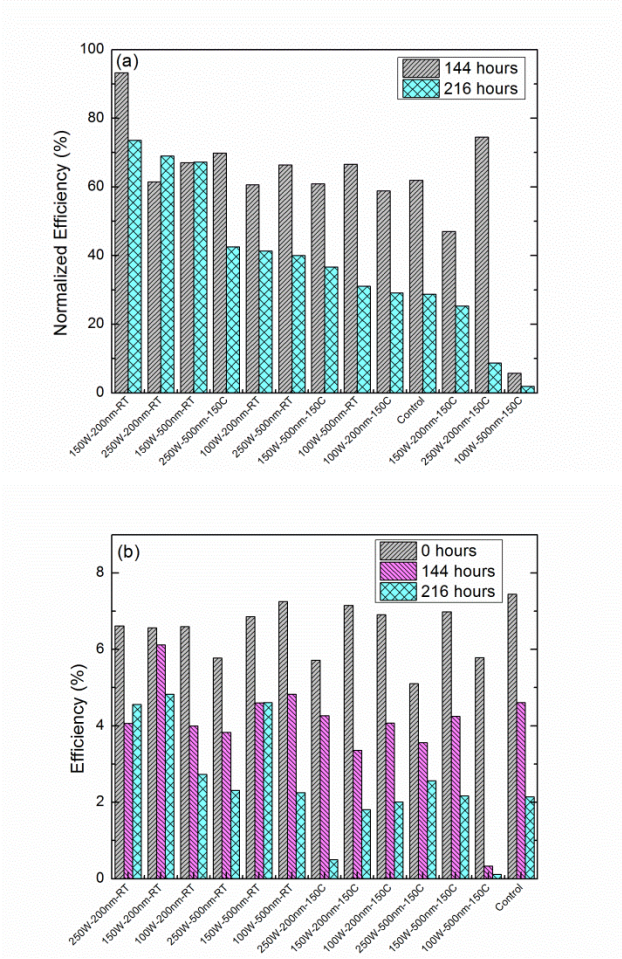

Figure 3.2. (a) Solar cell stability performance for the solar cell configuration shown in Figure 3.1(b). The efficiencies are normalized with respect to the initial solar cell efficiencies and ranked from left to right based on their performance after 216 h in the damp heat test chamber. **(b)** The absolute values of the solar cell efficiencies for the solar cells in (a).

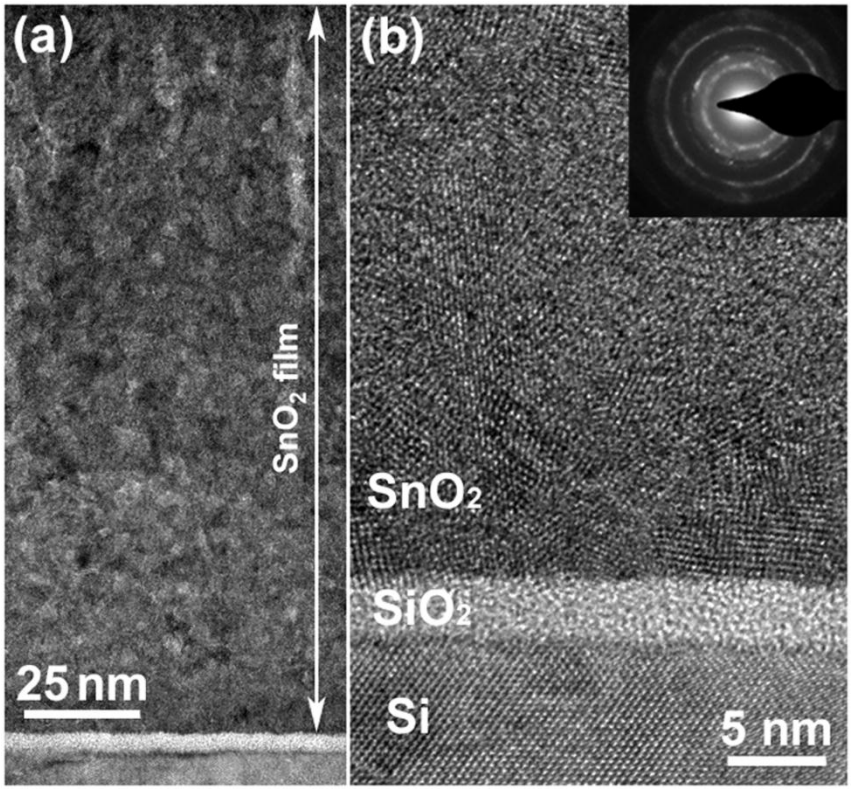

Figure 3.3. (a) Low magnification and **(b)** high magnification TEM images of SnO_2 films deposited in SiO_2-coated Si substrates at room temperature using 150 W RF power. The inset is the diffraction pattern from the SnO_2 film confirming the semicrystalline structure of the film.

The observations in Figure 3.4 on the degradation of control solar cells are consistent with the previously published reports. The increase in series resistance is attributed to the increase in ZnO and ITO resistivity.[14,17,18,76-82] The penetration of water to the CIGS absorber layer is believed to decrease the carrier concentration in the CIGS layer and to increase the Fermi level in the p-type absorber, E_{FP}.[14,17,18,76-78,82] The increase in E_{FP} explains the decrease in open circuit voltage. In addition, the carrier concentration in the ZnO layer may also be decreasing which lowers the Fermi level, E_{FN}, in the n-type ZnO and therefore the open circuit voltage.[17,79,80] Decrease in carrier concentration and carrier mobility has been observed in ITO films.[81] Lower carrier concentration in CIGS can also increase series resistance of the solar cell and contribute to the decrease in the fill factor.[14,17,18,76-78,82] Shunt resistance decrease with damp heat exposure has been observed previously[17,77] though there are only a few reports and the reasons are not well

understood. Igalson et al.[17] attributed the shunt resistance decrease to changes in the grain boundaries forming high conductance pathways remains unclear. A second possibility is the damp heat treatment increases the leakage across the ZnO-CdS-CIGS interface through the emergence of trap-assisted tunneling as a current leakage mechanism after damp heat treatment.[17]

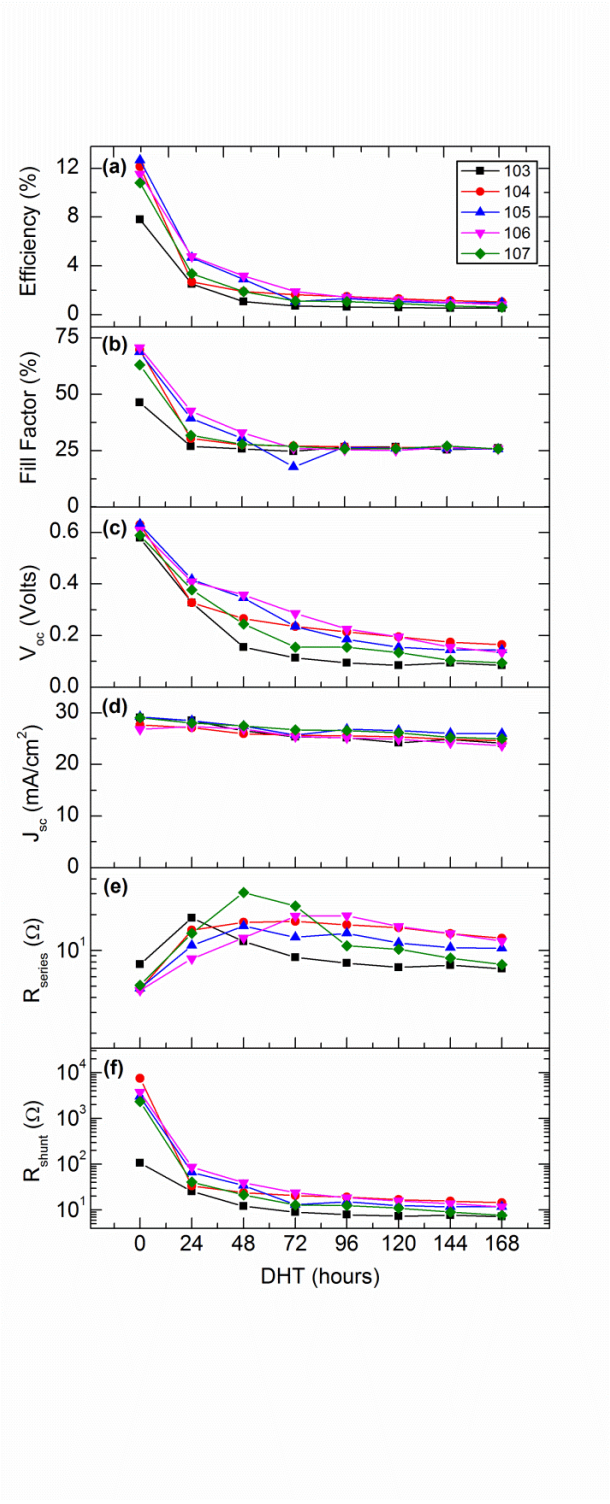

Figure 3.4. (a) Efficiency (η), **(b)** fill factor (FF), **(c)** open circuit voltage (V_{OC}), **(d)** short circuit current density (J_{SC}), **(e)** series resistance (R_{SR}), and **(f)** shunt resistance (R_{SH}) of the control solar cells as a function of damp-heat exposure time (DHT).

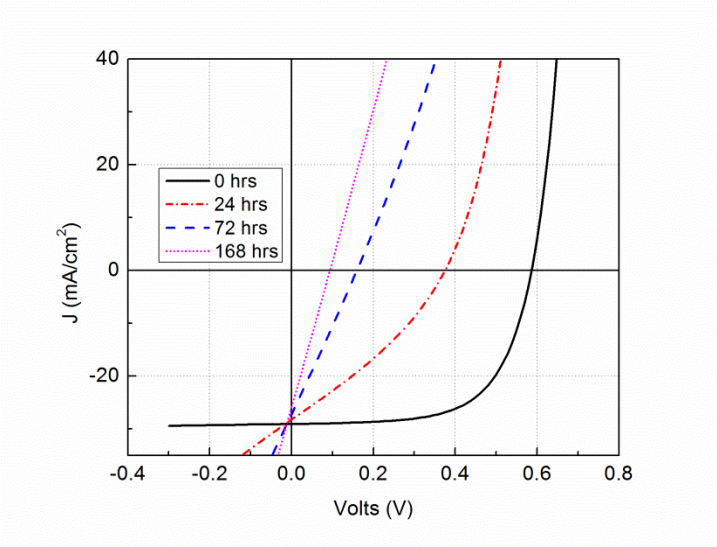

Figure 3.5. Temporal evolution of the current-voltage characteristics of an uncoated control CIGS solar cell as a function of damp heat exposure time.

Figure 3.6 shows the evolution of η, FF, V_{oc}, J_{sc}, R_{sh}, and R_{sr} as a function of damp-heat test time for SnO_2-coated solar cells [Figure 3.1(c)]. The deposition conditions for the SnO_2 film used for each solar cell are listed in Table 3.1. Each substrate had eight solar cells. The results in Figure 3.5 are from those cells, which showed the best performance under damp heat test conditions. Compared to Figure 3.4(a), the power conversion efficiencies of the SnO_2-coated solar cells do not drop rapidly and there is significant improvement in their damp-heat stability [Figure 3.6(a)]. Some solar cells (e.g., 1, 2, and 4) maintain their initial power conversion efficiency even after 240 hours under damp-heat conditions while other cells (e.g., 3, 5, and 6), though still better than the control solar cells, show 15 – 50 % drop from their initial efficiencies. Among the solar cells that show 15 - 50 % drop, the degradation rate is not uniform in time. For example, in some solar cells (e.g., 6) the initial power conversion efficiency was maintained for the first four days but degradation accelerated thereafter. Figure 3.6(c) shows the evolution of the open circuit voltage as a function of damp-heat test time. The open circuit voltages off all cells decreased less than 8 % from their initial values even after 240 hours in the damp-heat test chamber. Since the open circuit voltage decay is typically attributed to change in the Fermi levels E_{FN} and E_{FP} in ZnO and CIGS,

respectively,[14,17,18,76-82] we conclude that these levels and therefore the carrier concentrations in the ZnO and CIGS layers are not affected significantly by the damp-heat test conditions when the cells are coated with a thin layer of semicrystalline SnO_2. The insignificant change in the open circuit voltage suggests that the semicrystalline SnO_2 inhibits water penetration through the ZnO layer to the CdS and CIGS layers. The short circuit current density, shown in Figure 3.6(d), also does not show any change even after 240 hours of damp-heat testing. In solar cells where some degradation is observed (e.g., 3, 5, and 6), the decrease in the efficiency can be attributed almost solely to the decreasing shunt resistance which in turn decrease the fill factor [Figure 3.6(b)]. For example in solar cell 5 the efficiency, FF, R_{sr}, and R_{sh} remain constant for the first four days of the damp-heat test but after day four, the shunt resistance decreases by two orders of magnitude coinciding with the drop in the FF and the efficiency. In contrast, the stable solar cells 1, 2, and 4 maintain their initial shunt and series resistances value for the entire duration (240 hours) of the damp-heat stability test.

Figure 3.7 shows the evolution of representative *J-V* characteristics from SnO_2-coated solar cells as a function of DH exposure time. Figure 3.7(a) is the *J-V* characteristic of a solar cell coated with semicrystalline SnO_2 film deposited at room temperature (Cell 2 in Table 3.1 with corresponding TEMs shown in Figure 3.3). After 240 hours, except for a small decrease in V_{oc}, the *J-V* characteristic has not changed significantly compared to the *J-V* characteristic recorded prior to the damp heat test. In fact, the shunt resistance has improved. Figure 3.7(b) shows the *J-V* characteristics for solar cell 5; this cell did not show degradation for approximately 5 days under DH conditions but degraded rapidly after day 5. Figure 3.7(b) shows that, except for a slight increase in the series resistance, the *J-V* characteristic of this solar cell was unchanged after 120 hours. However, after 240 hours in DH conditions the series resistance had increased by a factor of four from ~5 Ω to over 20 Ω, while the shunt resistance had decreased by nearly two orders of magnitude from ~6×10^3 Ω to less than ~200 Ω. Nearly all of this degradation occurred after 120 hours which is responsible for the decrease in the FF and the overall efficiency. The delayed decrease in the shunt resistance in the case

of solar cell 5 can be an indicator of the delayed water penetration through the SnO_2 layer to the layers below. Finally, Figure 3.7(c) shows the *J-V* characteristic of solar cell 6. The SnO_2 coating on this cell is fundamentally different in structure that the others because it is deposited while maintaining the substrate at 150 °C. The films deposited at this temperature have much higher crystallinity and resemble polycrystalline films with grain boundaries rather that the semicrystalline structure in Figure 3.3.[20] As a consequence the films deposited at 150 °C are more prone to grain boundary water diffusion. Indeed, solar cell 6 is the worst performer of all cells. While slower, its *J-V* characteristic evolves in the same way the unprotected solar cells evolve (e.g., Figure 3.5) as a function of damp heat exposure time.

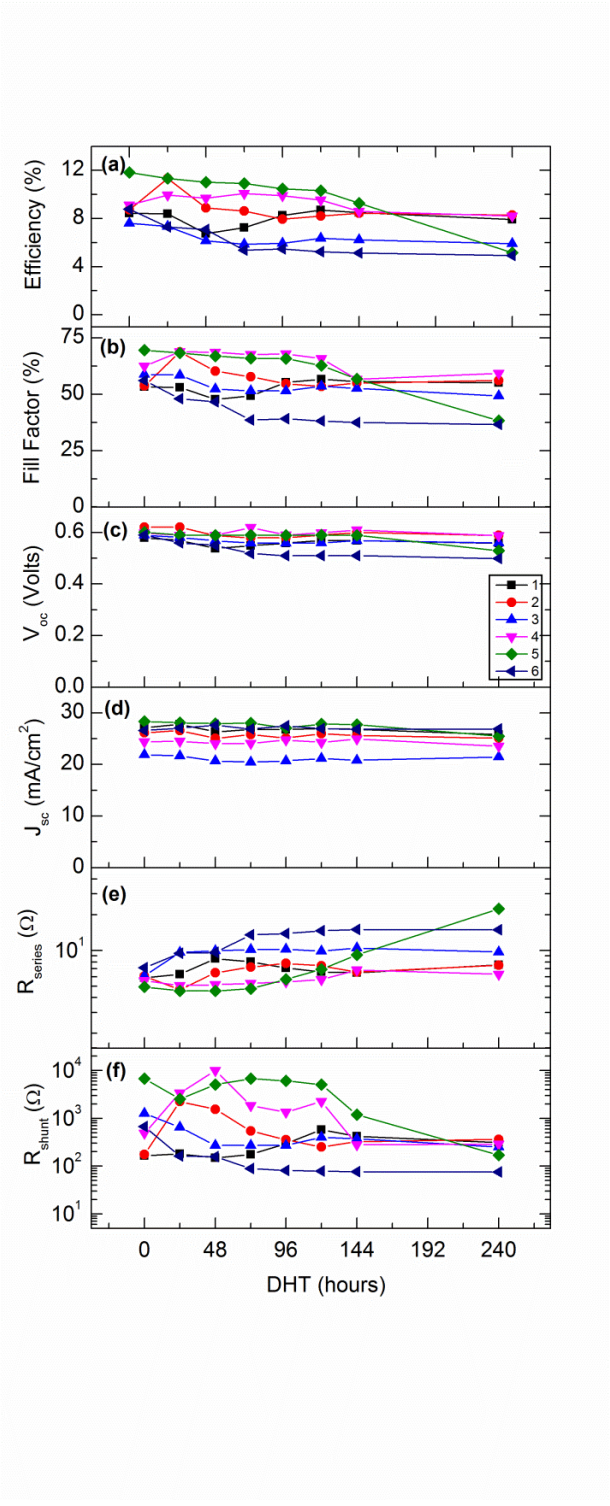

Figure 3.6. **(a)** Efficiency (η), **(b)** fill factor (FF), **(c)** open circuit voltage (V_{OC}), **(d)** short circuit current density (J_{SC}), **(e)** series resistance (R_{SR}), and **(f)** shunt resistance (R_{SH}) of the SnO_2-coated solar cells as a function of damp-heat exposure time (DHT).

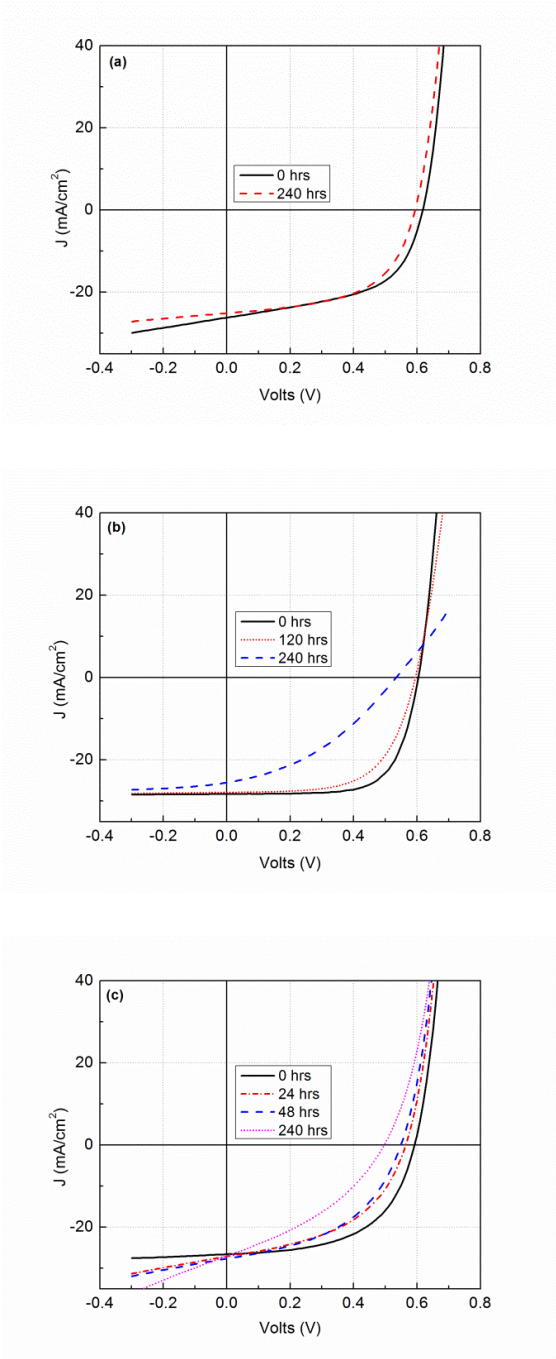

Figure 3.7. Temporal evolution of the current-voltage characteristics of three representative SnO_2-coated [Figure 3.1(c)] CIGS solar cells as a function of the damp heat exposure time: **(a)** solar cells 2, **(b)** solar cell 5, and **(c)** solar cell 6. See Table 3.1 for SnO_2 deposition conditions and Figure 3.6 for the temporal evolution of the solar cell figures of merit.

3.4. Conclusions

We studied the ability of the RF magnetron sputtered SnO_2 films deposited on CIGS solar cells to protect the solar cells from humidity. Compared to uncoated control solar cells, the damp-heat durability of SnO_2-coated CIGS solar cells increased significantly. Specifically, the power conversion efficiency, the fill factor, and the open circuit voltage of the uncoated control solar cells decreased dramatically during damp-heat tests while their power conversion efficiencies dropped from ~ 12 % to ~ 0.8 % in 168 hours. Consistent with previous reports, the decrease in the efficiency was caused by decreasing fill factor and open circuit voltage. The short circuit current density did not change significantly. In contrast, the solar cells protected with a SnO_2 over-layer deposited at room temperature maintained their initial power conversion efficiencies even after 240 hours in the damp-heat test chamber at 85 °C and 85 % relative humidity. In all SnO_2-coated solar cells, the short circuit current density and the open circuit voltage decreased less than 8 % even after 240 hours of damp-heat testing. Any observed decline in the power conversion efficiency is attributed mostly to decreasing fill factor. The best damp-heat test protection was achieved with SnO_2 films sputtered at room temperature using 150 W RF power. Even a SnO_2 film as thin as 200 nm thick is adequate to improve the damp heat stability of CIGS solar cells. The semicrystalline structure of this SnO_2 layer, sans grain boundaries, is believed to inhibit the moisture penetration. This structure eliminates diffusion of water molecules along the grain boundaries and provides a better protection from damp-heat conditions than polycrystalline films.

The tin dioxide layer is not an encapsulation. The tin dioxide layer is meant to decrease the water permeation requirements on thinner, flexible encapsulates by making the solar cell architecture more robust with respect to water permeation. That we do not observe degradation for 240 h under 85 °C and 85 % RH even without an encapsulant is promising. Moreover, tin dioxide is a wide band gap material with high visible transmission[8] and high thermal and UV stability. Use of the tin dioxide layer in conjunction with flexible encapsulants is expected to help these encapsulants in

exceeding module qualification according to IEC 61646 where the solar cells are expected to be stable for 1000 h under 85 °C and 85 % relative humidity.

CHAPTER 4

Tin Dioxide as an Alternative Window Layer for Improving the Damp-Heat Stability of Copper Indium Gallium Diselenide Solar Cells

In the previous chapter, we talked about the degradation of CIGS based solar cells with time when they are exposed to humid environments, which was attributed to the grain boundary diffusion of water through unstable ZnO window layer. In this chapter, we showed that CIGS-based solar cells using semi-crystalline SnO_2 performed the same overall power conversion efficiencies as those made with polycrystalline ZnO (~8%). The open circuit voltages of the solar cells made with ZnO and SnO_2 were the same indicating that the band alignment with tin dioxide is suitable for CIGS solar cells. More importantly, the efficiency of solar cells made with SnO_2 decreased less than 5% after 120 hours at 85 ^{o}C and 85% relative humidity while the efficiency of the solar cells made with ZnO declined by more than 70%.

4.1. Introduction

Even though copper indium gallium diselenide (CIGS) solar cell power conversion efficiencies reached over 20 % in the laboratory,[86,87] the lifetimes of these

solar cells remain short without the hermetic encapsulation. As discussed in the previous chapter, the lifetime degradation of CIGS solar cells with humidity exposure places stringent requirements on encapsulation of the finished solar cells, which can increase cost and constrain devices to be encapsulated and sealed within glass. The international Electrotechnical Commission (IEC) standard accelerated damp-heat tests conducted at 85 °C and 85 % relative humidity require that encapsulated and sealed devices must last at least 1000 hours to have service lifetimes in excess of 20 years. For CIGS-based devices, the efficiency (η) is proposed to decrease when water reacts within the ZnO transparent conductive film, reducing its carrier concentration and carrier mobility.[14,17,18,76-78] Some studies have also shown that water diffuses through polycrystalline ZnO to the CIGS-CdS junction where it reacts photochemically to reduce the hole concentration in the CIGS layer.[14,17] These reactions reduce both the open circuit voltage (V_{OC}) and the fill factor (FF) of the solar cells while the short circuit current (Jsc) usually remains unaffected.[14,17-19,76-78,82,88] The FF decreases because the resistivity of the ZnO layer and, thus, the overall solar cell series resistance increase.[14,17,18,76-78] The V_{OC} decreases because the changes in the carrier concentrations raise and lower the Fermi levels in the CIGS and ZnO, respectively.[14,17,18,76-78]

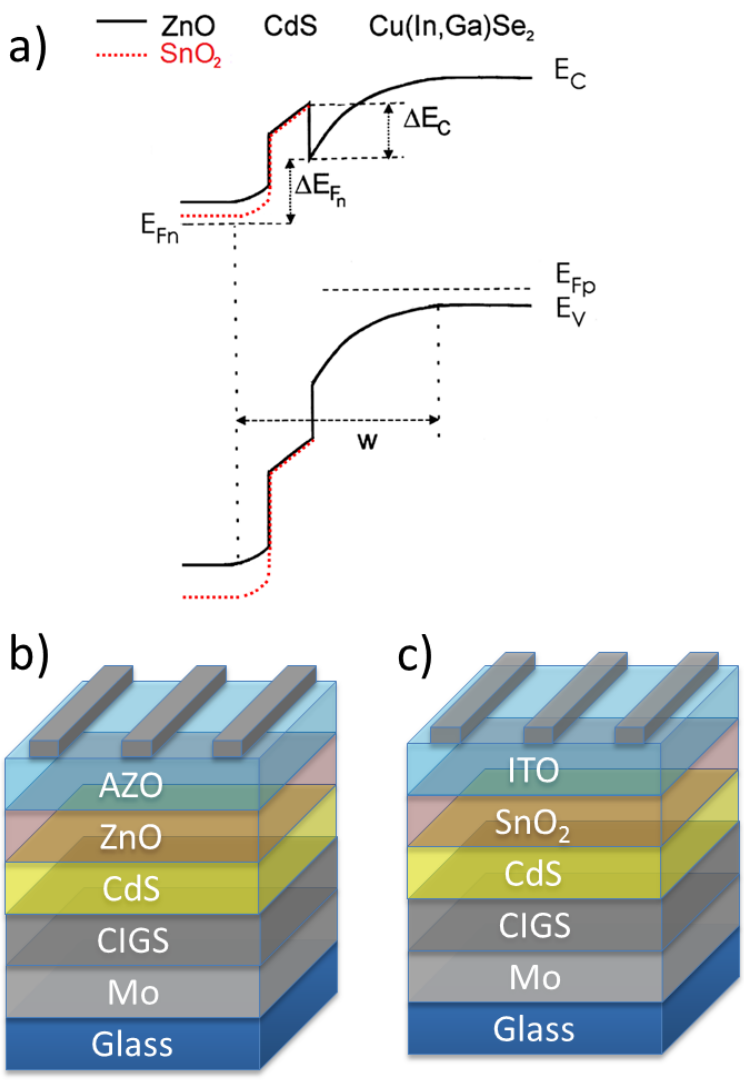

Figure 4.1. (a) Band alignment comparison between the SnO_2/CdS/CIGS and the ZnO/CdS/CIGS junctions. The CIGS solar cell designs with **(b)** SnO_2 and tin doped indium oxide layers and **(c)** with ZnO and aluminum doped zinc oxide layers.

Tin dioxide is more stable than zinc oxide at elevated temperatures (25-100 °C) and high relative humidity.[89] Pern *et al.* have studied the damp-heat degradation of transparent conducting oxides and showed that the damp-heat induced degradation rates followed Al-doped ZnO and $Zn_{1-x}Mg_xO$ >> tin doped indium oxide (ITO) > fluorine doped tin oxide.[90,91] They also evaluated the protective power of various films including those listed above and films such as indium zinc oxide on the underlying intrinsic ZnO, the buffer and absorber layers.[92] In the previous chapter[21] we showed that, a semi-

crystalline tin dioxide coating deposited on top of a finished CIGS solar cell protects the underlayers (ITO, ZnO, CdS and CIGS) from water and significantly increases the device lifetime. In that study, the tin dioxide layer was not a part of the solar cell circuit but acted as a protective overlayer. In this chapter, we consider replacing the traditional polycrystalline zinc oxide layer in the CIGS solar cell with semi-crystalline tin dioxide in order to improve the damp-heat stability of CIGS solar cells.

4.2. Experimental Details

The SnO_2 was selected to replace the ZnO because it is a more environmentally robust material with band gap and band alignment that are well-suited for use as a window layer in CIGS solar cells. SnO_2 has a wider band gap (E_g = 3.8 eV) than zinc oxide (E_g = 3.3 eV). Theory indicates that the band alignment in the SnO_2/CdS/CIGS junction is expected to be similar to that in the ZnO/CdS/CIGS junction and the two are compared in Figure 4.1(a). Electron affinities of ZnO has been reported between 4 and 4.6 eV[93-96] while the electron affinity of SnO_2 has been reported between 4.4 and 4.7 eV.[93,96,97] Electron affinity of SnO_2 has also been shown to vary depending on the oxygen vacancy concentration.[97,98] We sketched Figure 4.1(a) exaggerating any potential difference that may exist between ZnO-CdS-CIGS and SnO_2-CdS-CIGS band alignments. However, we expect the conduction band offset between the CdS buffer layer and the oxide window layer to either remain the same as in ZnO or increase slightly when ZnO is replaced with SnO_2. The similar device results reported below with ZnO and SnO_2 window layers suggest that the differences in alignment, if any, must be small *(vide infra).*

We replaced the ZnO window layer and the transparent conducting aluminum doped ZnO (AZO) layer in the traditional CIGS solar cell design with i-SnO_2 and tin doped indium oxide layers, respectively. These two cells designs are shown in Figures 4.1(b) and 4.1(c) and hereafter referred to as ZnO cells and SnO_2 cells, respectively. The i-ZnO and AZO or i-SnO_2 and ITO layers were deposited on identical CdS-CIGS

junctions: all the fabrication steps were identical except the deposition of the oxide layers. Specifically, approximately 2 μm thick CIGS absorber was deposited on molybdenum coated stainless steel foil by co-evaporation at 550 °C. Following, 40 nm thick CdS was deposited on the CIGS film through chemical bath deposition. The i-SnO_2 window layers were sputtered from a SnO_2 target using 150 W or 250 W plasma powers and were either 100 nm or 200 nm thick. Contacts to the AZO or the ITO layers were made with an evaporated Ni/Al grid, which was connected to a thicker bus bar at the edge of the foil for electrical contact. The solar cells were characterized under illumination with 100 mW/cm^2 AM 1.5 simulated solar spectrum. Illumination area was 0.47 cm^2. Each deposition condition was replicated on three different substrates and each substrate had eight solar cells.

4.3. Results and Discussion

Table 4.1 lists the average figures of merit for the control ZnO solar cells and solar cells assembled with two different thickness SnO_2 films deposited at two different sputtering powers. Figures 4.2(a) and 4.2(b) show the current-voltage (J-V) characteristics of the control ZnO solar cells and the highest performing SnO_2 solar cells from each deposition condition, respectively. Clearly, all the SnO_2 solar cells have similar figures of merit within the standard of deviation of reproducibility. Most importantly, the open circuit voltage (V_{OC}), short circuit current (Jsc), fill factor (FF) and the overall power conversion efficiencies (η) of the ZnO and SnO_2 solar cells are similar within the standard deviation. The highest average solar conversion was achieved with 200 nm thick SnO_2 window layer sputtered at 150 W. The main difference between these solar cells and solar cells assembled with SnO_2 deposited under other conditions is the FF and the J_{SC}. The 200 nm thick SnO_2 window layers consistently yielded higher FF due to larger shunt resistance. If the SnO_2 is fully depleted, the depletion region in the window layer reaches the transparent conductive oxide (TCO) layer and the presence of electric field increases the shunt current and therefore decreases the resistance. The higher shunt resistance is achieved when the depletion region is confined to the intrinsic SnO_2 layer

and a quasi-neutral electric field free region exists in the SnO_2 layer. Thus, the 200 nm thick SnO_2 films have higher shunt resistance, while 100 nm thick films are fully depleted. The slightly higher short circuit current with solar cells using SnO_2 window layer deposited at 150 W RF power is believed to be due to the higher light transmission through the SnO_2 window layers.

Table 4.1. Figures of merit for CIGS solar cells with SnO_2 as the window layer.

Name	RF power	Thick.	η (%)	FF (%)	V_{OC} (mV)	J_{SC} (mA/cm^2)	$R_{Sr,L}$ (Ω cm^2)	$G_{Sh,L}$ (mS/cm^2)
Control	N/A	N/A	8.13 ± 0.58	59.2 ± 2.6	459 ± 0.0	29.9 ± 1.1	2.93 ± 0.40	2.02 ± 0.46
1/2/3	150 W	100 nm	7.36 ± 1.04	59.5 ± 7.5	454 ± 6.0	27.2 ± 1.2	3.26 ± 1.28	3.86 ± 2.44
4/5/6	150 W	200 nm	8.11 ± 0.35	63.6 ± 2.3	452 ± 6.7	28.2 ± 1.0	2.21 ± 0.69	2.40 ± 0.08
7/8/9	250 W	100 nm	7.18 ± 1.48	58.7 ± 10.1	451 ± 4.9	27.0 ± 1.0	3.69 ± 2.27	3.16 ± 3.07
10/11/12	250 W	200 nm	7.54 ± 0.42	63.6 ± 0.9	448 ± 11.0	26.5 ± 0.9	2.40 ± 0.24	2.46 ± 0.64

The damp-heat stability of the SnO_2 solar cells was studied by measuring the solar cell figures of merit as a function of exposure time to damp-heat conditions (85 °C and 85 % relative humidity). The solar cells were unencapsulated during exposure to damp-heat conditions. The solar cells received a total of 120 hours exposure but were removed from the damp-heat test chamber every 24 hours to measure their J-V characteristics. The temporal evolution of the normalized solar cell figures of merit are shown in Figure 4.3. The figures of merit were normalized to their initial values, before the damp-heat test (t=0 hour). For comparison, Figure 4.3 also shows the evolution of the normalized solar cell figures of merit for a CIGS solar cell assembled with ZnO window layer and ITO TCO layer. Figure 4.3(a) shows that the CIGS solar cell made using ZnO window layer degrades rapidly over 120 hours of damp-heat test and losses more than 90% of its initial efficiency. In contrast, the solar cell made with 200 thick SnO_2 layer sputtered at 150 W retained 95% of its initial efficiency after 120 hours of damp-heat exposure. While not as impressive as this best case, other SnO_2 solar cells, also performed better than the ZnO solar cells and retained more than 50% of their initial efficiency after 120 hours of damp-heat exposure. Close examination of the evolution of the individual solar cell figures of

merit gives insight into the differences between the solar cells made with SnO_2 and ZnO. In both types of cells, the short circuit current decreased less than ~5% and remained approximately constant indicating that light absorption and charge separation remain largely unaffected with damp-heat exposure. In stark contrast, the evolution of the V_{OC} with damp-heat exposure is very different between the SnO_2 and ZnO solar cells. The V_{OC} of the SnO_2 solar cells remained constant over 120 hours of damp-heat exposure, while the V_{OC} of the ZnO solar cells declined to less than 30% of their initial value. Since, the decrease in the V_{OC} is associated with water permeation to the junction, we conclude that water permeation is significantly retarded or stopped in solar cells with SnO_2 window layer. Figures 4.3(e) and 4.3(f) show the evolution of the series and shunt resistances, respectively. The shunt resistance of the SnO_2 solar cells was more stable than the ZnO solar cells over the 120 hours of damp-heat exposure. In fact, the shunt resistance of the ZnO solar cells decreased by two orders of magnitude, which contributed significantly to the degradation of the fill factor. This, again, is consistent with retardation of water permeation through the SnO_2 window layer to the p-n junction. The series resistances of the SnO_2 and ZnO solar cells show a similar behavior and monotonically increase with damp-heat exposure. This increase is attributed to the increase in the resistivity of the transparent conducting oxide layers (e.g., ITO and AZO).[80,81] Despite this increase in the series resistance, the changes in the fill factor in both the ZnO and SnO_2 cells are attributed to the changes in the shunt resistance. For example, the precipitous drop in the ZnO solar cell FF correlates with the two order of magnitude drop in the shunt resistance. Similarly the gradual decrease in the FF of solar cells 1, 7 and 11 correlates with the slow decline in the shunt resistance. Even the unusual initial increase in the fill factor and efficiency in solar cell 4 correlate with the initial increase in shunt resistance for this cell.

The superior performance of the solar cell made with 200 nm thick SnO_2 film sputtered at 150 W is due to is microstructure. In chapter 2, we showed that SnO_2 films deposited under these conditions are semicrystalline and consist of nanocrystals embedded in an amorphous matrix.[20,21] These films do not have grain boundaries, which

eliminates grain boundary water diffusion across the window layer to the p-n junction. Figure 4.4 compares the x-ray diffraction from 200 nm thick ZnO and 200 nm SnO_2 films sputtered at room temperature using 150 W RF power. The polycrystalline ZnO film is textured and grows with its c-axis (002) oriented normal to the substrate surface. The SnO_2 film; on the other hand, is semicrystalline with SnO_2 nanocrystals embedded in an amorphous matrix. The broad feature in SnO_2 diffraction pattern at ~ 30º is from amorphous SnO_2.[21] The diffraction from crystalline regions are too small to be seen in x – ray diffraction but are clearly visible using transmission electron microscopy.[20,21] Despite this lack of grain boundaries, the SnO2 films still exhibit charge carrier mobilities that are adequate for solar cells.[21] Interestingly, coating a finished ZnO-CdS-CIGS solar cell with a ~200 nm thick SnO_2 film sputtered at 150 W also improves its damp-heat stability.[21] Moreover, light transmission is sacrificed by replacing ZnO with SnO_2 transmits more light to the underlying CIGS layer (Figure 4.5).

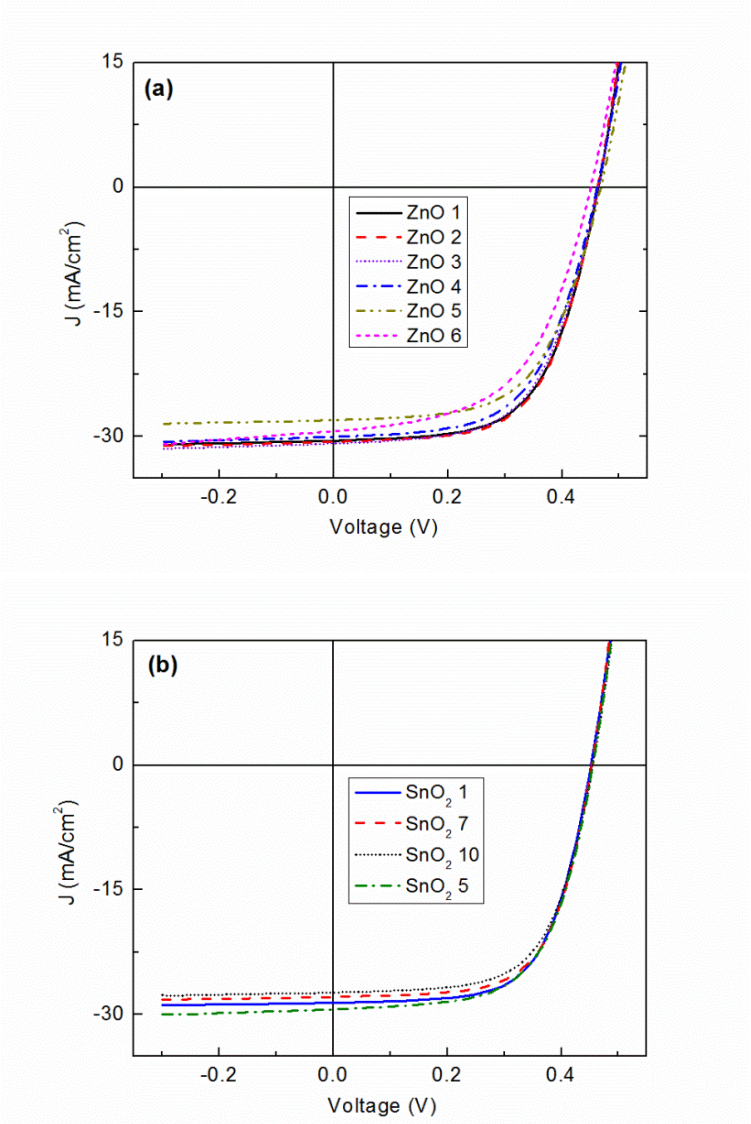

Figure 4.2. Current-voltage (J-V) characteristics of **(a)** the ZnO solar cells, and **(b)** the highest performing SnO_2 solar cells from each row of Table 4.1.

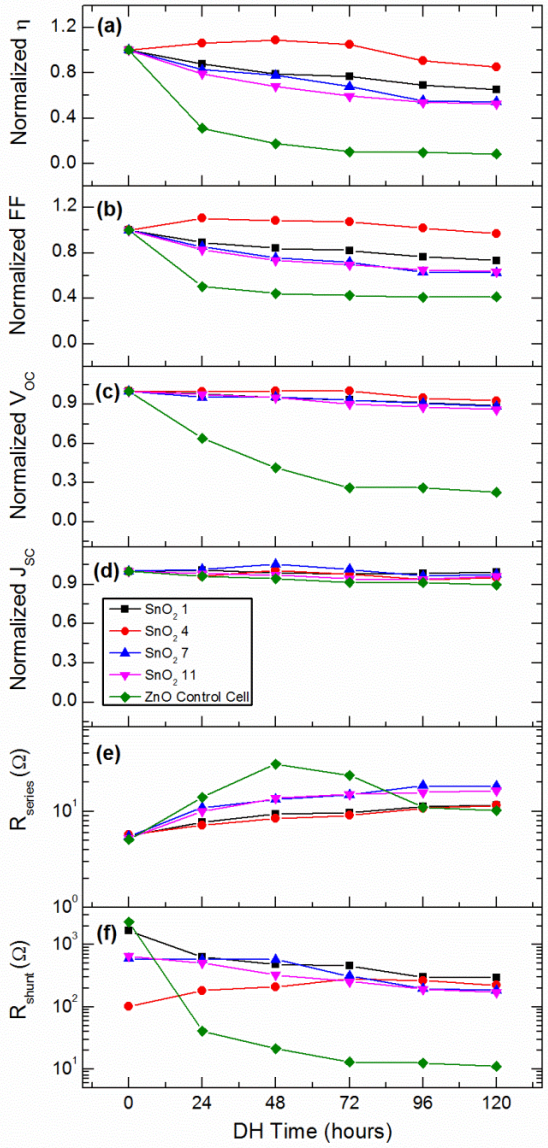

Figure 4.3. Temporal evolution of normalized **(a)** solar cell efficiency, **(b)** fill factor, **(c)** V_{OC}, **(d)** short circuit current, **(e)** series resistance, and **(f)** shunt resistance for ZnO and SnO_2 solar cells.

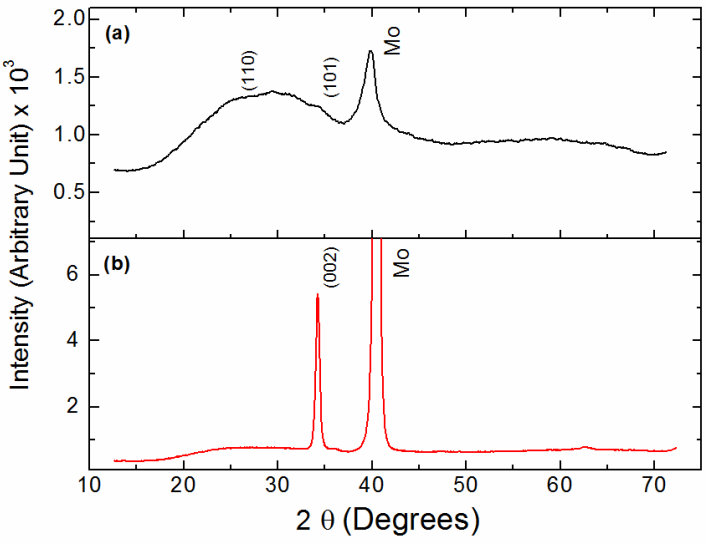

Figure 4.4. X-ray diffraction from 200 nm thick **(a)** SnO_2, and **(b)** ZnO films deposited on Mo-coated glass substrate at room temperature and using 150 W RF power.

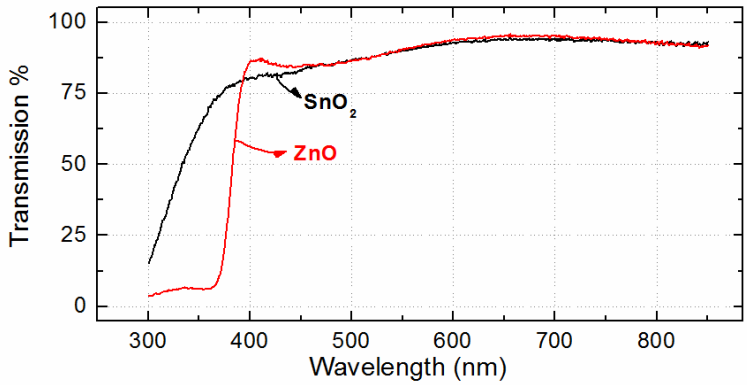

Figure 4.5. Comparison of optical transmission through a 200 nm thick SnO_2 and a 200 nm thick ZnO film deposited on glass at room temperature and using 150 W RF power.

4.4. Conclusions

In summary, we showed that ZnO window layer in CIGS solar cells can be replaced with SnO_2 with no decrease in the overall efficiency but with substantial gains in their damp-heat stability. Thus, replacing ZnO window layer with SnO_2 and coating the

finished solar cell with SnO_2 will reduce the requirements on solar cell encapsulation and increase the lifetime of the finished solar cells.

CHAPTER 5

Structure and Composition of $Zn_xCd_{1-x}S$ Films Synthesized through Chemical Bath Deposition

Zinc cadmium sulfide ($Zn_xCd_{1-x}S$) thin films grown through chemical bath deposition (CBD) are used in chalcopyrite solar cells as the buffer layer between the n-type zinc oxide and the p-type light absorbing chalcopyrite film. To optimize energetic band alignment and optical absorption, advanced solar cell architectures require the ability to manipulate x as a function of distance from the absorber-ZnCdS interface. In this chapter, we demonstrate the entire range of $Zn_xCd_{1-x}S$ thin films by CBD and examine the chemical composition of the films as a function of growing film thickness. We found that films are inhomogeneous and x varies significantly as function of distance from the film-substrate interface. Films with high overall Zn concentration ($x>0.5$) exhibit a Cd-rich layer near the film-substrate interface because Cd is more reactive than Zn. This layer is typically beneath a nearly pure ZnS film that forms after the Cd-rich layers are deposited and Cd is depleted in the bath. In films with high overall Cd concentration ($x<0.5$) the Zn concentration rises towards the film's surface. Fortunately, these gradients are favorable for solar cells based on low band gap chalcopyrite films.

5.1. Introduction

Amongst the second generation thin film solar cells, those based on the copper indium gallium diselenide ($CuIn_{1-x}Ga_xSe_2$ or CIGS) absorber have the distinction of having the highest overall power conversion efficiencies (20.3%).[99-102] The p-n junction in the CIGS solar cell is between a p-type CIGS absorber and a 50-100 nm thick n-type cadmium sulfide (CdS) layer grown on the CIGS through chemical bath deposition (CBD).[102-110] A nominally intrinsic oxide (e.g., ZnO) is deposited on the CdS film to complete the p-n junction and, for this reason, the CdS is often refered to as the buffer layer. The CBD-CdS buffer layer is crucial for achieving high efficiencies. CdS films have also been synthesized through other methods including molecular beam epitaxy,[111] metal-organic vapor phase epitaxy,[112] spray pyrolysis,[113] magnetron sputtering,[114] photochemical,[115] sol-gel,[116] and atomic layer deposition.[117] The main role of the CdS is to keep the Fermi level at the interface above the middle of the CIGS band gap. In addition, CdS is lattice-matched to CIGS and protects the p-n junction from physical damage during sputtering of ZnO.[109] Even though physical or chemical vapor deposition methods would be more convenient than CBD, solar cells made with CdS films deposited through these vacuum-based approaches have not been able to match the high efficiencies obtained using CBD-CdS. There appears to be a process in CBD that modifies the CIGS-CdS interface but this process is not easily duplicated in vacuum deposition. It has been suggested that the CBD process dopes the surface of the CIGS layer n-type and result in a buried homojunction within the absorber's subsurface region.[118] CBD-CdS films are also used in the emerging copper zinc tin sulfide (or selenide) based solar cells.[119,40]

Reducing CdS buffer layers by alloying or by completely replacing it with zinc sulfide (ZnS) has always been an interest.[23-36] The narrow band gap of CdS (E_g~2.4 eV) partially blocks the transmission of high-energy photons to the absorber layer below and decreases the power conversion efficiency. While thinner CdS layers maybe used to mitigate this blocking, very thin CdS layers result in low shunt resistance in the solar cells, and reduce the fill factor.[120,121] When CdS is replaced with ZnS, wider band gap of

ZnS leads to higher quantum efficiency in the blue region of the electromagnetic spectrum,[122] but despite this increase, the overall power conversion efficiency decreases from over 20% to 19%.[123] The decrease in the power conversion efficiency is attributed to the increase in the conduction band offset between CIGS and the ZnS buffer layer which results in lower short circuit current density (J_{sc}) and lower fill factor (FF).[124] Solar cells with buffer layers comprised of ZnS deposited on a very thin CdS were more efficient than solar cells with just CdS or just ZnS films.[124] The improved performance with this dual buffer layer architecture is attributed to the better band alignment at the CdS/CIGS interface and higher transmission through the ZnS.[124] An alternative and particularly elegant way to obtain higher transmission and improved performance is by using size quantized CdS.[125]

Multijunction CIGS-based solar cells require wider band gap absorber layers than CIGS such as copper indium aluminum gallium diselenide ($CuIn_{1-x-y}Al_yGa_xSe_2$ or CIAGS). In solar cells made with CIAGS films, the conduction band offset between the absorber and CdS layer will be larger, leading to increased recombination rates at the junction and lower solar cell efficiencies.[124,126] Depending on the band gap of the absorber layer (e.g., Al and Ga concentrations in the film), it is desired to adjust the band gap of the $Zn_xCd_{1-x}S$ buffer layer by adjusting x to reduce "cliff" and "spike" type discontinuities.[127] The ability to manipulate x as a function of distance from the absorber-$Zn_xCd_{1-x}S$ interface may also be desired to simultaneously optimize the energetic band alignment, the optical absorption and the internal electric field in the junction.

While $Zn_xCd_{1-x}S$ films have been deposited by CBD,[24,36,129] the structure and composition of these films have not been studied in detail. It is often assumed that the film composition (e.g., x) is homogenous in the direction normal to the substrate surface. In this chapter, we deposit and characterize $Zn_xCd_{1-x}S$ films with $0 \leq x \leq 1$ and show that the chemistry of the CBD method leads to a variety of film structures and composition variations within the film. These variations are brought about by the differences in the Cd and Zn ion reaction rates and equilibria.

$Zn_xCd_{1-x}S$ films are typically deposited from aqueous solutions containing thiourea, $ZnSO_4$, $CdSO_4$ and ammonia.[123] Ammonia complexes with the metal ions, increases the pH (~10.5) and decomposes the thiourea to release sulfur ions into solution.[129] The chemical reactions taking place in $Zn_xCd_{1-x}S$ CBD are listed in Table 5.1.[122]

Table 5.1. Important reactions in $Zn_xCd_{1-x}S$ CBD. Reactions (12)-(15) are important in presence of a chelating agent such as EDTA.

$SC(NH_2)_{2(s)} + OH^-_{(aq)} \leftrightarrow SH^-_{(aq)} + CH_2N_{2(aq)} + H_2O_{(aq)}$		(1)
$NH^{4+}_{(aq)} + OH^-_{(aq)} \leftrightarrow NH_{3(aq)} + H_2O$		(2)
$ZnSO_{4(s)} \leftrightarrow Zn^{2+}_{(aq)} + SO_4^{2-}{}_{(aq)}$		(3)
$CdSO_{4(s)} \leftrightarrow Cd^{2+}_{(aq)} + SO_4^{2-}{}_{(aq)}$		(4)
$Zn^{2+}_{(aq)} + 4\ NH_{3(aq)} \leftrightarrow [Zn(NH_3)_4]^{2+}_{(aq)}$	$K = 10^{8.9}$	(5)
$Cd^{2+}_{(aq)} + 4\ NH_{3(aq)} \leftrightarrow [Cd(NH_3)_4]^{2+}_{(aq)}$	$K = 10^{6.9}$	(6)
$SH^-_{(aq)} + OH^-_{(aq)} \leftrightarrow S^{2-}_{(aq)} + H_2O$		(7)
$Zn^{2+}_{(aq)} + 2\ OH^-_{(aq)} \leftrightarrow Zn(OH)_{2\ (s)}$	$K_s = 10^{-16}$	(8)
$Cd^{2+}_{(aq)} + 2\ OH^-_{(aq)} \leftrightarrow Cd(OH)_{2\ (s)}$	$K_s = 10^{-13.7}$	(9)
$Zn^{2+}_{(aq)} + S^{2-}_{(aq)} \leftrightarrow ZnS_{(s)}$	$K_{sp} = 10^{-24.7}$	(10)
$Cd^{2+}_{(aq)} + S^{2-}_{(aq)} \leftrightarrow CdS_{(s)}$	$K_{sp} = 10^{-27}$	(11)
$Zn^{2+}_{(aq)} + EDTA_{(aq)} \leftrightarrow Zn(EDTA)^{2+}_{(aq)}$		(12)
$Cd^{2+}_{(aq)} + EDTA_{(aq)} \leftrightarrow Cd(EDTA)^{2+}_{(aq)}$		(13)
$[Zn(NH_3)_{4-x}EDTA_x]_{(aq)} + SC(NH_2)_{2(aq)} + 2\ OH^-_{(aq)} \rightarrow [ZnS]_{(s)} + EDTA_{(aq)} + NH_{3(aq)} + CN_2H_{2(aq)} + H_2O$		(14)
$[Cd(NH_3)_{4-x}EDTA_x]_{(aq)} + SC(NH_2)_{2(aq)} + 2\ OH^-_{(aq)} \rightarrow [CdS]_{(s)} + EDTA_{(aq)} + NH_{3(aq)} + CN_2H_{2(aq)} + H_2O$		(15)

Metal sulfide CBD is understood in terms of two competing reaction mechanisms,[130,131] the ion-by-ion and cluster-by-cluster deposition mechanisms. The dominant mechanism is determined by many factors including the ratio of the free metal ions to complexing agent, pH, and concentration of metal ions. In the ion-by-ion deposition, the metal and the sulfur ions react heterogeneously to form the metal-sulfide, CdS or ZnS. This mechanism is operative when free Cd^{2+} and Zn^{2+} concentrations are low and, consequently, the deposition is slow.[129-133]. In addition, the ion-by-ion

deposition leads to larger crystals in the deposited films.[132] In cluster-by-cluster mechanism, the S^{2-} ions are thought to react with very small colloidal particles or clusters of metal-hydroxide either on the surface of the growing film or in the solution. This mechanism is thought to become increasingly more important as the concentrations of the precursors are increased.[129] Since the solubility product of CdS is smaller than that for ZnS (e.g., reaction 11 in Table 5.1), and $Cd(OH)_2$ reacts faster with S^{2-} than $Zn(OH)_2$, CdS growth is dominated by the ion-by-ion deposition mechanism, while ZnS growth is dominated by the cluster-by-cluster deposition mechanism. However, the deposition mechanism can be shifted from cluster-by-cluster to ion-by-ion mechanism by reducing the Zn^{2+} and Cd^{2+} ion concentration in the solution. This can be achieved by using strong chelating agents, such as ethylenediaminetetraacetic acid disodium (EDTA) or sodium citrate which slow the release of Zn^{2+} and Cd^{2+} ions to the solution[123] [reactions (12) and (13) in Table 5.1]. This strategy also results in lower hydroxide incorporation into the growing films.[133]

5.2. Experimental Details

The $Zn_xCd_{1-x}S$ films were deposited on 1 inch × 1 inch pieces of bare or Mo-coated Si (100) wafers. The 750 nm thick Mo film was deposited using sputtering. The substrates were cleaned ultrasonically in a de-ionized (DI) water, acetone and isopropanol mixture (1:1:1 ratio by volume) and dried by blowing compressed air across the substrate. A piece of kapton tape was used to cover a small section of the substrate to create a step for measuring the film thickness using a profilometer (KLA-Tencor P-16 Surface Profiler). During deposition, the CBD solution was stirred continuously using a 9.5 mm magnetic stirring bar at 400 rpm. The CBD solutions were prepared at room temperature by adding the following chemicals to DI water in order, cadmium sulfate ($CdSO_4$), ammonium hydroxide (NH_4OH), EDTA, zinc sulfate ($ZnSO_4$), and thiourea ($SC(NH_2)_2$). The total solution volume was 120 mL. In all depositions, the ammonium hydroxide concentration in the solution was kept constant at 3 M. The concentration of other reactants was changed to study their effects on the deposition rate and film properties.

Typically, the $ZnSO_4$ concentration was kept higher than $CdSO_4$ concentration because of the lower reaction rate of Zn. A 250 mL salted bath water was heated prior to start of the deposition to 103-105 °C and the beaker containing the CBD solution was placed in this bath at t=0 sec. In the meantime, the substrates were placed in the solution beaker. The beaker with the CBD solution and the substrates was placed in the heating bath after the bath reached 103 °C. The reaction solution started to become turbit within 8-15 minutes as both the solution and bath temperatures reach ~85 °C simultaneously. The substrates were kept in the heated CBD solution for 1-3 hours. The substrates were removed from the chemical bath after 1, 2 and 3 hours, rinsed with DI-water, ultrasonically cleaned and then dried using compressed air.

The film thicknesses were measured with a profilometer and confirmed with single wavelength and spectroscopic ellipsometry as well as scanning electron microscopy (SEM, Jeol 6500). Energy-dispersive X-ray spectroscopy (EDS, Thermo-Noran Vantage SIX) was used for the elemental analysis of the deposited films. The accelerating voltage was kept constant as 7.5 keV. The spatially averaged (across thickness and across lateral dimensions) elemental concentrations were determined using the π-ρ-z method with theoretical standard element sensitivity factors after subtracting the background from the acquired X-ray spectra. Mo $L_{\square}$ emission (2.29 keV) is very close to S $K_{\square}$ emission (2.306 keV) and they overlap in EDS. Hence the S concentration in the films deposited on Mo cannot be detected accurately. The structural properties of the films were studied using X-ray diffraction (XRD, Bruker-AXS) with Cu-K_α radiation (λ=0.154056 nm). The variation of the film's composition as a function of position perpendicular to the substrate surface was studied using depth profiling by Auger electron spectroscopy (AES, Physical Electronics Model 545), and film thicknesses (and, thus, Auger sputtering rates) were calibrated using spectroscopic ellipsometry measurements. Argon ions were used for sputtering during Auger depth profiling and the sputtering rate varied between 5.6 nm/min for CdS to 10.7 nm/min for ZnS.

If the EDTA concentration is too high for a given $CdSO_4$ or $ZnSO_4$ concentration, the chelation equilibrium leads to very low Cd^{2+} and Zn^{2+} concentrations and no film is

deposited. The appropriate EDTA concentrations were found by depositing CdS and ZnS using different $CdSO_4$-to-EDTA and $ZnSO_4$-to-EDTA ratios, respectively. Figures 5.1(a) and 5.1(b) show the regions of the $CdSO_4$-EDTA and $ZnSO_4$-EDTA planes where CdS and ZnS deposition is possible. Figure 5.1(a) and 5.1(b) show that CdS deposition requires a $CdSO_4$-to-EDTA ratio of at least ~0.3 and ZnS deposition requires a $ZnSO_4$-to-EDTA ratio of at least ~2.5. The higher surface roughness in Mo-coated Si (100) leads to film nucleation (or smaller incubation time) and deposition at low $ZnSO_4$-to-EDTA ratios which does not result in films on bare Si (100) substrates. In the no-deposition regions of Figures 5.1(a) and 5.1(b), the Si substrate is etched and Mo peels off the silicon. The EDTA concentrations in our experiments were guided by Figures 5.1(a) and 5.1(b). When depositing $Zn_xCd_{1-x}S$ films, we kept the overall EDTA concentration constant at 20 mM while changing the $ZnSO_4$ and $CdSO_4$ concentrations to achieve different x. $ZnSO_4$ and $CdSO_4$ concentrations were chosen to remain above the lines in Figures 5.1(a) and 5.1(b).

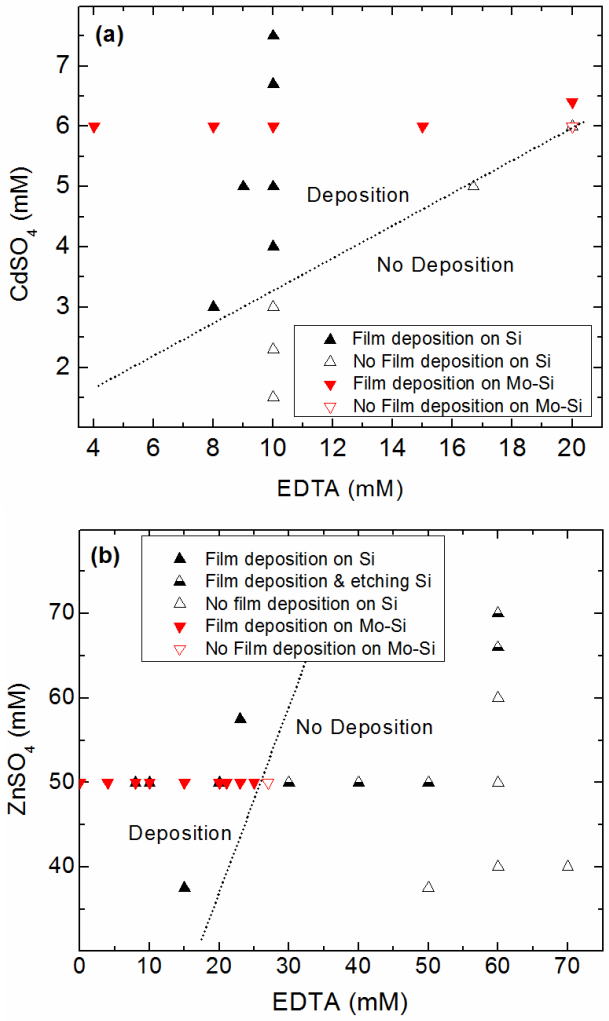

Figure 5.1. Region of the **(a)** $CdSO_4$-EDTA and **(b)** $ZnSO_4$-EDTA parameter space where (a) CdS and (b) ZnS films are obtained. The ammonium hydroxide and thiourea concentrations were kept constant at 3 M and 0.6 M, respectively.

5.3. Results and Discussion

5.3.1. Film Structure

Figure 5.2 shows the XRD patterns from films deposited with various initial $CdSO_4$ and $ZnSO_4$ concentrations on Mo-coated Si (100) substrates. The XRD from the Mo (110) diffraction at $2\theta = 40.7°$ is used as a reference. The films deposited only with

$ZnSO_4$ exhibit a broad asymmetric diffraction peak at ~ 29.2° shifted by 0.63° to higher 2θ values from the (111) diffraction peak of cubic ZnS (sphalerite) and from the (002) diffraction of hexagonal ZnS (wurtzite), which diffract at the same 2θ. This shift indicates a lattice strain of about 2.13 %. This contraction may be due to incorporation of O into the film: O was detected in the films by AES (*vide infra*). The asymmetry indicates the presence of some hexagonal ZnS. Indeed Figure 5.3 shows a deconvolution of the peak at $2\theta \approx 29.2^{o}$ into three contributions representing diffractions from the (100), (002) and (101) planes of hexagonal ZnS and from the (111) planes of cubic ZnS. The (002) diffraction from hexagonal ZnS and the (111) diffraction from cubic ZnS overlap and are represented using a single peak. Formation of cubic zinc blende is not surprising because ZnS is the thermodynamically stable phase at low temperatures.[134] Hexagonal phases can be incorporated into the growing film through the formation of stacking faults during low temperature growth. The addition of $CdSO_4$ to the growth solution incorporates Cd into the film (Table 5.1) and shifts the ZnS diffraction peak at $2\theta \approx 29.2°$ to lower angles. With enough $CdSO_4$ addition, three diffraction peaks corresponding to a hexagonal structure with lattice parameters close to those of CdS appear. These peaks seem to appear between x=0.76 and x=0.5 and grow as x decreases.[134] For example, the films deposited using 17 mM $ZnSO_4$ and 4 mM $CdSO_4$ (x= 0.09) clearly show the (100), (002) and (101) hexagonal CdS diffractions. The ratios of the (100), (002) and (101) peaks in CdS films deposited using $CdSO_4$ alone do not match the ratios expected from a polycrystalline diffraction pattern. Two-dimensional diffraction patterns show rings indicating that the films are not textured. Thus, we conclude that the CdS films (x=0) are primarily hexagonal with some cubic CdS incorporated in the film. We note that the XRD probes the entire film and the diffractions patterns for $Zn_xCd_{1-x}S$ films may contain more than one phase. For example, films where the average composition is between x=0 and x=1 may be mixtures of the cubic $Zn_yCd_{1-y}S$ and hexagonal $Zn_zCd_{1-z}S$ with z and y such that the overall composition is *x*.

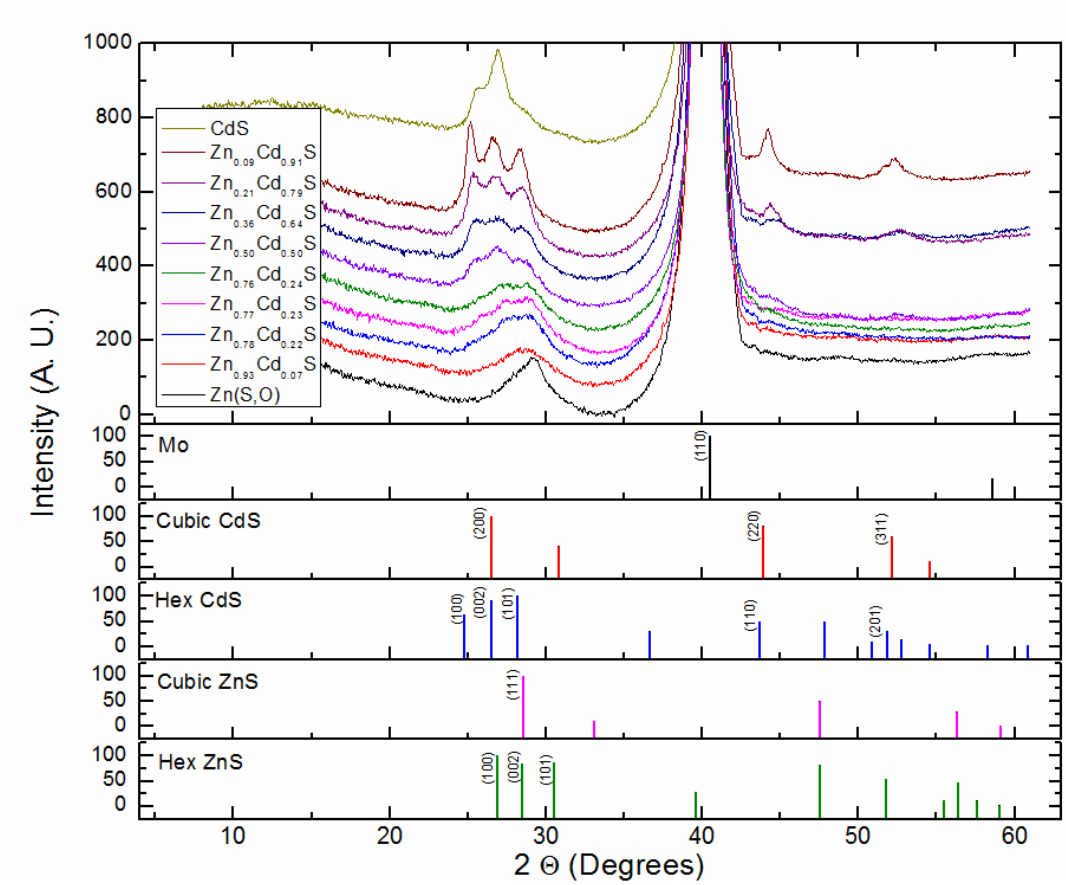

Figure 5.2. X-ray diffraction from $Zn_xCd_{1-x}(S,O)$ films deposited on Mo-coated Si (100) substrates for 3 h using various initial concentrations of $ZnSO_4$ and $CdSO_4$ in the CBD solution (please see the legend). Ammonium hydroxide, thiourea, and EDTA concentrations were 3, 0.6 and 0.02 M, respectively. XRD expected from various polycrystalline sulfides and Mo are shown below the experimental data.

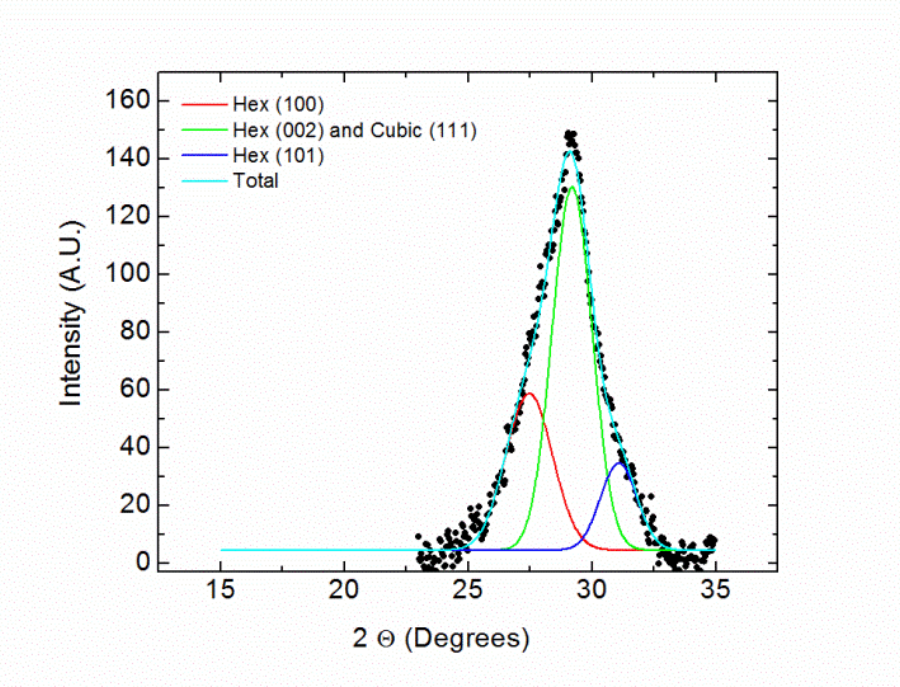

Figure 5.3. Deconvolution of the XRD peak at 2Θ = 29.2 into three contributions representing diffractions from the (100), (002), and (101) planes of hexagonal ZnS and from the (111) planes of cubic ZnS. The (002) and (111) diffractions appear at the same location and were fitted with a single peak.

5.3.2. Film Composition

Table 5.2 shows the $Zn_xCd_{1-x}(S,O)$ film composition as a function of the initial $CdSO_4$ and $ZnSO_4$ concentrations in the CBD solutions. These films were deposited on Mo-coated Si(100) substrates. Zn and Cd stoichiometry was calculated from EDS. The sulfur peak overlaps with that of Mo so that its concentration cannot be determined using EDS. From AES data we know that the films contain S and O so that we refer to these films as $Zn_xCd_{1-x}(S,O)$. Clearly, increasing the $ZnSO_4$ concentration in the solution increases the average Zn concentration, x, in the film though the increase is not linear with the solution composition, Figure 5.4 shows x vs $[ZnSO_4]/[CdSO_4]$ ratio. The average Zn concentration in the film increases linearly from 0 to ~0.75 with increasing $[ZnSO_4]/[CdSO_4]$ ratio. Increasing it beyond 0.75 requires a steeper increase in the $[ZnSO_4]/[CdSO_4]$ ratio.

Since the bath composition changes with time during the deposition, we expected Zn and Cd concentration gradients within the film. Consequently, we examined the film composition as a function of depth into the film using AES depth profiling. The $Zn_xCd_{1-x}(S,O)$ film thicknesses from spectroscopic ellipsometry in conjunction with the shifts in the AES spectra were used to locate the Mo-$Zn_xCd_{1-x}(S,O)$ film interface. The details of our approach for determining the film composition as a function of depth are as follows.

Table 5.2. Average composition and thickness of $Zn_xCd_{1-x}(S,O)$ films deposited on Mo-coated Si (100) substrates as a function of initial $ZnSO_4$ and $CdSO_4$ concentrations in the solution[α]

[$ZnSO_4$] (mM)	**[$CdSO_4$] (mM)**	**Thickness (nm)**	**$Zn_xCd_{1-x}(S,O)$**
50	N/A	204	Zn(S,O)
49	0.10	186	$Zn_{0.93}Cd_{0.07}(S,O)$
48	0.25	167	$Zn_{0.78}Cd_{0.22}(S,O)$
46	0.50	133	$Zn_{0.77}Cd_{0.23}(S,O)$
42	1.00	104	$Zn_{0.76}Cd_{0.24}(S,O)$
39	1.33	129	$Zn_{0.50}Cd_{0.50}(S,O)$
36	1.67	82	$Zn_{0.36}Cd_{0.64}(S,O)$
33	2.00	115	$Zn_{0.21}Cd_{0.79}(S,O)$
17	4.00	117	$Zn_{0.09}Cd_{0.91}(S,O)$
0	6.00	85	CdS

[α]Compositions correspond to films that were deposited for 3 h. Ammonium hydroxide, thiourea, and EDTA concentrations were kept constant at 3 M, 0.6 M and 0.02 M respectively. The ratio of [$ZnSO_4$] to [$CdSO_4$] concentrations is varied such as to lie above the lines in Figure 5.1(a) and 5.1(b).

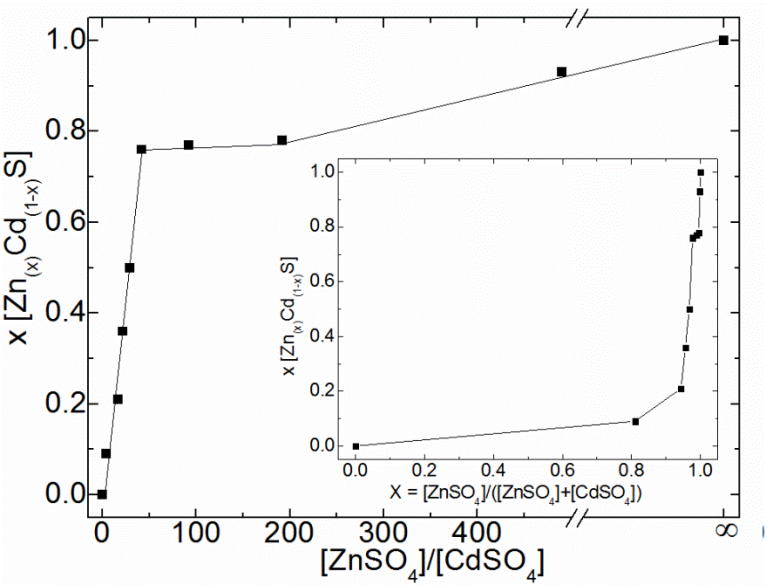

Figure 5.4. Composition variable *x* versus the $ZnSO_4$-to-$CdSO_4$ concentration ratio. The inset shows the composition variable versus the initial fraction of $ZnSO_4$ in the chemical bath, $x = [ZnSO_4]/([ZnSO_4] + [CdSO_4])$.

First, the thicknesses of the $Zn_xCd_{1-x}(S,O)$ films were determined using spectroscopic ellipsometry, which also provided information on the surface and interfacial roughness. The refractive index of the films for wavelengths longer than 550 nm (2.25 eV) could only be fit if the three-layer model shown in Figure 5.5 was used. The three-layer model consisted of an interfacial roughness layer between Mo and the $Zn_xCd_{1-x}(S,O)$ film, the $Zn_xCd_{1-x}(S,O)$ film, and a surface roughness layer. This model is shown schematically in Figure 5.5 along with a typical fit to a CdS film. The Cauchy equation was used for modeling the optical properties of the $Zn_xCd_{1-x}(S,O)$ films. The roughness layers between Mo- and the $Zn_xCd_{1-x}(S,O)$ and on the surface of the $Zn_xCd_{1-x}(S,O)$ film were modeled using the effective medium approximation. The former consisted of 50% Mo and 50% $Zn_xCd_{1-x}(S,O)$ and the latter consisted of 50 % voids and 50 % $Zn_xCd_{1-x}(S,O)$. The thicknesses of the three layers were adjusted to fit the optical data.

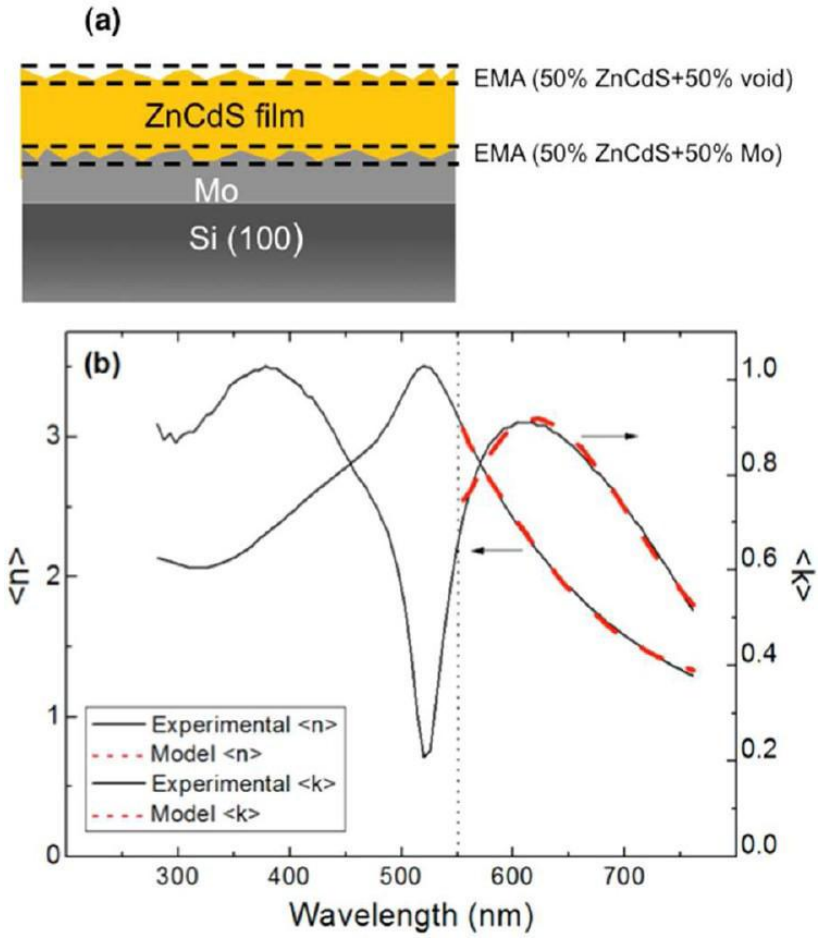

Figure 5.5. (a) Three-layer optical model of the film used for modeling the spectroscopic ellipsometry data. The film is modeled as consisting of three layers, an interface roughness layer model as a 50%/50% mixture of Mo and the sulfide film, the sulfide film and a surface roughness layer model as a 50%/50% mixture of voids and the sulfide film. The roughness layers are modeled using Bruggeman effective medium approximation. **(b)** A typical fit of pseudo-n and pseudo-k data for a CdS film.

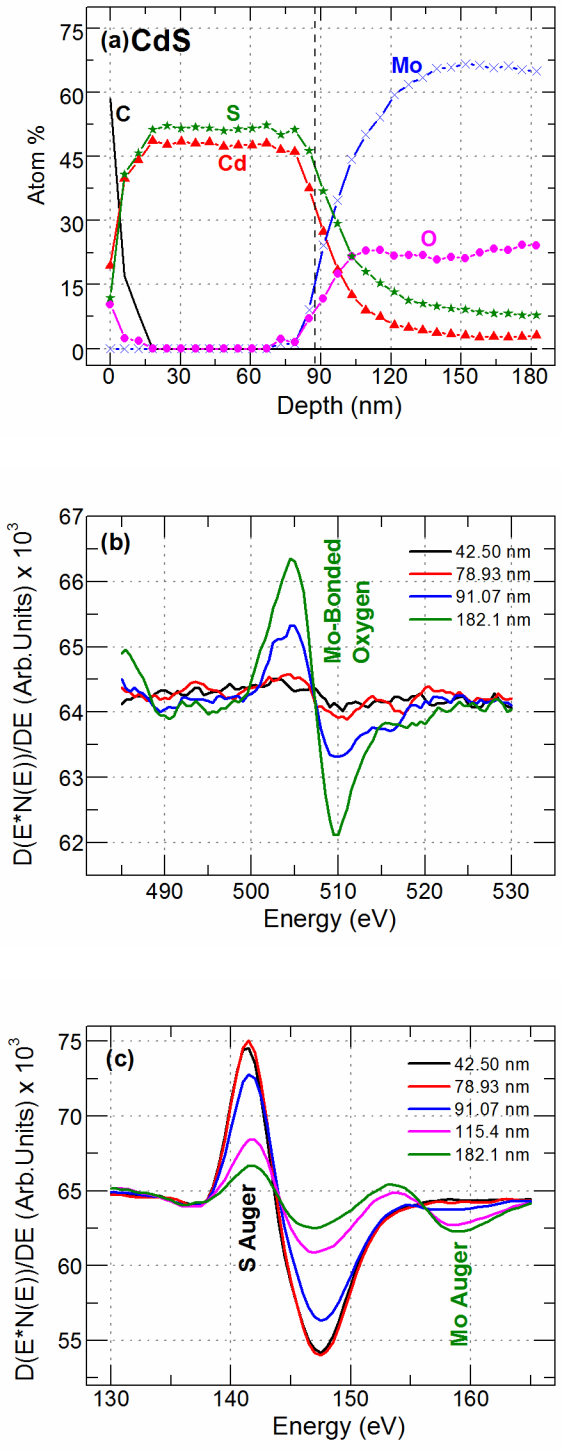

Figure 5.6. (a) Auger depth profile of an 85 nm thick CdS film deposited on Mo-coated Si (100) substrates, **(b)** oxygen region of the auger spectrum of this CdS film at different depths, **(c)** sulfur region of the auger spectrum of this CdS film at different depths.

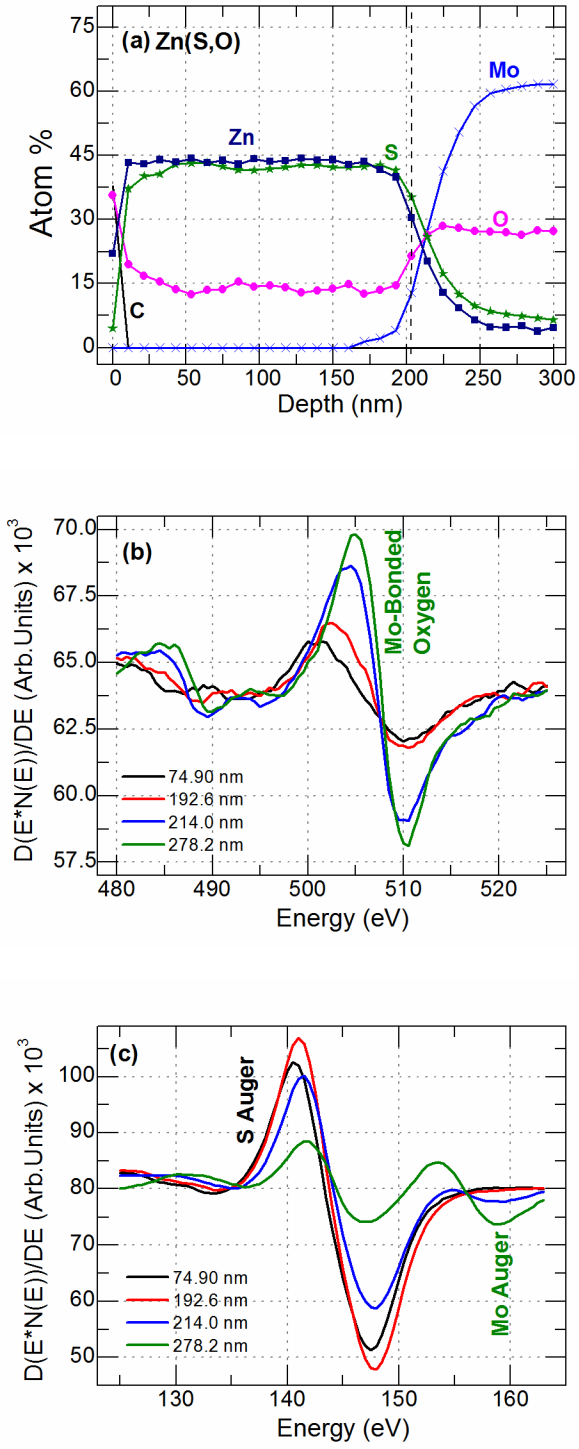

Figure 5.7. (a) Auger depth profile of an 204 nm thick ZnS film deposited on Mo-coated Si (100) substrates, **(b)** oxygen region of the auger spectrum of this ZnS film at different depths, **(c)** sulfur region of the auger spectrum of this ZnS film at different depths.

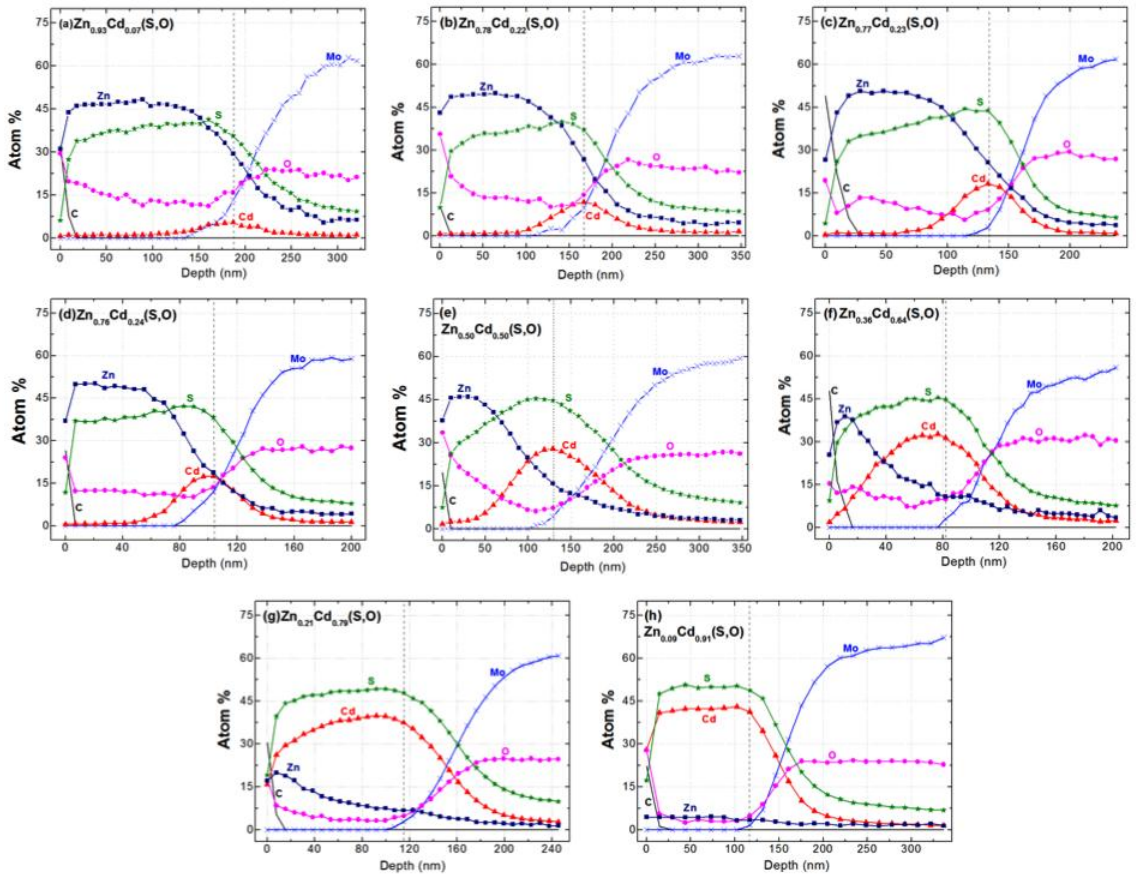

Figure 5.8. Auger depth profiles for **(a)** $Zn_{0.93}Cd_{0.07}(S,O)$, **(b)** $Zn_{0.78}Cd_{0.22}(S,O)$, **(c)** $Zn_{0.77}Cd_{0.23}(S,O)$, **(d)** $Zn_{0.76}Cd_{0.24}(S,O)$, **(e)** $Zn_{0.5}Cd_{0.5}(S,O)$, **(f)** $Zn_{0.36}Cd_{0.64}(S,O)$, **(g)** $Zn_{0.21}Cd_{0.79}(S,O)$, and **(h)** $Zn_{0.09}Cd_{0.91}(S,O)$ films.

Second, the location of the Mo-$Zn_xCd_{1-x}(S,O)$ film interface was determined from the shifts in the AES peaks. The AES of the elements, especially anions, showed characteristic shifts at the Mo-$Zn_xCd_{1-x}(S,O)$ film interface. The spectrum at which the shift occurred was assigned to be the interface and the depth at that point was taken to be the value of the top two layers of the 3-layer optical model film thickness determined using spectroscopic ellipsometry.

For example, Figure 5.6(a) shows the elemental Auger depth profile of an 85 nm thick CdS film. Figures 5.6(b) and 5.6(c) show selected Auger electron spectra recorded as one approaches and sputters through the Mo-CdS film interface. There are two indications when sputtering reaches the Mo-CdS film interface. First, as the sputtered

surface reaches the Mo layer, the oxygen Auger peak increases (Figure 5.6(b)). Our Mo films always contain oxygen both due to incorporation during sputtering and due to grain boundary oxidation after the film is taken outside the sputtering chamber. Oxidation of the grain boundaries may also be taking place in the basic CBD solution prior to CdS nucleation and growth. This residual oxygen was convenient to locate the interface between the CdS and the Mo films. The shift in the sulfur and the rise in the Mo Auger spectra are two additional indicators of the Mo-$Zn_xCd_{1-x}S$ film interface. Figure 5.6(c) shows that there is a very small but detectable shift in the S Auger peak accompanied by the appearance of the Mo Auger peak at ~153 eV as the Mo-CdS interface is reached. We assign the spectrum at which we begin detecting Mo and O to a depth of 85 nm, the sum of the surface roughness layer (~20 nm) and the bulk CdS film (~65 nm) thicknesses. The Auger depth profile shows a uniform CdS film between ~15 nm and ~85 nm. Adventitious C and O are detected at the surface, which decay to the noise level after sputtering approximately 15 nm of the film's surface, about the thickness of the surface roughness layer. Both cadmium and sulfur are detected well into the Mo film indicating significant diffusion, most likely due to diffusion along the Mo grain boundaries.

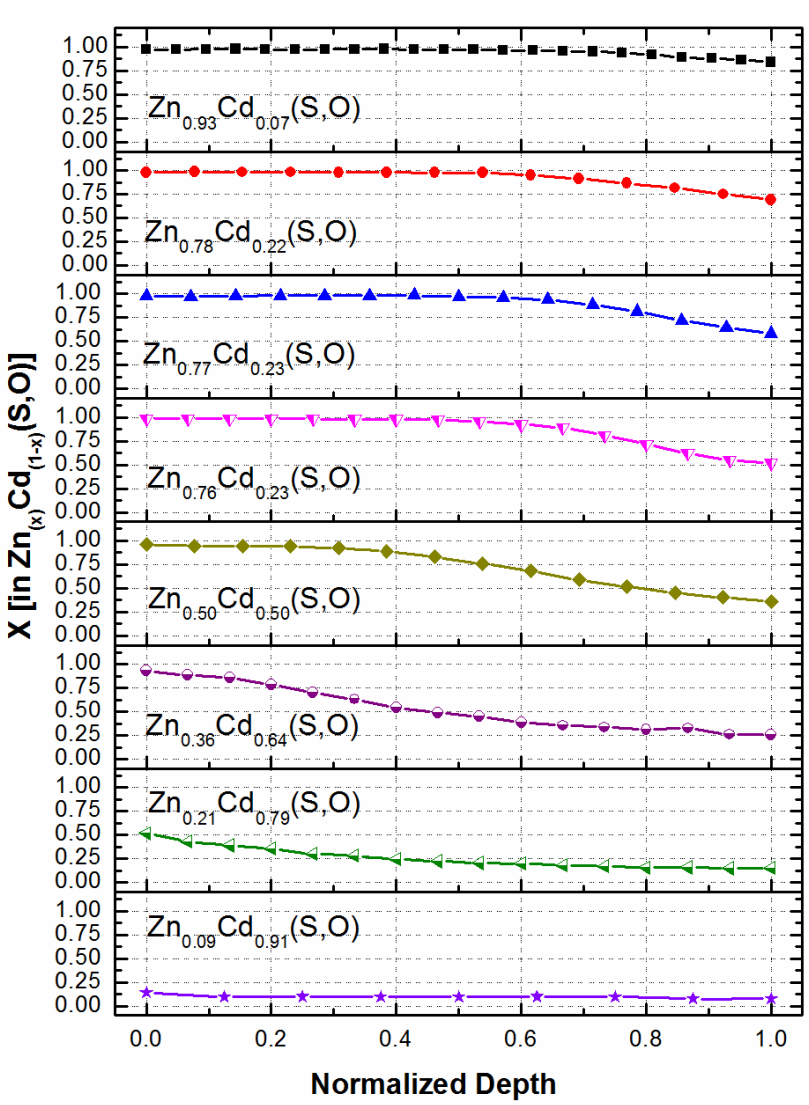

Figure 5.9. Film composition x as a function of dimensionless position in $Zn_xCd_{1-x}(S,O)$ films.

Figure 5.7(a) shows the elemental Auger depth profile of a 204 nm thick ZnS film. Figures 5.7(b) and 5.7(c) show selected Auger electron spectra recorded as one approaches and sputters through the Mo-ZnS film interface. The ZnS film shows 15% oxygen incorporation in the film.

Figure 5.8 shows the Auger depth profile for $Zn_xCd_{1-x}(S,O)$ films where the spatially averaged *x* is varied by changing the initial $ZnSO_4$ and $CdSO_4$ concentrations

(Table 5.1). Figure 5.9 shows the corresponding variation of *x* as a function of depth. All depth profiles show that the film composition is not homogeneous and *x* varies along the film thickness. The underlying reason behind the concentration gradients is the different reactivities of Cd^{2+} and Zn^{2+} and the differences in the solubility products of CdS and ZnS. The solubility product of CdS is smaller than ZnS, which leads to faster nucleation and growth of CdS as compared to ZnS.[122] For example; Figure 5.8(a) shows the Auger depth profile for the $Zn_{0.93}Cd_{0.07}S$ film. The Cd concentration in the film is highest near the Mo-$Zn_{0.93}Cd_{0.07}S$ interface and decreases slowly towards the film's surface. It appears that this film is cubic ZnS with Cd incorporated into this cubic lattice to form an alloy. Although the thickness-averaged Cd concentration is 7 %, it decreases monotonically from approximately 18 % near the Mo surface to nearly zero at the film surface. This decrease is due to rapid depletion of Cd through homogeneous nucleation and growth. Similar Cd concentration depth profiles are observed in films where the average x is lower. For example, Figure 5.8(b) shows the Auger depth profile for the $Zn_{0.78}Cd_{0.22}S$ film. The Cd concentration decreases monotonically from 38 % near the Mo surface to nearly zero within 70 nm of the interface. The thickness-averaged Cd concentration in this film is approximately 22 % even though the top 80 nm of the film is entirely ZnS. Interestingly, a wide range of $ZnSO_4$-to-$CdSO_4$ ratios (40-200, Figure 5.4) give films with nearly the same overall composition (Table 5.1 and Figures 5.8(b)-8(d)) but with different film thicknesses.

Figure 5.8(e) shows the Auger depth profile for a film that has equal amounts of Zn and Cd concentrations ($Zn_{0.5}Cd_{0.5}S$). Figure 5.9(e) shows that the first 30 nm of this film near the Mo-$Zn_{0..5}Cd_{0.5}S$ interface is Cd-rich (*x*=0.33, ~33 % Zn and ~67 % Cd). Towards the surface the Zn concentration rises while Cd concentration decreases such that the top layers of the film are nearly all ZnS with very little Cd. The O and S concentrations show the opposite trends in the top 100 nm of the film. The O concentration in the film follows that of Zn, rising with increasing Zn concentration while the S concentration decreases. This is consistent with the fact that $Zn(OH)_2$ reacts

slower with S^{2-} than $Cd(OH)_2$ which leads to higher O concentration in regions of the film that grow after Cd has been depleted.

Figures 5.8(f), 5.8(g) and 5.8(h) show the Auger depth profiles from films with average composition of x=0.36, x=0.21 and x=0.09, respectively. In these cases, there is enough Cd in the CBD solution such that Cd is not depleted significantly during the growth and the entire film is $Zn_xCd_{1-x}(S,O)$. For x=0.36 and x=0.21, Zn is incorporated into the film nonuniformly and the Zn concentration rises monotonically from the Mo surface towards the film surface. For the film with x=0.09, the Zn incorporation and film composition appears uniform on the scale of Figure 5.9 though there is a slow linear increase towards the surface.

When the initial CBD solution contains both $CdSO_4$ and $ZnSO_4$, we always observe a Cd-rich film near the interface with Mo. This is the desired concentration profile for buffer layers to be used with low band gap CIGS films because the conduction band offset is minimized. Moreover, increasing the Zn concentration towards the film surface would increase the light transmission by widening the band gap of the film towards the surface of the film.

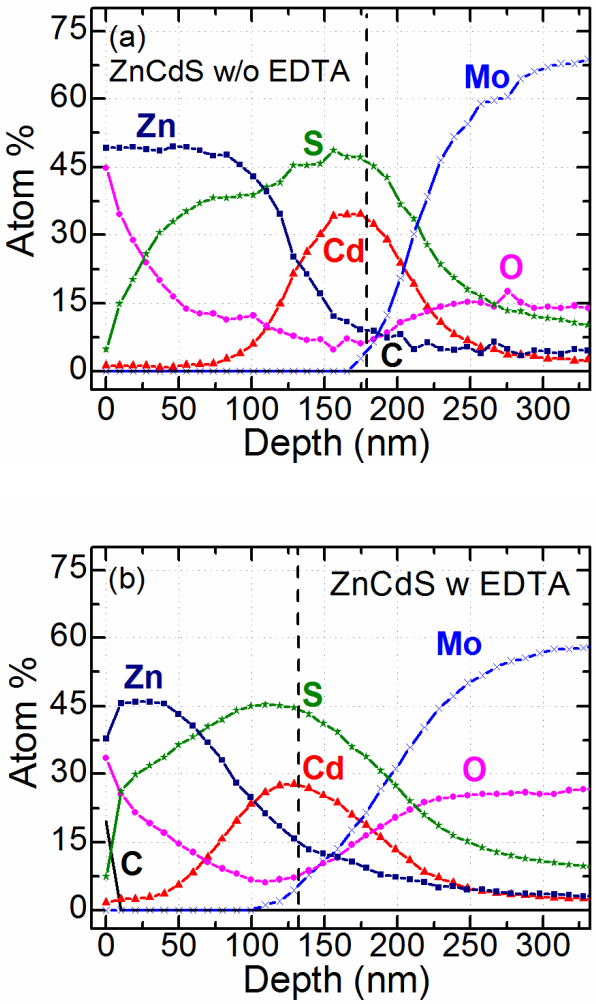

Figure 5.10. Auger depth profiles for films deposited **(a)** without and **(b)** with 0.02 M EDTA added to the chemical bath. Ammonium hydroxide, thiourea, $ZnSO_4$ and $CdSO_4$ concentrations were 3 M, 0.6 M 39 mM and 1.33 mM, respectively.

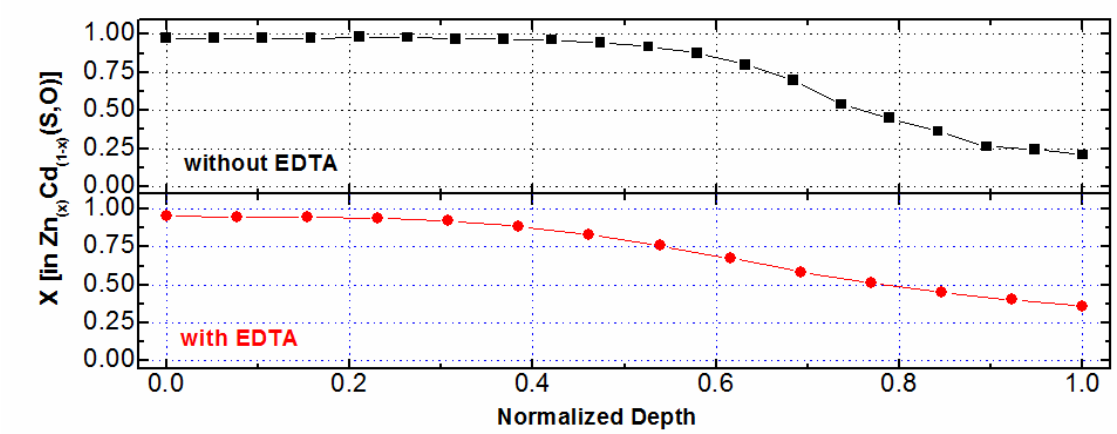

Figure 5.11. Film composition *x* as a function of dimensionless position in films deposited with and without EDTA. The films and the deposition conditions are same as those in Figure 5.10.

5.3.3. Effect of EDTA on the composition depth profile

Finally, we discuss the effects of EDTA on the Cd- and Zn-concentration depth profiles. All the films discussed so far have been deposited with EDTA added to the deposition solution. Addition of EDTA into the chemical bath slows down the deposition rate and results in more gradual changes in the Zn and Cd concentrations as a function of depth in the film than when EDTA is not used. Figure 5.10 compares the Auger depth profiles of the films deposited with and without EDTA. When EDTA is used, more Zn is incorporated into the film during the initial stages of the deposition and Zn concentration gradient becomes more gradual. This is most obvious from Figure 5.11, which shows variation of zinc fraction, *x*, as a function of depth. Cd-rich and Zn-rich layers appear more segregated when EDTA is not used. Addition of EDTA also appears to decrease O incorporation most likely due to EDTA chelation of Zn. Zn chelation decreases the zinc ion concentration and slows down the zinc hydroxide formation in the solution. This, in turn, decreases the oxygen concentration in the film.

5.4. Conclusions

The structure and chemical composition of $Zn_xCd_{1-x}(S,O)$ films deposited using the CBD method were studied in detail. ZnS and CdS films are primarily cubic and hexagonal, respectively. These are the predicted thermodynamically stable phases for ZnS and CdS. The Zn-rich films (e.g. $x>0.5$) are primarily cubic ZnS with Cd incorporated into the film. For these films, the Cd concentration decreases from the film-substrate interface towards the film's surface. In fact, depending on the deposition time, Cd in the bath can be depleted completely such that the top portion of the film is ZnS. This Cd-rich region near the interface is attributed to faster reaction of Cd compared to Zn. The composition gradients that yield Cd-rich region near the substrate surface are favorable for solar cells based on low band gap CIGS films.

CHAPTER 6

Efficient Continuous-Flow Chemical Bath Deposition of CdS Films as Buffer Layers for Chalcogenide-Based Solar Cells

The highest power conversion efficiencies in copper indium gallium diselenide (CIGS) solar cells are achieved when a cadmium sulfide (CdS) buffer layer is deposited on the CIGS absorber through chemical bath deposition (CBD). These CdS buffer layers are also used in emerging kesterite solar cells such as those based on copper zinc tin sulfide/selenide (CZTS/Se). In a typical CBD system, the entire solution, including the substrate, is heated. This leads to homogeneous nucleation of the metal sulfide particles in addition to the heterogeneous reaction that deposits the desired buffer layer on the substrate. This homogeneous nucleation and growth of particles consumes chemicals by creating toxic waste. In this chapter, we describe a novel continuous-flow chemical bath deposition (CF-CBD) system for efficient utilization of chemicals during CdS film deposition without homogeneous nucleation. CdS films are grown on 10-cm-diameter molybdenum-coated silicon wafers to demonstrate the potential of the method to achieve uniform thin CdS films.

6.1. Introduction

The CdS buffer layer is crucial for achieving high efficiencies and is deposited on the CIGS film using chemical bath deposition (CBD) for many reasons. For instance, CBD-CdS dopes subsurface of the CIGS layer n-type to create a buried homojunction as mentioned in Chapter 1 earlier. CdS buffer layers are also used in other chalcopyrite and kesterite thin film solar cells such as those based on the emerging material copper zinc tin sulfide/selenide (CZTSSe).[40] Uniform deposition of CdS films on large-area solar cells is challenging but necessary for mass production. Moreover, traditional batch-type chemical bath deposition wastes the reactants because homogenous reactions form CdS particles. In fact, nearly all of the Cd in the bath ends up in homogeneously nucleated CdS particles. Thus, the CBD process, while simple, produces large volumes of waste. Herein, we demonstrate a scalable continuous flow chemical bath deposition (CF-CBD) approach that produces uniform CdS films without homogeneous nucleation of particles. We demonstrate deposition on 10-cm-diameter substrates but the approach is easily scalable and even adaptable for roll-to-roll processing.

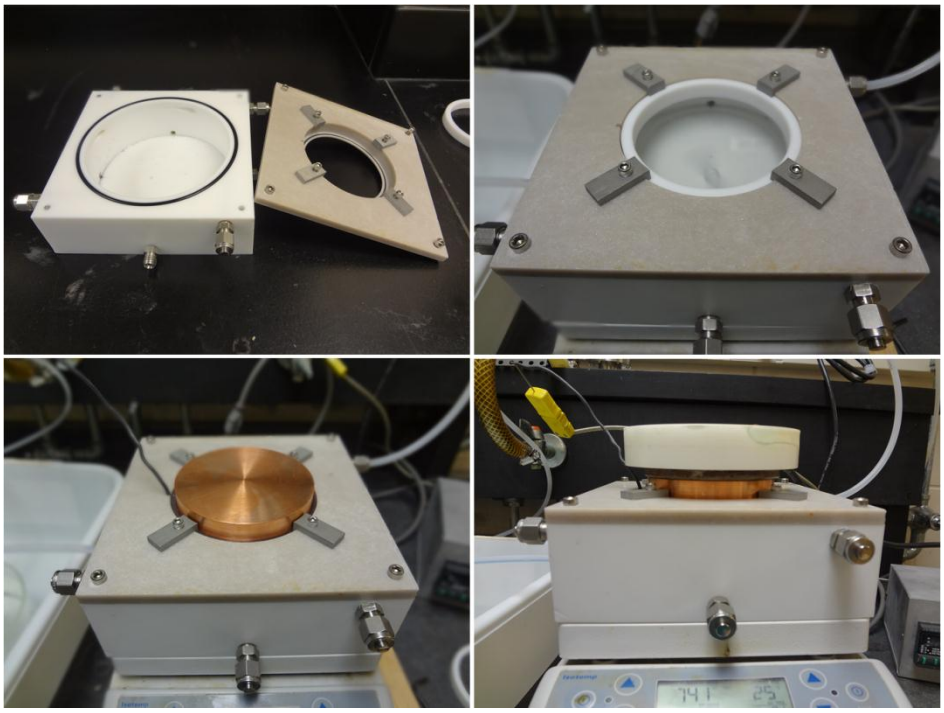

Figure 6.1. The continuous-flow chemical bath deposition system

6.2. Experimental Details

Cadmium sulfide films were grown on Mo-coated single-crystal Si substrates using aqueous solutions containing $CdSO_4$ (~ 0.0015 M), thiourea (~ 0.6 M), and NH_4OH (~ 3 M). In the traditional CBD approach, the solution and the substrate are both heated to the deposition temperature. This traditional approach has been used for the last two decades. Nonetheless, CBD wastes much of the reactants because CdS forms both homogeneously in the solution as particles and heterogeneously on the substrate as a thin film. To eliminate homogeneous nucleation, we designed and built a novel continuous-flow CBD (CF-CBD) system that heats only the substrate to the deposition temperature while continuously circulating the reactant solution between the bath, where the deposition takes place, and a chilled reservoir. Hence, the CBD solution remains near room temperature during deposition and reacts only at or near the substrate surface. Figure 6.1 shows the digital photographs of the continuous-flow CBD system at different stages of this assembly. During depositions, the bath is stirred continuously with a

magnetic stir bar, while the substrate is mounted on a heated copper block upside down. We measured the temperatures of the substrate and of the solution circulating through the bath as a function of time during deposition and found that the substrate temperature rises to within 5 ^{o}C of the set point in 10 minutes while the CBD solution remains below 27 °C. Keeping the solution cool eliminates the homogenous nucleation reaction, which would otherwise form CdS particles and waste chemicals. Visual examination of the solution before and after reaction confirms that the homogeneous particle formation is reduced significantly in CF-CBD compared to the traditional batch CBD. After deposition, the solution from the traditional CBD process is visibly turbid due to the homogenous CdS particle formation. In contrast, the solution from the CF-CBD system remains clear with a slight yellow tint, which indicates that the homogenous reaction that forms CdS particles is largely eliminated by maintaining the CBD solution at low temperature. Below we show deposition results at 85 °C and discuss the effects of stirring rate and surface roughness on the deposition uniformity. The CdS films were characterized using x-ray diffraction (XRD), spectroscopic ellipsometry, and atomic force microscopy (AFM).

6.3. Results and Discussion

The CdS films deposited by both traditional CBD and CF-CBD show primarily hexagonal crystal structure.[37] Figure 6.2 shows x-ray diffraction from two CdS films deposited by (a) traditional CBD, and (b) CF-CBD. CdS films deposited with the CF-CBD approach exhibit more intense (002) peaks per unit thickness compared to traditional CBD indicating that the crystallinity of the CF-CBD films are at least as good or better than the films deposited through traditional CBD. This improvement in crystallinity is attributed to the slower film growth in the CF-CBD system.

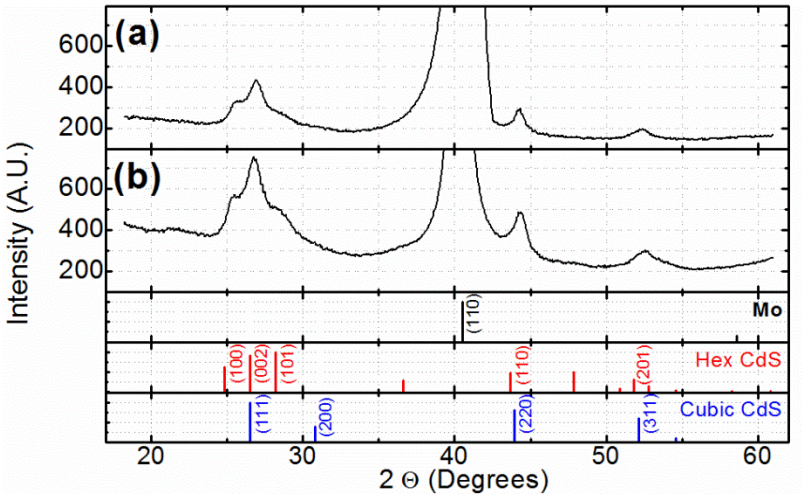

Figure 6.2. XRD patterns from CdS films deposited at 85 °C using **(a)** traditional CBD, and **(b)** CF-CBD.

Stirring rate, which determines the angular velocity of the fluid near the substrate surface, affects the deposition uniformity. Figure 6.3 shows CdS films deposited on Mo-Si substrates at 85 °C with stirring rates of 450 rpm, and 725 rpm for 2 h. As shown in the photographs of the deposited films (left) and the film thickness measured by spectroscopic ellipsometry (right), increasing the stirring rate improves the deposition uniformity. Figure 6.3(a) shows that, at 450 rpm stirring rate, the film thickness increases towards the edges of the substrate. A large bulls eye pattern is also visible in the center of the substrate. Increasing the stirring rate to 725 rpm (Figure 6.3(b)) results in visibly more uniform films with the exception of a small circular region in the center of the substrate. Indeed, detailed spectroscopic ellipsometric measurements of the film thickness across the substrate shows that the film thickness as a function of radial position across the substrate varies in a complicated manner. Starting from the center of the substrate, the film thickness first increases very steeply over a span of 0.5 cm and then decreases, again very steeply, to a constant value. The film thickness remains constant for 2 cm and then increases again towards the edges of the substrate. This variation can be explained by considering the fluid flow below the substrate during the deposition. The fluid motion generated by a rotating magnetic stir bar creates a vortex and funnel region above the stir bar. In closed systems, the liquid in the vortex funnel

region is stagnant and the size of this region shrinks with increasing rotation speed. This flow pattern affects the local heat and mass transport rates near the substrate surface. These transport rates in turn determine the radial variation of the temperature, T(r) and precursor concentrations, C(r) across the substrate. Since the deposition rate increases exponentially with temperature and is proportional to the precursor concentration, the film thickness reflects these variations. The fluid near the center is stagnant and we expect the heat transfer coefficient to be small in this region. Consequently, the center of the substrate above the vortex should be hotter. However, this stagnant region also leads to rapid depletion of precursors near the center of the substrate. Consequently, the precursor concentration at the center of the substrate is lower than the region away from this stagnant region. Figure 6.4 illustrates the expected radial variation of the temperature and precursor concentrations. Inside the stagnant region the temperature is high but concentration is low which leads to low, deposition rates. Outside the stagnant region, the concentration is high but the temperature is low, which also leads to low deposition rates. In a small transition region the deposition rate is maximized as illustrated in Figure 6.4 and as observed in Figure 6.3(b).

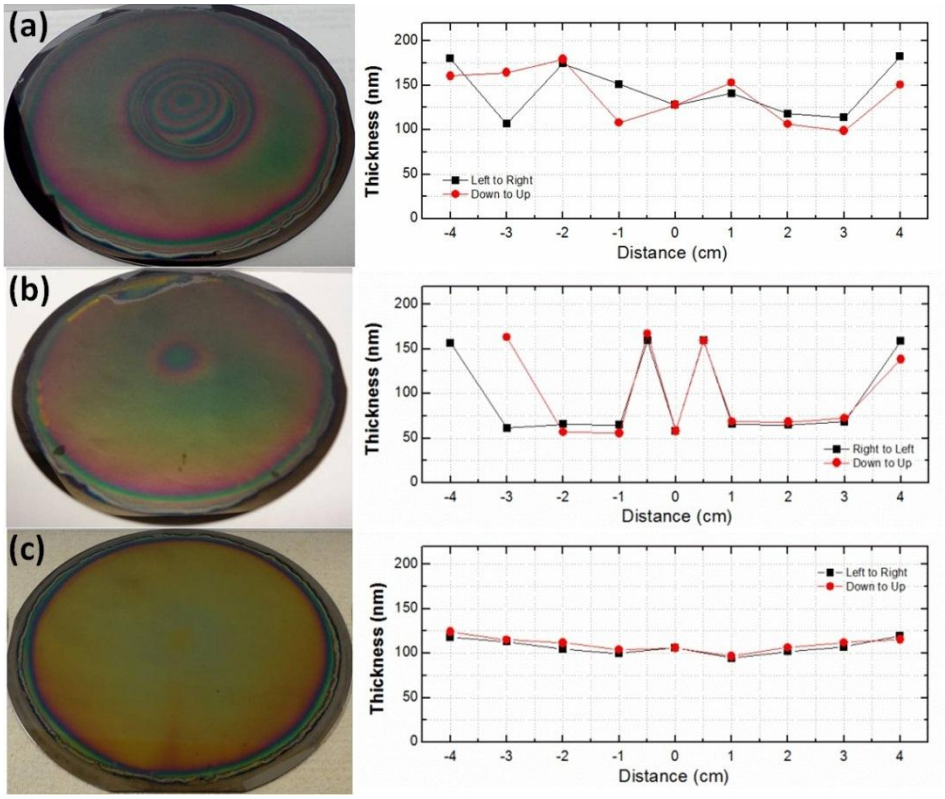

Figure 6.3. CdS films deposited using CF-CBD at 85 °C with **(a)** 450 rpm, **(b)** 725 rpm stirring rates on Mo-coated Si wafers where the Mo was sputtered at 10 mTorr (rms roughness=3.5 nm), and **(c)** 725 rpm stirring rate on Mo-coated Si where the Mo was sputtered at 5 mTorr (rms roughness=12.3 nm).

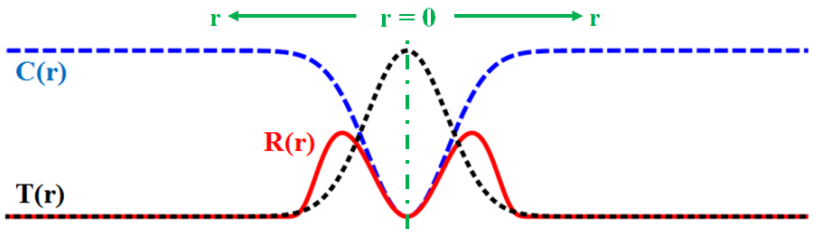

Figure 6.4. Expected radial concentration, C(r), temperature, T(r), and deposition rate, R(r), profiles.

We found that the film thickness uniformity is also a strong function of the substrate surface roughness. Deposition on rough substrate surfaces is more uniform than deposition on smooth substrate surfaces. We surmise that this difference is due to a difference in the film nucleation rate and density on smooth versus rough films. We use

Mo-coated Si substrates as a proxy for the CIGS covered substrates and we control the Mo surface roughness by controlling the Mo sputtering conditions. We surmise that increasing the Mo surface roughness increases the nucleation centers and decreases the time between nucleation events. On rough surfaces, nucleation is rapid, dense and uniform, which leads to uniform films. In contrast, nucleation events on smooth surfaces are separated in time and therefore not uniform. Consequently film thickness can vary significantly as a function of position. For example, Figure 6.3(a) shows a CdS film deposited at 85 ˚C and 450 rpm for 2 h on Mo-coated Si substrates where the Mo was sputtered in 10 mTorr Ar: a Mo film with 3.5 nm rms roughness results under these conditions (Figure 6.5). As both the photograph and SE thickness profiles show, the film deposited on this Mo surface is not uniform. Increasing the stirring rate to 725 rpm (Figure 6.3(b)) on Mo with 3.5 nm rms roughness improves the uniformity somewhat but the standard deviation of the film thickness is still more than 40% across the substrate. Increasing the Mo layer roughness by sputtering at lower pressure (5 mTorr) helps to deposit a more uniform CdS film. Figure 6.3(c) shows a CdS film deposited at 85 ˚C and 725 rpm for 3 h on Mo sputtered at 5 mTorr. A Mo film with 12.3 nm rms roughness results under these conditions (Figure 6.5). Both the photograph and the thickness measured by ellipsometry shows that the uniformity is improved significantly. The standard deviation of the film thickness is 6% for the CdS film shown in Figure 6.3(c). We note that a small nonuniform region at the center of the substrate is still apparent to the eye even in Figure 6.3(c) but the nonuniformity due to the effect described in Figure 6.4 is greatly reduced.

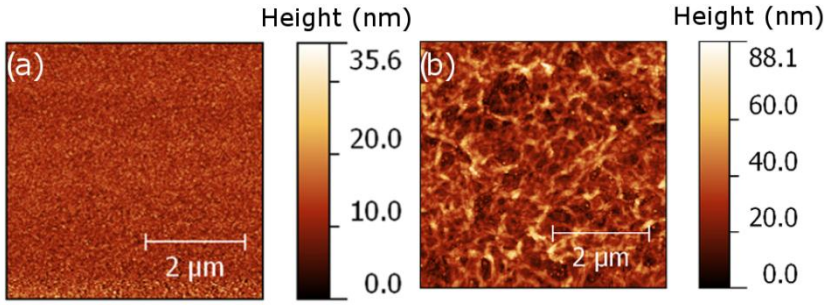

Figure 6.5. Dynamic mode AFM images of Mo-Si sputtered at **(a)** 10 mTorr, and **(b)** 5 mTorr.

Finally we confirmed that the surface roughness of the Mo changes with the sputtering pressure. Dynamic ("tapping") mode AFM images of Mo films sputtered at 250 W with (a) 10 mTorr, and (b) 5 mTorr Ar process pressure are shown in Figure 6.5. The roughness, averaged over five 5 x 5 mm^2 regions, is 3.5 nm and 12.3 nm for Mo sputtered at 10 mTorr and 5 mTorr, respectively.

6.4. Conclusions

CdS films were deposited by continuous-flow chemical bath deposition from aqueous solutions of $CdSO_4$, NH_4OH, and thiourea on 10-cm-diameter Mo-coated Si substrates. Only the substrate is heated to deposit CdS film. Loss of Cd through homogeneous nucleation is reduced significantly. The CF-CBD approach should be scalable to large areas and even to roll-to-roll deposition strategies. The uniformity of CdS films depends strongly on the stirring rate and the substrate surface roughness. CdS films deposited using both traditional CBD and CF-CBD approaches showed similar structural properties by XRD. The CF-CBD can produce ~50-120 nm thick films, varying less than 6% in thickness across a 10-cm-diameter substrate.

CHAPTER 7

Continuous-Flow Chemical Bath Deposition of Buffer Layers for Chalcopyrite and Kesterite Thin Film Solar Cells

Kesterite and chalcopyrite thin film solar cells have an n-type metal sulfide (e.g., CdS, ZnS or $Zn_xCd_{1-x}S$) buffer layer, which is typically grown using chemical bath deposition (CBD). CBD, while simple, wastes a significant amount of chemicals because metal sulfide particles nucleates and grows homogenously during the film deposition. This homogenous growth of metal sulfide particles also produce copious amount of toxic waste. In the chapter 6, we presented a continuous-flow chemical bath deposition (CF-CBD) approach for sustainable and low cost manufacturing of these buffer layers. In this chapter, we demonstrate $Zn_xCd_{1-x}S$ film depositions with uniform thickness on 10-cm-diameter molybdenum (Mo) coated silicon (Si) substrates by using CF-CBD approach. Moreover, we showed that CF-CBD can deposit blending $Zn_xCd_{1-x}S$ films with both uniform and graded elemental depth profiles.

7.1. Introduction

The interest in replacing the cadmium sulfide (CdS, E_g~2.4 eV) with alternative buffer layers, primarily with zinc sulfide (ZnS, E_g ~ 3.7 eV), originates from the desire to mitigate parasitic absorption in the blue region of visible spectrum in solar cells.[23-36,120] The narrow band gap of CdS decreases the quantum efficiency of the solar cells and, thus, their short circuit current density (J_{SC}); for example by 6 mA/cm^2 compared wide band gap ZnS.[123] However, CIGS based solar cells completed with ZnS buffer layers show lower power conversion efficiencies (19%) compared to CIGS solar cells completed with CdS buffer layers (20%).[124] The lower power conversion efficiencies with the ZnS buffer layers have been attributed to the increase in the energetic misalignments of ZnS with the absorber layers, which results in lower J_{SC} and a lower fill factor in the solar cells.[125] Solar cells that are completed first with a very thin CdS, and then with a ZnS layer showed higher efficiencies compared to solar cells using only CdS or ZnS buffer layers.[125] The improvement in the performance is related to the better energetic band alignments at the CdS/CIGS interface and higher quantum efficiency through the ZnS.[125] Alloying CdS buffer layers with ZnS, namely $Zn_xCd_{1-x}S$, is expected to lead better band alignments and quantum efficiencies than the two layer approach due to the smoother transition of the electrical properties.

A sustainable and low cost manufacturing of zinc-cadmium sulfide ($Zn_xCd_{1-x}S$) buffer films is necessary for large scale and cost effective solar cell module production, but challenging with traditional chemical bath deposition (CBD) approach. In a typical CBD process, the entire solution including the substrate is heated. One drawback of this approach is that a significant fraction of the reactants are consumed through homogenous nucleation and growth of CdS particles. A very small fraction of the reactants end up on the substrate as a film. Consequently, although simple, the traditional CBD process produces large volumes of hazardous waste. Even though, there had been reports on continuous feeding of reaction solution for CBD systems for $Zn_xCd_{1-x}S$ film depositions recently;[138] the deposited film properties as a function of depth and the uniform film

deposition, especially across large-scale (10 cm in diameter) substrates has not been studied.

In this chapter, we demonstrate a scalable continuous-flow chemical bath deposition (CF-CBD) system, shown in Figure 7.1, for uniform deposition of CdS, ZnS, and $Zn_xCd_{1-x}S$ films that eliminates homogenous nucleation and growth of particles. In the CF-CBD process, only the substrate surface is heated, while the chemical bath solution is kept around room temperature by circulation through an ice bath. Figure 7.2 shows a typical variation of the substrate and the solution temperatures as a function of time while the substrate is heated to deposition temperatures (85 °C). The substrate reaches to within 10 % of the deposition temperature set point in the first 10-15 minutes, while the reaction solution remains below 27 °C during the entire deposition period. Thus, a temperature gradient is created in a thin boundary layer next to the substrate, which limits the CdS forming reactions to the substrate surface and perhaps a very small volume near the substrate surface. Thus, the majority of the Cd precursor is utilized only for the film formation; and waste by homogeneous particle formation is minimized. Figure 7.2 insets illustrate the efficient utilization of Cd precursor by comparing the CBD solutions after 2-hours of deposition using traditional batch and CF-CBD methods. The solution before deposition is shown on the right, and it appears clear and colorless. The solution after 2-hour of traditional CBD deposition of CdS at 85 °C is shown on the left and appears turbid and yellow due to the homogenously formed CdS particles. The solution after 2-hours of CF-CBD of CdS at 85 °C is shown in the center photo and appears clear with a very slight yellow tint. The slight yellow tint is due to low density of CdS nanoparticles that form in the very small volume near the substrate. This yellow tint disappears entirely when ethylenediaminetetraacetic acid (EDTA) is added to the bath (*vide infra)* and the solution looks clear and colorless just as the starting solution shown in the right inset of Figure 7.2.

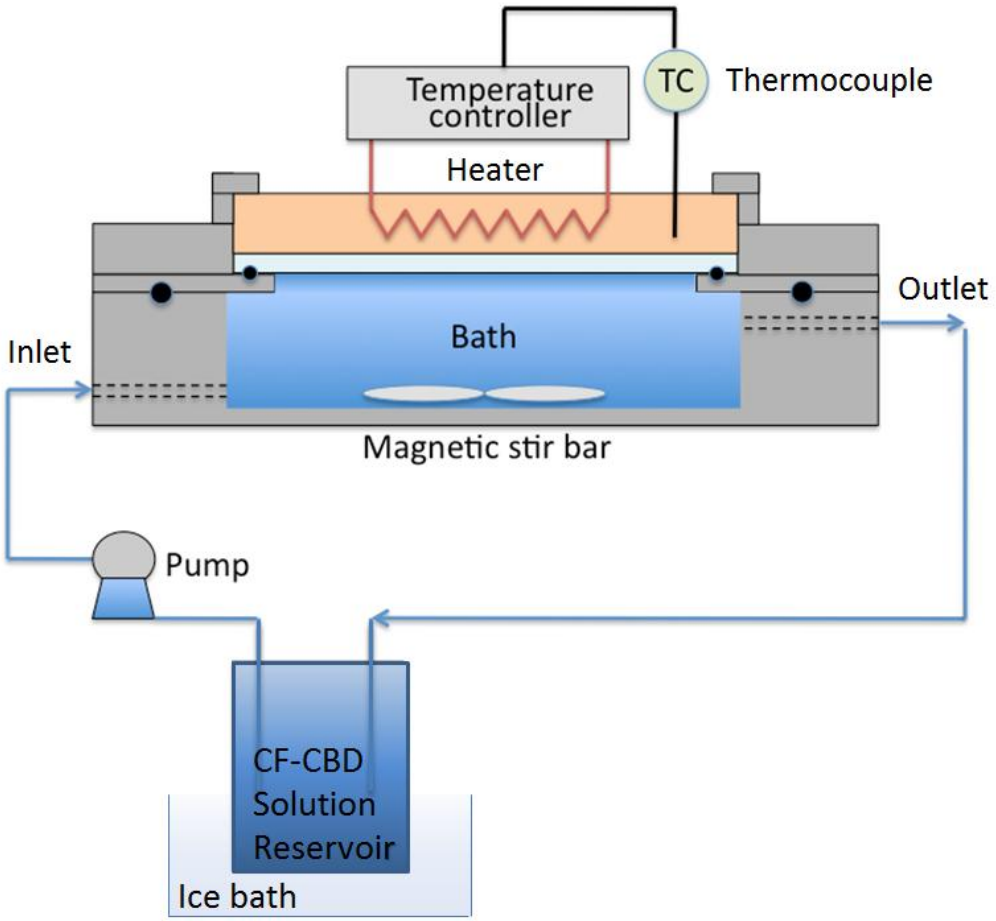

Figure 7.1. A schematic of the continuous-flow chemical bath deposition (CF-CBD) system. In CF-CBD only the substrate is heated while the solution is kept cool by circulating it through an ice-bath.

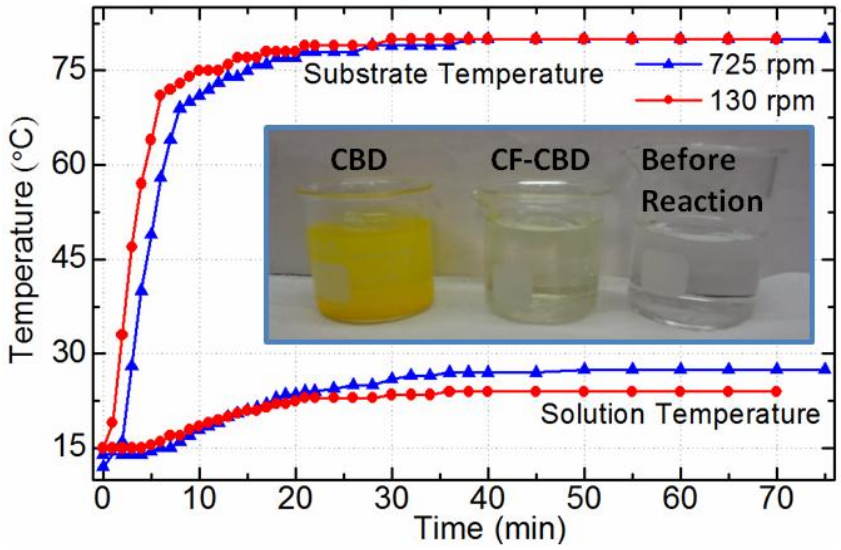

Figure 7.2. A typical temporal variation of the substrate and solution temperatures during deposition. The substrate surface is heated to reaction temperature (e.g., 80-85 °C), while the solution temperature is kept below 30 °C. The inset shows the chemical bath solutions after 2 hours of growth via traditional CBD (left), and CF-CBD (middle). The precursor solution before the reaction is shown on the right.

7.2. Experimental Details

Using the CF-CBD apparatus shown in Figure 7.1, the CdS, ZnS and $Zn_xCd_{1-x}S$ films were deposited on molybdenum (Mo) coated (100) oriented single crystal silicon (Si) 10-cm-diamater substrates (Mo-Si) through the CF-CBD design. Sputtered molybdenum (~250 nm) is used as a proxy for the CIGS absorber layer: some surface roughness is needed to activate the nucleation and growth of the buffer layers, and Mo and CIGS have similar surface roughness that initiates nucleation and growth. The Si (100) substrates were cleaned ultrasonically in a mixture of de-ionized (DI) water, acetone, and isopropanol (IPA) (1:1:1 ratio by volume), and then dried by blowing compressed air. The substrate is mounted with the Mo coating facing the bath solution. An approximately 1 mm thick (and 10-cm-diameter) SLG is stacked on top of the Mo-Si wafer as a proxy of the heat transfer for the depositions on the absorber layers using SLG substrates. Following, a ~2 cm thick (and 10-cm-diameter) copper (Cu) plate is placed on the glass for uniform heat transfer across the radian of Mo-Si substrate. The sealing is done by using rubber o-rings between the substrate and the reactor frame, and by

clamping down the Cu plates with stainless steel nails from the ceramic top of the reactor. The heater ring plate is mounted to the grove on the top of the Cu plate. A PI-type temperature controller is used with a single-point thermocouple inserted closer to the substrate surface and the radial center of the Cu plate. The deposition solution is prepared at room temperature by adding the precursors into DI water in the order of $CdSO_4$, EDTA, $ZnSO_4$, NH_4OH, and Thiourea. In all depositions, NH_4OH concentration was kept at 3 M, while the concentrations of other reactants were changed to study the effects of solution composition on the film properties. $ZnSO_4$ concentration was always kept by ~10 times higher than $CdSO_4$ because Cd^{2+} is more reactive than Zn^{2+} in forming the respective sulfides. The total solution volume is kept at 1 liter. First, the bath is filled with the ~600 mL CBD solution using the pump with at 800 mL/min. Following, the solution beaker is immersed into the ice bath and the substrate heating is begun with the temperature controller (t=0 s) set to predetermined deposition temperature, while the rest of the solution in the reservoir, the pump, and the tubes is chilled by circulating through the ice-bath. During the deposition, the solution using in the bath (~5 cm depth and ~12.3 cm diameter) is mixed vigorously using a 5 cm magnetic stir bar from 0-725 rpm. After a predetermined period deposition, the heater is turned off and removed from top of the Cu plate. The system is left for natural cooling until the substrate temperature drops below 35 °C, while the solution is still stirred, circulated and chilled. After 35 °C (or below) is reached, the solution is evacuated from the bath (reaction chamber), and the substrate is removed. Subsequently, the substrate is rinsed with DI water, ultrasonically cleaned, and then dried by blowing compressed air.

The special variation of the film thickness on the substrate was measured using spectroscopic ellipsometry, and confirmed with cross sectional scanning electron microscopy (SEM). The spectroscopic ellipsometry data was modeled using a three layer optical model that consisted of a roughness layer between the substrate and the film, the film, and a surface roughness layer.[37] The layer thicknesses are fitted as a Cauchy dielectric. The structural properties of the films were studied using x-ray diffraction (XRD, Bruker-AXS) with Cu-K_α radiation (λ=0.154056 nm). The change in the chemical composition as a function of film depth was studied using depth profiling via Auger

electron spectroscopy (AES, Physical Electronics Model 545); the Auger sputtering rates, with argon ions, is calibrated using the film thickness obtained from spectroscopic ellipsometry measurements. The change in the crystallographic structure and *d*-spacing of the unit cells as a function of depth was studied using a high-resolution transmission electron microscope (HRTEM) and selected area electron diffraction (SAED) from the cross-section of the alloys.

7.3. Results and Discussion

7.3.1. Film Uniformity

The radial uniformity of the film thickness is a strong function of the stirring rate. When the stirring rates are sufficiently high, the CF-CBD can deposit ~50-120 nm thick CdS films with less than 8% variation in film thickness across a 100-mm-diameter substrate. Increasing the stirring rate increases the angular velocity of the fluid near the substrate surface and improves the deposition uniformity. For example, Figure 7.3 shows digital photographs of CdS films (left) and the radial variation of the film thickness as measured by spectroscopic ellipsometry (right) as a function of the bath stirring rates. The films shown in Figures 7.3(a), (b) and (c) were deposited at 50 °C for 2 hours using 130 rpm, 450 rpm, and 725 rpm stirring rates, respectively. At low stirring rates, the film thickness increases towards the edges. Clearly, increasing the stirring rate, to 450 rpm (Figure 7.3(b)) and 725 rpm (Figure 7.3(c)), results in visibly more uniform films, while reducing the deposition rate at the periphery of the substrate. The fluid motion generated by magnetic stir bars in circular geometries creates a vortex and a funnel region above the stir bar.[139,140] In closed systems, the liquid in the vortex funnel region is stagnant, while the liquid outside this region mixes with a uniform angular velocity. Thus, in the CF-CBD system, the radial variation of the reactant concentrations and the temperature at the substrate surface are functions of the rotation speed, resulting in local changes in the deposition rates. The heated copper plate at the back of the substrate creates a uniform heat flux to maintain the set-point temperature. However, the heat removal rate by the fluid flow may be nonuniform leading to temperature gradients on the substrate surface.

At low rotation speeds (*e.g.*, 130 rpm) the fluid velocity near the edges are slow leading to lower heat transfer rates. Thus, we expect the deposition rate at the edges to be higher as seen in Figure 7.3(a). As the rotation speed is increased, temperature profile and consequently the deposition rate and the film thickness become more uniform as shown in Figures 7.3(b) and 7.3(c). For the film shown in Figure 7.3(c), the standard deviation of the film thickness at 17 different positions on the surface was ~6.3 nm or 7.5 % of the average film thickness (82.0 nm). Films deposited at higher temperatures are also uniform. For example, Figure 7.3(d) shows digital photograph and the radial variation of the film thickness for a CdS film deposited at 85 °C for 3 hours using a stirring speed of 725 rpm. For this film, the standard deviation of the film thickness at 17 different positions on the surface was ~8.0 nm or 7.4 % of the average film thickness (108.7 nm). At high deposition temperatures (*e.g.*, 85 ^{o}C), we noticed that the film thickness uniformity can be very sensitive to the substrate surface roughness and this issue has been discussed previously.[38]

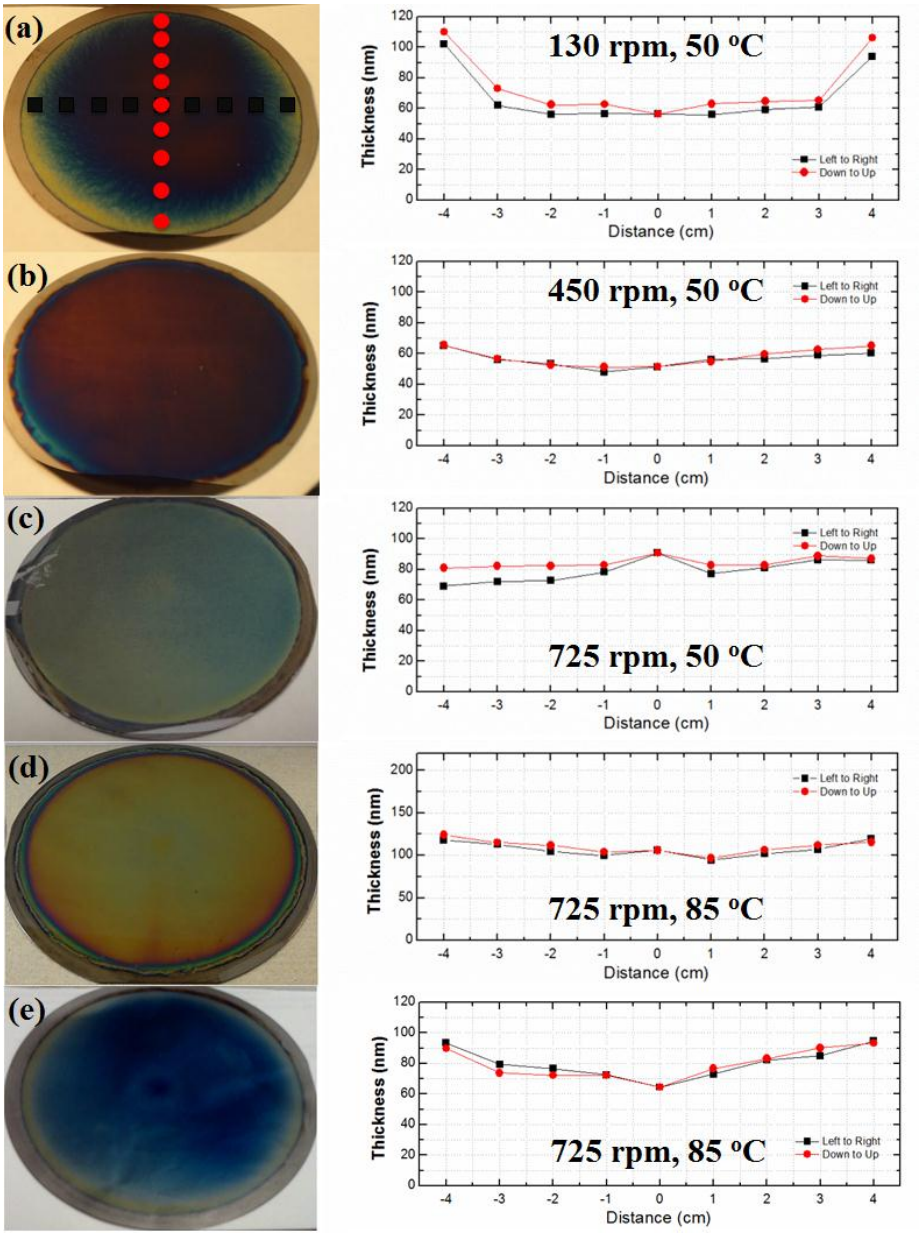

Figure 7.3. The spatial variation of the film thickness for CdS films deposited on Mo-coated Si substrates using CF-CBD at 50 °C with **(a)** 130 rpm, **(b)** 450 rpm, and **(c)** 725 rpm stirring rates. **(d)** CdS film, and **(e)** ZnS film deposited using CF-CBD at 85 °C and 725 rpm stirring rate. The deposited films have an average of **(a)** 70.5 nm thickness with 18.7 nm (26.6 %) standard deviation, **(b)** 57.1 nm thickness with 5.3 nm (9.2 %) standard deviation, **(c)** 82.0 nm thickness with 6.2 nm (7.5 %) standard deviation, **(d)** 108.7 nm thickness with 8.0 nm (7.4 %) standard deviation, and **(e)** 80.8 nm thickness with 9.4 nm (11.6 %) standard deviation.

Figure 7.3(e) shows the radial variation of the film thickness for a ZnS film grown in the CF-CBD system at 85 °C, 725 rpm for 3 hours. The average film thickness is 81

nm with 11.6 % (9.4 nm) standard deviation across the entire 100-mm-diameter. The ZnS films that are grown under identical conditions but using the traditional CBD approach yields thicker films (~250 nm).[37] Both, ZnS and CdS, deposition rates in the CF-CBD approach are a factor of 3 to 4 lower than those obtained in the traditional CBD method. This may be due to suppressed cluster-by-cluster deposition mechanism in CF-CBD process where the role of homogenous reactions are diminished due to lower solution temperature. $Zn_xCd_{1-x}S$ alloys grown with the CF-CBD system with and without EDTA also yield uniform film thickness across the entire substrate surface (Appendix I, Figure AI.1). The film thickness from $Zn_{0.88}Cd_{0.12}S$ alloy grown with the CF-CBD system without EDTA is confirmed by cross-sectional SEM (Figure AI.2).

7.3.2. Film Composition

The film composition and its variation as a function of film thickness is important because it determines the variation of conduction band and valence band edge energies as a function of film depth. Either uniform or graded film compositions may be desired depending on the application. For example, it may be desirable to have a CdS rich interface, for favorable band alignment with the absorber, followed by ZnS rich surface layers for reduced light absorption. Figure 7.4 compares the elemental Auger depth profiles for several $Zn_xCd_{1-x}S$ films deposited with and without EDTA in the solution. The film composition was varied by using different $CdSO_4$ and $ZnSO_4$ concentrations in the solution. The elemental Auger depth profiles of films grown without EDTA show nonuniform incorporation of Cd and Zn into the films. CdS and ZnS form at different rates and this difference results in films that are CdS-rich near the substrate-film interface and ZnS-rich near the film surface.[37] For example, Figure 7.4(c) shows that a $Zn_xCd_{1-x}S$ alloy is formed near the substrate surface but Cd concentration decreases rapidly as the film grows. In fact, the top 30 nm of this film is entirely ZnS and does not contain any Cd. In contrast, depositions with EDTA added to the solution results in relatively uniform incorporation of Zn and Cd across the entire film thickness. In Figure 7.4, the right (a, b, c) and the left (d, e, f) columns show the depth profiles for films deposited with and without EDTA, respectively, while each row shows depth profiles from films deposited

using the same initial precursor concentrations. For all the films grown without EDTA, the elemental Auger depth profiles show that Cd is incorporated near the film-Mo interface and Cd concentration decreases towards the film's surface. This is similar to the depth profiles that are typically seen in films deposited using the traditional CBD approach.[37] The principle reason for this decrease is the faster depletion of Cd^{2+} from the solution as compared to Zn^{2+}. While we do not observe significant homogenous nucleation of particles the Cd is still consumed because we observe deposition of films on the bath and tube walls. Chelating the ions with EDTA prevents homogeneous nucleation and stops deposition on reactor and tube walls. Chelating also slows the free-metal ion release into reacting solution and controls the films formation.[37] This helps to improve alloying of ZnS and CdS to form $Zn_xCd_{1-x}S$.[37] For example, Figures 7.4(d)-(f) show that the Cd and Zn composition depth profiles in films deposited with EDTA are much more uniform than the composition depth profiles in films deposited without EDTA (Figures 7.4(a)-(c)). Since Cd is not depleted through homogeneous nucleation and deposition on bath and tube walls its incorporation into the growing film is increased when EDTA is used. For example, the films in each row of Figure 7.4 were deposited with the same initial $ZnSO_4$ and $CdSO_4$ concentrations in the bath but, clearly, the films deposited with EDTA (7.4d-f) have more Cd than the films deposited without EDTA (7.4(a)-(c)).

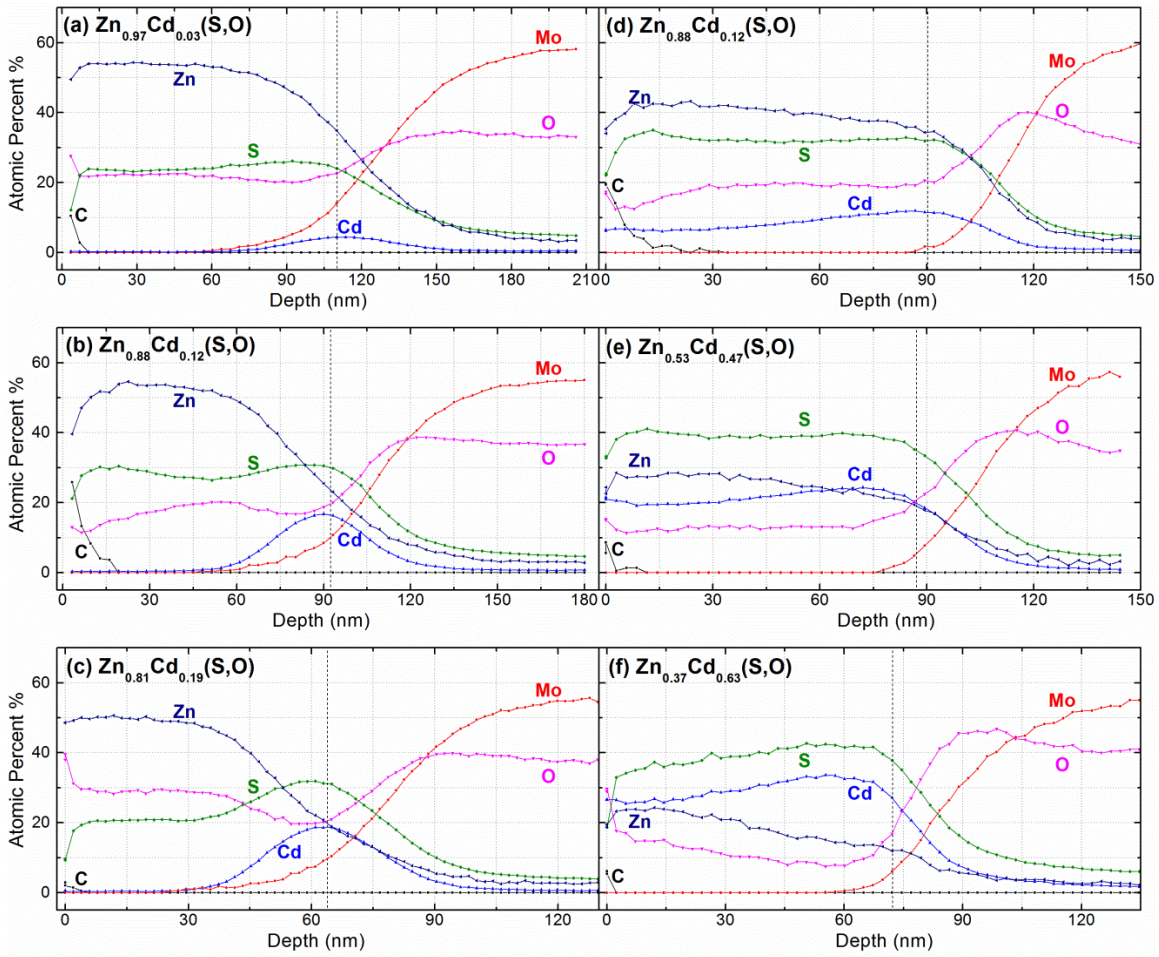

Figure 7.4. Auger depth profiles from CF-CBD grown $Zn_xCd_{1-x}S$ films deposited at 85 °C using **(a)** 49.5 mM $ZnSO_4$ and 0.05 mM $CdSO_4$, **(b)** 49.0 mM $ZnSO_4$ and 0.15 mM $CdSO_4$, **(c)** 48.5 mM $ZnSO_4$ and 0.20 mM $CdSO_4$ with no EDTA in the solution, and **(d)** 49.5 mM $ZnSO_4$ and 0.05 mM $CdSO_4$, **(e)** 49.0 mM $ZnSO_4$ and 0.15 mM $CdSO_4$, **(f)** 48.5 mM $ZnSO_4$ and 0.20 mM $CdSO_4$ with 15 mM EDTA in the solution.

All films also contain some oxygen and the amount of oxygen is higher for films with higher Zn content. The oxygen incorporation into CBD films is well known and is a result of the formation of $Zn(OH)_2$ which introduces the oxygen into the growing films.[34,128--132] This oxygen incorporation is also seen in CF-CBD. Thus, it is more appropriate to refer to these films as $Zn_xCd_{1-x}(S,O)$.

The spatial elemental compositions of $Zn_xCd_{1-x}(S,O)$ films are also uniform across the substrate diameter. The spatial variations in the elemental depth profiles from the $Zn_{0.53}Cd_{0.47}S$ and $Zn_{0.37}Cd_{0.63}S$ films, are compared in Supporting Information given

in Appendix I, Figures AI.3 and AI.4, respectively. Even though the films are slightly thicker at the edges, the elemental composition depth profiles exhibit the same trends regardless of the location on the substrate. The CF-CBD yields uniform film composition profiles across the radius of the substrate surface.

7.3.3. Film Structure

The XRD from $Zn_xCd_{1-x}S$ films deposited with and without EDTA are compared in Figure 7.5. In Figure 7.5, the right (a, b, c) and the left (d, e, f) columns show the XRD from films deposited with and without EDTA, respectively, while each row shows XRD from films deposited using the same initial precursor concentrations.

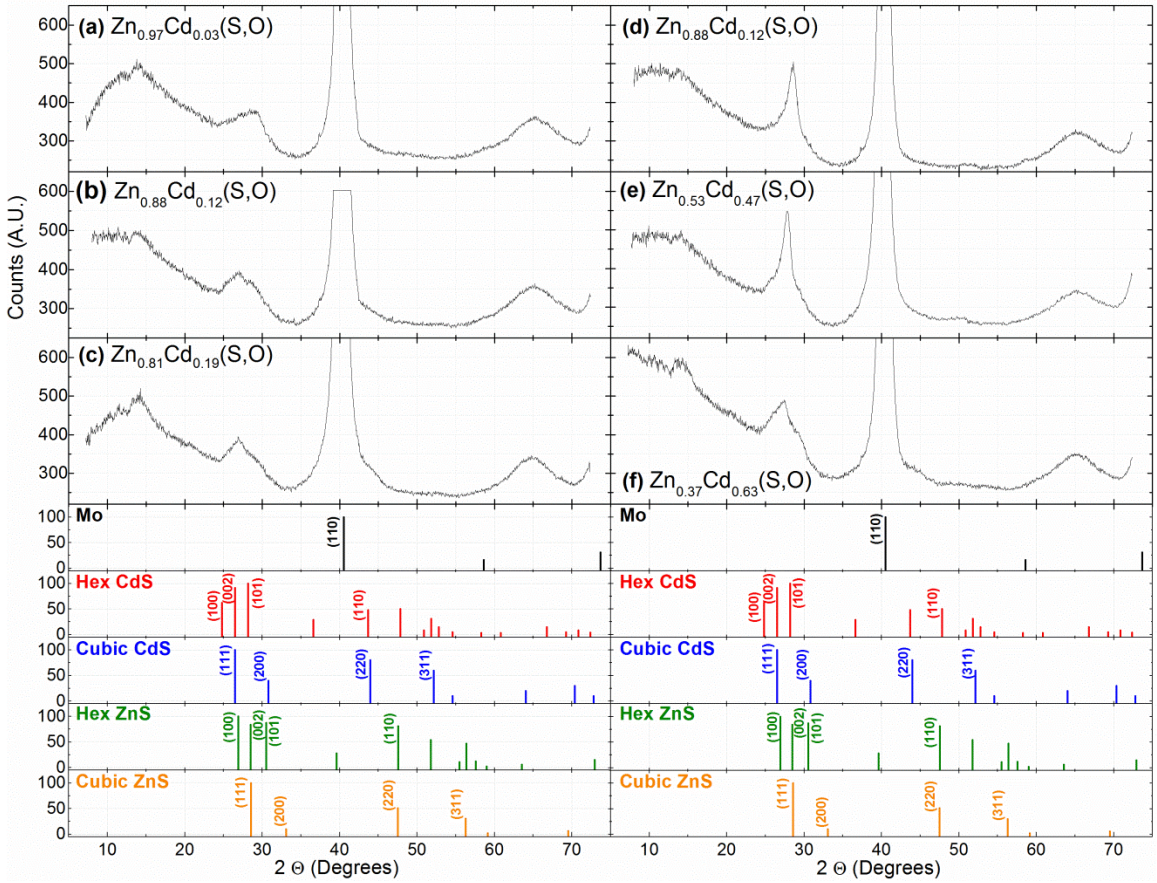

Figure 7.5. XRD from CF-CBD grown $Zn_xCd_{1-x}S$ films deposited at 85 °C using **(a)** 49.5 mM $ZnSO_4$ and 0.05 mM $CdSO_4$, **(b)** 49.0 mM $ZnSO_4$ and 0.15 mM $CdSO_4$, **(c)** 48.5 mM $ZnSO_4$ and 0.20 mM $CdSO_4$ with no EDTA in the solution, and **(d)** 49.5 mM $ZnSO_4$ and 0.05 mM $CdSO_4$, **(e)** 49.0 mM $ZnSO_4$ and 0.15 mM $CdSO_4$, **(f)** 48.5 mM $ZnSO_4$ and 0.20 mM $CdSO_4$ with 15 mM EDTA in the solution.

The XRD from the Zn-rich film (*e.g.*, Figure 7.5(a)) grown without EDTA is similar to the XRD from the $Zn_xCd_{1-x}S$ films deposited using the traditional CBD approach.[36] The broad diffraction peak at 29.2° is close that expected from cubic ZnS. The shift and broadening is likely due to both the small crystallite size and incorporation of O into the lattice. As Cd concentration in the film is increased (*e.g.*, Figures 7.5(a) and 7.5(b)) a second broad peak at lower 2θ grows in. The resulting shift to lower 2θ is consistent with increasing Cd concentration in the $Zn_xCd_{1-x}S$ alloy. A very thin layer of hexagonal Cd rich $Zn_xCd_{1-x}S$ alloy, as in Figure 7.5(b) and 7.5(c), would not be detectable in the XRD. In Figure 7.5(a), the absence of characteristic three close diffractions from (100) (002) and (101) planes in hexagonal CdS indicate that Cd is incorporated into the cubic ZnS lattice.[37] Combining the XRD with the Auger depth profiling, we conclude that these films are comprised of a likely cubic $Zn_xCd_{1-x}S$ alloy near the substrate and gradually become cubic ZnS near the film's surface. The precise location where they become entirely ZnS can be determined from the Auger depth profiles in Figures 7.4(a)-(c). The XRD peaks in Figures 7.5(a)-(c) are broad because of the gradients in the film composition and the resulting heterogeneity in the lattice parameter.

The XRD from films deposited with EDTA (Figures 7.5(d)-(f)) exhibit much narrower peaks as compared to the $Zn_xCd_{1-x}S$ grown without EDTA (Figures 7.5(a)-(c)). This difference in the peak widths is attributed to the differences in the uniformity of the elemental composition across the film thickness. For example, the relatively uniform film composition of the film shown in Figure 7.4(d) results in cubic structured films with very little variation in the lattice parameter. Consequently, the XRD in Figure 7.5(d) shows a very sharp peak at ~28.6°. Indeed, sharp XRD diffractions are obtained up to x=0.53. For example, the XRD for the cubic $Zn_{0.53}Cd_{0.47}$(S,O) film (Figure 7.5(e)), clearly shows a sharp peak at ~27.8°. The peak for the $Zn_{0.53}Cd_{0.47}$(S,O) film appears at a lower 2θ value than the peak for the $Zn_{0.88}Cd_{0.12}$(S,O) film because more Cd has been incorporated into the cubic ZnS lattice. However, a broad shoulder at ~26° is also discernible and indicates the possible presence of hexagonal structure somewhere in the film. Wright and Gale[134] predicted that $Zn_xCd_{1-x}S$ films with x>0.60 should have cubic structure, while films with

x<60 should have hexagonal structure.[134] Indeed, we have previously shown that $Zn_xCd_{1-x}S$ films deposited using the traditional CBD approach with x>0.60 have cubic crystal structure and that the structure switches to hexagonal when x<60.[134] Thus, it is surprising that the film with overall $Zn_{0.53}Cd_{0.47}(S,O)$ composition is still primarily cubic. However, close examination of the elemental composition profile shows that the top 60 nm of this film is Zn rich. In fact, the average composition of the top 60 nm is $Zn_{0.66}Cd_{0.34}(S,O)$ while the average film composition is $Zn_{0.53}Cd_{0.47}(S,O)$. Thus, x is greater than 0.6 for nearly two-thirds of the film and a significant fraction of the film remains cubic. On the other hand, the Zn composition decreases as the interface with the Mo is approached. The film composition at near the interface with the Mo is $Zn_{0.50}Cd_{0.50}(S,O)$ and we surmise that this portion of the film is hexagonal leading to the shoulder at ~26°. In Figure 7.5(f), the Cd content is so large that the entire film is likely a hexagonal alloy. The diffraction peaks from three close diffractions from (100), (002), and (101) planes are broadened and overlap due to the decreasing lattice parameters with decreasing Cd^{2+} composition from substrate interface to film surface.

The variation of the $Zn_{0.88}Cd_{0.12}(S,O)$ film's structure along its depth was investigated using HRTEM and SAED. This is the film in Figures 7.4(b) and 7.5(b) and it was deposited without EDTA in the CF-CBD solution. A cross-sectional sample of this film was prepared for TEM examination using the tripod polishing technique. Figure 7.6 shows the HRTEM images and respective SAED from this film. The electron diffraction was recorded from three selected regions defined by a ~250 nm diameter aperture (Figure 7.6(a)). Diffractions and images were recorded from the first 15 nm of the film near the Mo interface (Figure 7.6(b)), the entire film (Figure 7.6(c)), and the top 50 nm of the film's surface (Figure 7.6(d)). The SAED patterns in Figures 7.6(e), (f) and (g) correspond to the areas shown in Figures 7.6(b), (c) and (d), respectively. The plot in Figure 7.6(h) was generated by integrating the electron diffraction patterns in Figures 7.6(e), (f) and (g) over 2π radians. In Figure 7.6(h), the diffraction from the lower 15 nm of the film near the interface shows a peak position at 2.94 nm^{-1}. This corresponds to 3.40 Å, averaged from the possible overlapping hexagonal (100), (002), and (101) plane *d*-spacings of the Cd-rich alloy. The entire film has a higher Zn content than the first 15

nm. This reflects on SAED with peak shifts to higher locations on average of 2.99 nm^{-1} which corresponds to *d*~3.34 Å. The SAED from 50 nm near the surface has a peak at 3.06 nm^{-1}, an average of *d*~3.26 Å, from the (111) planes of cubic $Zn_xCd_{1-x}(S,O)$. This decrease in the *d*-spacing agrees well with the decreasing Cd composition in the Auger depth profile shown in Figure 7.5(b). The unit cell lattice parameters decreases from the Cd-rich alloy at the Mo interface towards Zn(S,O) film at the surface. The film composition at the interface is calculated from Auger depth profiles to be $Zn_{0.55}Cd_{0.45}(S,O)$. Since this composition is $x<0.60$ at the Mo interface, the film structure is surmised to be hexagonal at the Mo interface. Thus, the broader ring pattern in Figure 7.6(e) is likely from the three close diffractions (100), (002), and (101) of hexagonal structure.

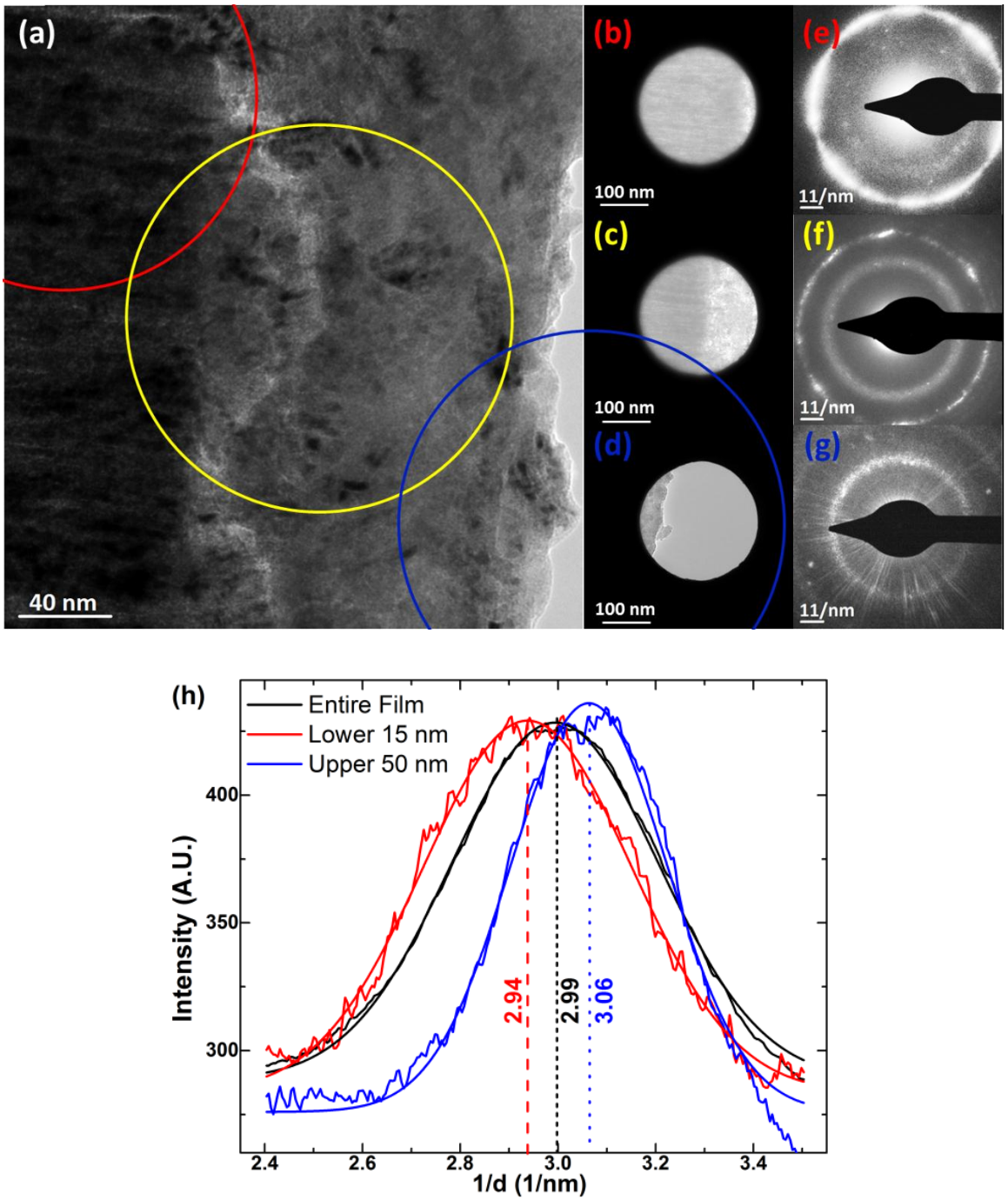

Figure 7.6. (a) HRTEM image of $Zn_{0.88}Cd_{0.12}(S,O)$ film deposited using 49 mM $ZnSO_4$ and 0.15 mM $CdSO_4$ and without EDTA. **(b)** Selected area image from the first 15 nm of this film near the Mo interface where averaged x≈0.55. **(c)** Selected area image from the entire film where the average x≈0.88. **(d)** Selected area image from the top 50 nm of the film's surface where the averaged x≈1. Selected area electron diffractions from **(e)** the first 15 nm of this film near the Mo interface, **(f)** the entire film, and **(g)** the top 50 nm of the film's surface. **(h)** Angle integrated electron diffraction from the selected areas.

7.4. Conclusions

We have demonstrated a continuous flow chemical bath deposition approach that provides efficient utilization of chemicals. The key idea is to heat the substrate while limiting the heating of the liquid solution containing the precursors. This approach can eliminate the formation of particles in the liquid phase via homogenous reactions. CdS, ZnS, and $Zn_xCd_{1-x}S$ films were deposited on 100-mm-diameter substrates uniformly with and without EDTA in the solution. $Zn_xCd_{1-x}(S,O)$ films deposited without EDTA showed Cd incorporation primarily at the substrate-film interface. On the other hand, $Zn_xCd_{1-x}(S,O)$ films deposited with EDTA showed relatively more uniform composition profiles across the film thickness. $Zn_xCd_{1-x}(S,O)$ alloys were cubic when $x>0.60$, and hexagonal when $x<0.60$, though a mixture of the two structures can also result when the overall composition is close to this boundary.

CHAPTER 8

Cu_2ZnSnS_4 Nanocrystal Dispersions in Polar Solvents

Cu_2ZnSnS_4 (CZTS) nanocrystals sterically stabilized with oleic acid and oleylamine ligands and dispersed in nonpolar organic solvents have been extracted into, and electrostatically stabilized in, polar solvents by covering their surfaces with S^{2-}.

8.1. Introduction

Rapid development of thin-film copper zinc tin sulfide (Cu_2ZnSnS_4 or CZTS) and selenide ($Cu_2ZnSnSe_4$ or CZTSe) solar cells with power conversion efficiencies in the 7-10% range attests to the remarkable potential of this material as a light absorber comprised of earth-abundant and nontoxic elements.[40,41,141] Thin CZTS films can be synthesized in many different ways including coevaporation from elemental sources in vacuum[142,143] or high-temperature sulfidation of metal precursors deposited on substrates by evaporation or sputtering.[144-146] While most methods rely on traditional vacuum thin-

film deposition, coating from colloidal nanocrystal dispersions (inks) have also received attention because they have the potential to be less expensive than vacuum processing.[147,148] Recently, several approaches for synthesizing CZTS nanocrystal dispersions have been reported[149-152] and solar cells made from these dispersions have achieved efficiencies exceeding 7%.[136] However, all methods produce nanocrystal dispersions in organic nonpolar solvents where the nanocrystals are sterically stabilized by long alkyl ligands adsorbed on their surfaces. Deposition of thin films by coating and drying from nanocrystal dispersions necessitates the handling of large volumes of organic solvents such as toluene, undermining the presumed cost advantage of making solar cells from nanocrystal inks. Aqueous dispersions of CZTS are prefered.[153] Herein, we describe a method for extracting CZTS nanocrystals from organic non-polar solvents into polar solvents and ultimately forming aqueous dispersions.

8.2. Experimental Details

CZTS nanocrystals used in this work were synthesized from copper, zinc and tin dithiocarbamate complexes in presence of oleic acid and oleylamine as described by Khare *et al.*[152] The as-synthesized CZTS nanocrystals are stabilized in organic nonpolar solvents such as toluene by oleic acid and oleylamine adsorbed on their surfaces. To make nanocrystals dispersions in polar solvents, these long alkyl-chains must be at least partially removed and replaced. Inspired by recent reports of replacing organic ligands on III-V and II-VI nanocrystals (CdSe, InP, ZnSe, etc.) with inorganic ions,[154] we extracted the nanocrystals from toluene into formamide, containing K_2S in at room temperature and eventually dispersed them in water.

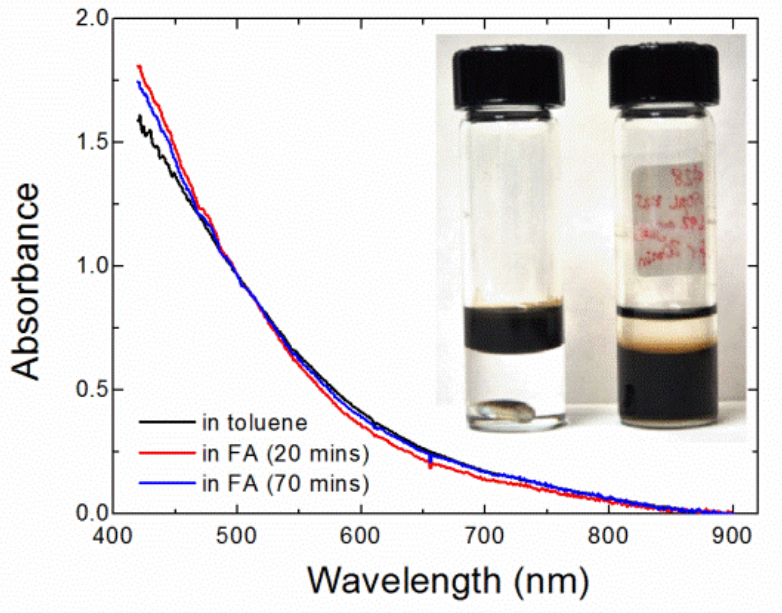

Figure 8.1. Optical absorption spectra of ~5 nm diameter CZTS nanocrystal dispersions in toluene before extraction and in formamide (FA) after extraction. The 20 and 70 minutes refer to the duration of the extraction. The inset shows the as-synthesized CZTS nanocrystals in toluene before extraction (left) and in formamide after extraction (right).

In a typical extraction, CZTS nanocrystals dispersed in toluene are added to a mixture of formamide and K_2S solution in deionized (DI) water and the resulting two-phase mixture is stirred vigorously for a period ranging from 20 minutes to 16 hours. The detailed experimental procedures are given in the Appendix II, Supplementary Information.[†] The extent of extraction can be monitored through the color changes in the nonpolar toluene and polar formamide phases (Figure 8.1 inset). Initially, CZTS containing toluene phase appears black and the formamide phase is clear and colorless. The formamide phase turns orange with the addition of K_2S. As S^{2-} adsorb on the CZTS surface, the nanocrystals are electrostatically stabilised and extracted to the formamide phase. While the formamide phase begins to get darker after stirring for 20 minutes, a thick emulsion still remains visible between the polar formamide and nonpolar toluene phases. Stirring longer gradually thins the emulsion and the formamide phase gets darker. We surmise that the nanocrystals covered with both alkly ligands and S^{2-} act as a surfactant and stabilize the emulsion at the toluene-formamide interface. When the nanocrystals are mostly covered with S^{2-} they are transferred to the formamide phase and

the emulsion breaks up. Following stirring, the toluene phase is removed from the top and the nanocrystals are separated from formamide by adding acetonitrile and centrifuging the resulting mixture to precipitate them out of dispersion. The nanocrystals are cleaned by washing with formamide and redispersed in fresh formamide by vortexing and sonicating. Typically, washing and redispersion in formamide is repeated several times (3 to 6). Repeating the cleaning step removes excess K_2S but also decreases the stability of the dispersion. When washed once, the S^{2-} capped particles are stable for more than a week in formamide but only a few days if the washing step is repeated several times. The dispersion stability depends on the K_2S concentration in the solvent and can also be improved by addition of K_2S to the final formamide dispersion. For making aqueous dispersions, water is added to the CZTS nanocrystals after the last cleaning step.

8.3. Results and Discussion

The CZTS nanocrystals were characterized using optical absorption spectroscopy, x-ray diffraction (XRD), high-resolution transmission electron microscopy (HRTEM), Raman spectroscopy and attenuated total reflection Fourier transform infrared (ATR-FTIR) spectroscopy before and after extraction into formamide. (See Appendix II[†]).

The extraction of CZTS nanocrystals into formamide does not change their structure, size and optical properties. Figure 8.1 compares the optical absorption of CZTS nanocrystals when they are dispersed in toluene and, after extraction, when they are dispersed in formamide. The optical absorption begins to rise at ~850 nm corresponding to the band gap of bulk CZTS (1.45 eV). The average diameter of these particles were too large (~5 nm) to show quantum confinement.[152]

Figure 8.2 shows the XRD from CZTS nanocrystals that were drop cast and dried on a silicon substrate from toluene, formamide and aqueous dispersions. All three diffraction patterns match with the expected CZTS powder diffraction pattern (JCPDS 26-0575). The average crystallite size extracted from the width of the (112) diffraction peak (28.5°) using Debye-Scherer analysis was 5 nm for all CZTS nanocrystals

regardless of the liquid they were dispersed in. This average size agreed well with the nanocrystal diameters measured from HRTEM images (Figure 8.3), which showed nanocrystal with diameters between 4 and 6 nm in ensembles cast from both toluene and formamide. Raman spectra of nanocrystal films cast from dispersions in toluene and formamide were identical and showed a single scattering peak centered at 338 cm^{-1} consistent with CZTS (Figure 8.4).

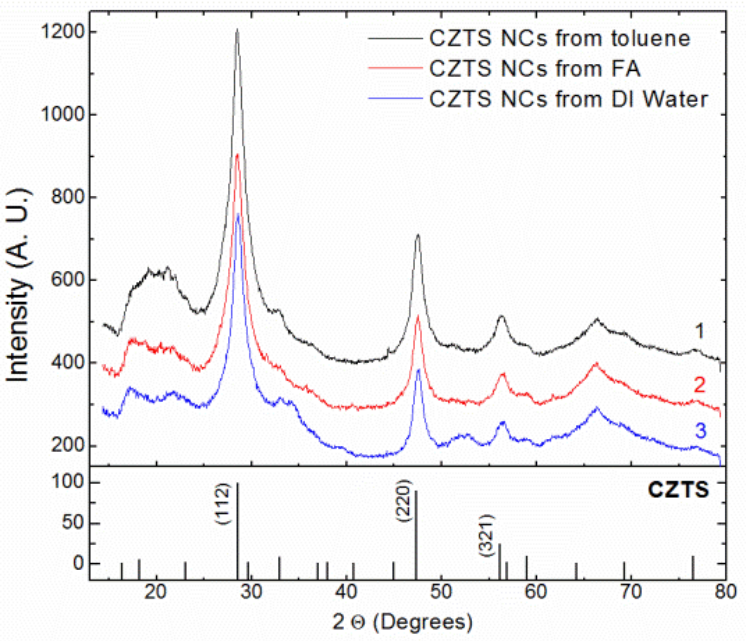

Figure 8.2. XRD from CZTS nanocrystals (NCs) drop cast and dried on silicon (100) substrates from toluene, formamide (FA) and water.

Extraction into an intermediate phase such as formamide and washing the excess K_2S is necessary for succesfully preparing aqueous dispersions of CZTS nanocrystals. We observed significant changes in the CZTS nanocrystals when high concentrations of K_2S was present in aqueous dispersions. Specificaly, combination of CZTS nanocrystals, exces K_2S and water leads to the formation of zinc hydroxystannate ($ZnSn(OH)_6$). The aqueous solution becomes basic upon hyrolysis of K_2S in water via $K_2S + H_2O \leftrightarrow KOH + KSH$ and $ZnSn(OH)_6$ forms, likely through the reactions of OH^- ions with CZTS. For example, Figure 8.6 shows the XRD from a CZTS nanocrystal film cast from an aqueous dispersion with excess K_2S.

Specifically, the CZTS nanocrystals were cleaned only once after extraction before dispersing them in DI water. Sharp (200) and (220) diffractions from $ZnSn(OH)_6$ clearly indicate the presence of this reaction product.

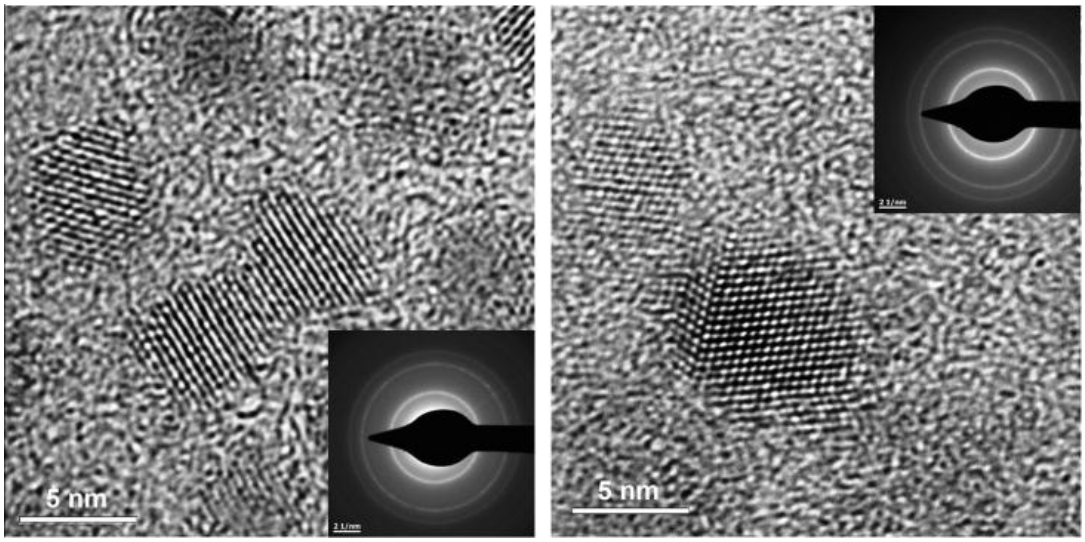

Figure 8.3. HRTEM images of as synthesized CZTS nanocrystals drop cast onto TEM grids from toluene (left) and S^{2-} capped CZTS nanocrystals drop cast onto TEM grids from formamide (right). The insets are diffraction patterns recorded from samples.

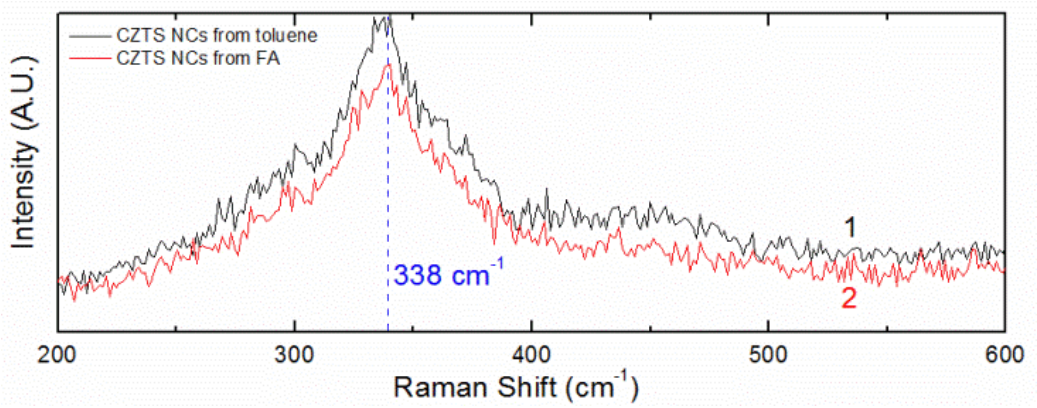

Figure 8.4. Raman spectra of (1) as synthesized CZTS nanocrystals drop cast from toluene and (2) S^{2-} capped CZTS nanocrystals drop cast from formamide (FA).

Clearly, the bulk of the CZTS nanocrystals remain unaltered during the extraction but their surfaces must be different to change their interactions with polar and nonpolar liquids. To investigate these changes on the nanocrystal surface we employed ATR-FTIR. Figure 8.5 shows the ATR-FTIR spectra of nanocrystal films

cast onto a Ge ATR crystal from toluene and from water, before and after extraction, respectively. The as-synthesized nanocrystals in toluene exhibit IR absorption at 2852 cm^{-1} and 2925 cm^{-1} corresponding to the vibrations of C-H bonds in oleylamine and oleic acid adsorbed onto the nanocrystal surfaces. Figure 8.5 shows that, surprisingly, even the nanocrystals extracted into polar liquids have residual oleylamine and oleic acid on their surfaces and not all organic ligands are removed during extraction. Despite these remaining organic ligands, the CZTS nanocrystals are extracted into and dispersed in formamide and water. We could rationalize this surprising result only after quantifying the absolute coverage of the organic ligands on the CZTS nanocrystal surface. (See Appendix II for details†). Quantification of the ligand coverage on the CZTS nanocrystals revealed that the magnitude of the C-H stretching absorbance corresponds to ~9×10^{13} ligand molecules/cm^2. This is only ~13% of the available sulfur (or metal) sites (~6.8×10^{14} cm^{-2}) on the {001} surfaces of the CZTS nanocrystals. Approximately 50-60% of these ligands are removed during extraction so that the ligand coverage decreases to ~3.5×10^{13} ligand molecules/cm^2 or about ~5% of the available sites. Thus, we conclude that the extraction into the polar liquid is achieved by covering the remaining surface sites with S^{2-} ions in formamide and the small amount of remaining alkyl ligands are inconsequential to their dispersion in polar solvents. Likely, the residual alkyl ligands left on the surface take on more compact configurations when the nanocrystals are in water or formamide and do not extend into the polar solvent. Moreover, dynamic light scattering (DLS) experiments show some degree of agglomeration with an average agglomerate size of ~93 nm in the formamide phase and ~220 nm in the toluene phase (See Appendix II†). Thus, the ligands remaining on the surfaces may be those that are trapped wihin these small agglomerates.

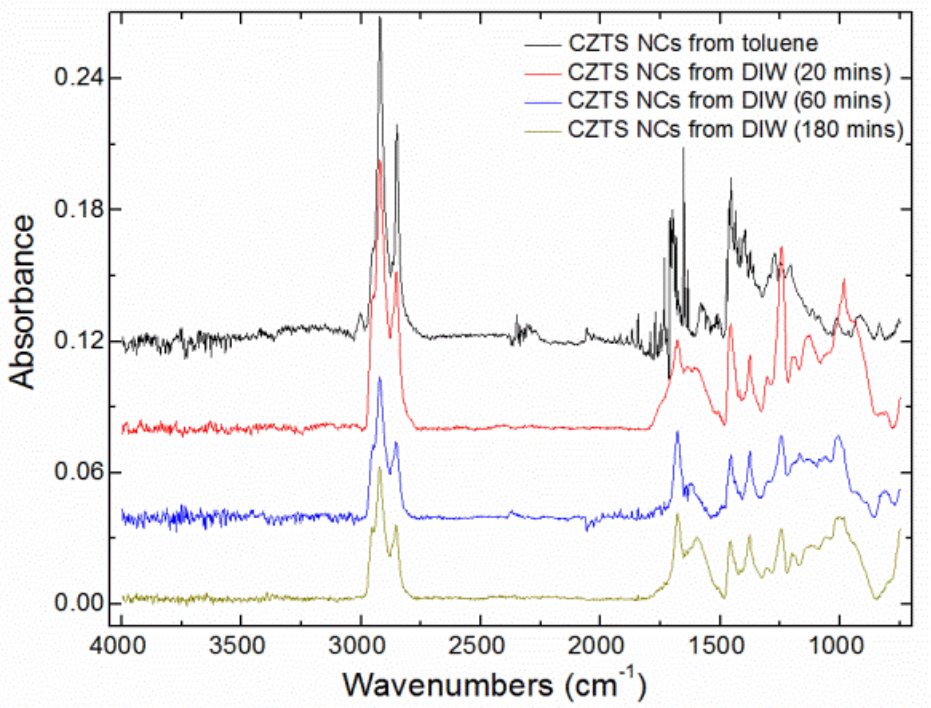

Figure 8.5. ATR-FTIR spectra of the CZTS nanocrystals drop cast from toluene, before extraction, and drop cast from DI water, after extraction. Spectra for different extraction times are shown. The blue, red and black spectra baselines were shifted for clarity.

In water, K_2S hydrolyzes rapidly to KOH and KSH so that the capping ligands are expected to be HS^- rather than S^{2-}. Indeed, the infrared spectra, between 800-1700 cm^{-1}, of the nanocrystals drop cast and dried on ATR crystals from water and formamide is consistent with this picture and exhibit infrared absorptions that can be assigned to vibrations of SO_4 in K_2SO_4 and in $KHSO_4$,[155] which are expected to form when K_2S oxidizes in air in presence of moisture.

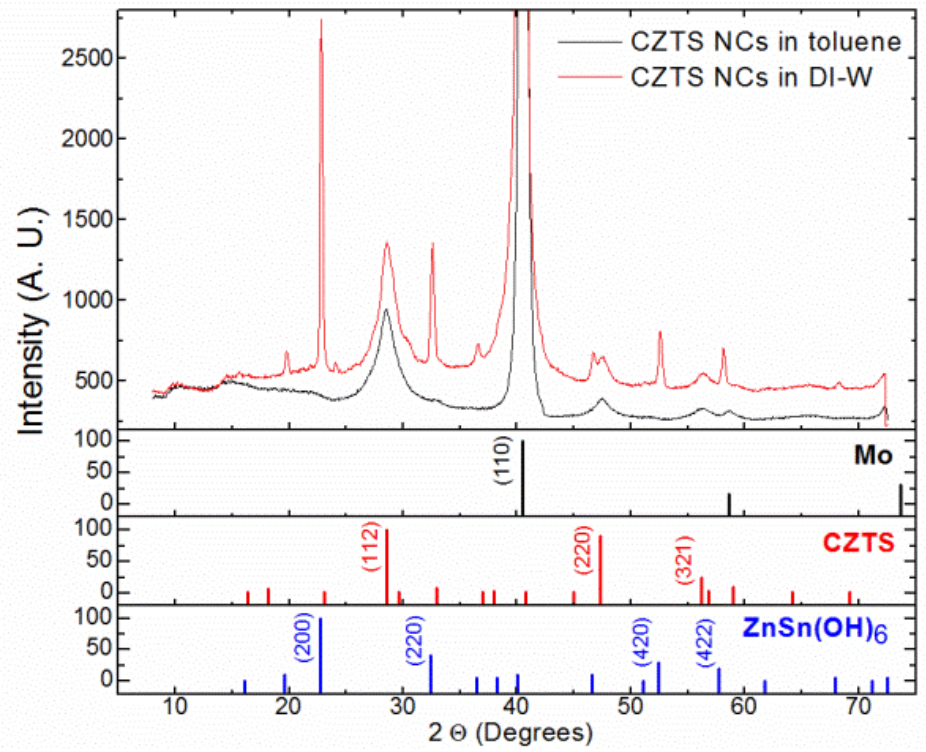

Figure 8.6. XRD from CZTS nanocrystals drop cast and dried from toluene and from aqueous dispersions after extraction. The CZTS NCs were cleaned only once after extraction before dispersing them in DI water. The bottom panels show reference powder XRD patterns for Kesterite CZTS (JCPDS 26-0575) and cubic $ZnSn(OH)_6$ (JCPDS 20-1455). The particles were drop cast on Mo coated Si (100) substrates.

8.4. Conclusions

In summary, we report a method for dispersing CZTS nanocrystals in polar solvents such as formamide and water. These dispersions are achieved by extracting oleylamine and oleic acid capped CZTS nanocrystals dispersed in toluene into a K_2S solution in formamide. The nanocrystals are electrostatically stabilized with inorganic S^{2-} in formamide and HS^- in water. Examination of the nanocrystals by optical absorption, TEM, XRD and Raman spectroscopy show that the extraction process does not change the nanoparticle size and the structure, provided that care is taken not to expose the crystal to high concentrations of K_2S in water.

CHAPTER 9

The Effect of SnS Vapor on Cu_2ZnSnS_4 Thin Film Microstructure from Water-Based Nanocrystal Inks

We deposited Cu_2ZnSnS_4 (CZTS) thin films from water based nanocrystal inks on molybdenum coated soda-lime glass substrates by drop casting. These, the drop cast CZTS nanocrystal films were annealed at 600 °C in sealed quartz ampoules. High temperature annealing leads to decomposition of CZTS by sulfur (S) and tin monosulfide (SnS) evaporation but this can be eliminated by controlling the annealing ambient. In this chapter, we investigate the effect of $SnS_{(g)}$ and $S_{(g)}$ vapor pressure on the microstructure evolution of films during annealing. Annealed films are studied by x-ray diffraction (XRD), Scanning electron microscopy (SEM), and Raman spectroscopy. Two grain growth mechanisms are observed, normal grain growth and abnormal grain growth. SnS vapor pressure (~10 mTorr) in the presence of S vapor drastically enhances the abnormal grain growth, and leads to 1-4 μm grains.

9.1. Introduction

Cooper zinc tin sulfide (Cu_2ZnSnS_4, CZTS) has garnered significant interest during the last five years as a low-cost photovoltaic material because it has the potential to achieve similar solar energy conversion efficiencies as the high efficiency (>20.3 %) thin film $Cu(In,Ga)Se_2$ (CIGS) solar cells and it is comprised of abundant elements.[156,157] Many vacuum and liquid solution based methods have been developed for depositing CZTS.[3,120,136,145,151,157-159] Vacuum based deposition methods such as co-sputtering followed by sulfidation and co-evaporation have been used because these methods yield high efficiency CIGS based solar cells.[147,148] Solution based methods are emerging as an alternative and are purported to reduce the fabrication cost without sacrificing the efficiency. Infact, the highest efficiency (10.1 %) CZTS solar cells are synthesized through reactions of organometalic complexes dissolved in hydrazine.[141] CZTSSe solar cells made by annealing nanocrystal coatings deposited from colloidal nanocrystal dispersions in organic solvents (inks) have reached over 7.2% conversion efficiencies. This method of making CZTSSe films by annealing colloidal nanocrystal coatings may have high-throughput manufacturing potential. The nanocrystals used for this purpose are capped with long alkyl ligands, and dispersed in organic solvents. Preparing these nanocrystal inks in less expensive and environmentally benign solvents, such as water without alkyl ligands, can further reduce the solar cell manufacturing cost and improve the film purity efficiencies by reducing the carbon content of the absorber film.[47,153]

Microstructure of thin CZTS films strongly affect the performance of solar cells.[160] Large grains are desired to minimize surface recombination at the grain boundaries, and to improve carrier collection. For this reason, CZTS nanocrystal films deposited from colloidal dispersions of 5-30 nm CZTS nanocrystals require post-deposition annealing, to obtain large grained films. Ideally grain sizes on the order of the film thickness is desired such that photo-generated carriers encounter as few grain boundaries as possible before they reach to junction at the top and the bottom of the film.

CZTS decomposes to SnS which has high vapor pressure and leaves the CZTS especially when the temperature of the film is above 500 °C.[163-168] Specifically, CZTS decomposes into $Cu_2SnS_{3(s)}$ first and later to $Cu_2S_{(s)}$, $ZnS_{(s)}$, $S_{(g)}$, and $SnS_{(g)}$ through a series of reactions. The decomposition is summarized in reaction 9.1. The decomposition into binaries have adverse effects on the device performance.[163-170] Fortunately, this decomposition of CZTS can be eliminated by annealing under high enough S and SnS vapor pressures.[164,168]

$$Cu_2ZnSnS_4(s) \leftrightarrow Cu_2S_{(s)} + ZnS_{(s)} + SnS_{(g)} + S_{(g)} \quad (9.1)$$

Herein, we studied the annealing and microstructure evolution of CZTS nanocrystal thin films deposited from colloidal dispersions of CZTS nanocrystals in water[163] on molybdenum (Mo) coated SLG substrates under different S and SnS vapor pressures. The microstructures of the films were examined before and after annealing using scanning electron microscopy (SEM, Joel 6500 and 6700 Field-Emission). Their stoichiometry was determined using energy-dispersive x-ray spectroscopy (EDS). The phase compositions of the annealed films were studied using x-ray diffraction and Raman spectroscopy.

9.2. Experimental Details

The CZTS nanocrystals (~20 nm) were synthesized from Zn-, Sn- and Cu-diethyldithiocarbamates as described by Chernomordik et al.[171] The as synthesized nanocrystals are capped with oleate ligands and dispersed in toluene. The particles were extracted into formamide (FA) as described in Chapter 8 by covering their surfaces with S^{2-} from a K_2S solution. After the extraction, the excess K_2S was cleaned with FA ~6 times. Following, CZTS nanocrystals were dispersed in deionized water (DI-W) by vortexing and sonicating. Approximately 3 μm thick films were deposited on Mo-coated SLG substrates by drop casting. Mo film was 1 μm thick, and deposited by DC magnetron sputtering. The films crack if the drying is fast. Thus, the crack formation was minimized by slowing the drying process. Films were casted in ~300 nm thickness each

time to yield a ~3 μm thick nanocrystal film, and each casting is dried for 2 hours. The excess K_2S crystals are rinsed from every ~1 μm film layer dried overnight by DI water before the addition of other layers. EDS analysis from the rinsed CZTS nanocrystal films showed ~0.1-0.01 % (at.) K, which is in the instrumental limits.

The films were annealed at 600 °C in sealed quartz ampoules. The drop-casted CZTS nanocrystal films were loaded into 1 cm diameter quartz tubes with various amounts of S and Sn pellets and evacuated to 10^{-6} Torr, or lower pressure using a turbo molecular pump. After 10^{-6} Torr is reached, the quartz tube was sealed by fusing to obtain a 10 cm long sealed ampoule. The sealed ampoules were loaded into a preheated ceramic block with cylindrical slots from the ampoule in a preheated oven (both 600 °C) as 1 cm of the ampoule will stick out from the ceramic block. During cooling this 1 cm region cools first and vapors condense there instead of on the thin film. The ampoules were kept in the oven for a predetermined time period (e.g., 1 hour, 2 hours, 4 hours, and 8 hours), and naturally cooled to room temperature by turning off the heater. The samples were removed from the ampoules by breaking them.

The average crystal sizes after annealing were calculated by using a line method with averaging over ~15 grains in the high magnification top-view micrographs. In the presence of Na diffusing from SLG substrate, Cu and Zn L_α peaks (0.93 eV and 1.02 eV) interferes with Na K_α peak (1.04 eV). Thus, 15 keV accelerating voltage is used to identify the Cu and Zn K_α peaks at 8.03 eV and 8.64 eV, respectively. The structure of the films were investigated using x-ray diffraction (XRD, Bruker-AXS) with Cu-K_α radiation (λ=0.154056 nm). However, CZTS is not distinguishable from decomposition products Cu_2SnS and ZnS by x-ray diffraction, because they have the same S sublattice with nearly the same unit cell dimensions. Raman scattering from these phases are different than each other. Raman peaks appears at 289 cm^{-1}, 338 cm^{-1}, 350 cm^{-1}, and 370 cm^{-1} for CZTS, at 267 cm^{-1}, 303 cm^{-1} and 356 cm^{-1} for Cu_2SnS_3, and at 278 cm^{-1} and 352 cm^{-1} for ZnS.[146,172] Room temperature Raman scattering spectra, excited with a 514.5 nm Argon ion laser (~300 nm beam size), was collected using a confocal Raman microscope

(WiTec alpha300R) in conjunction with a UHTS300 spectrometer and a DV401 CCD detector.

9.3. Results and Discussion

Figure 9.1 shows the effect of annealing with 1 mg of S loacked into the ampoule. At 600 ºC, all solid S is vaporized and the pressure in the tube is ~35 Torr. In Figure 9.1, the first column (a, b, c), the second column (d, e, f), the third column (g, h, i), and the forth column (j, k, l) show the drop-casted films before annealing, after 2 hours, after 4 hours, and after 8 hours annealing, respectively. The first row (a, d, g, j), and the second row (b, e, h, k) show the low- and the high-magnification top-view SEM micrographs, while the third row (c, f, i, l) shows the cross-sectional SEM micrographs, respectively.

The first observation is that the crystal size grows from ~20 nm to 190 nm ± 15 nm by the end of 2 hours, to 192 nm ± 70 nm by the end of 4 hours, and to 203 nm ± 48 nm by the end of 8 hours. The neck formation between grains indicates sintering and increase in grain size must have taken place via solid state diffusion since zinc and copper sulfides are not volatile even though SnS has high vapor pressure. Moreover, the grain growth and sintering results in denser films, and the film thickness decreases from ~3 μm to ~2 μm as seen in the cross sectional micrographs in Figure 9.1(c) and 9.1(l), respectively. Occasionally, larger grains (~1 μm) are observed on films annealed for 4 and 8 hours (Figures 9.1(h) and 9.1(k)). The increase in crystal size is also observed in the corresponding x-ray diffractions (Figure 9.2). The CZTS (112) diffraction peak is sharper after 2 hours of annealing indicating that the crystal size is grown. By 2 hours, the peak width has reached the instrumental broadening limit which is ~ 50 nm. Raman scattering peaks at 338 cm^{-1} confirm the presence of CZTS phase before and after annealing for 2 hours, 4 hours, and 8 hours, respectively (Figure 9.3).

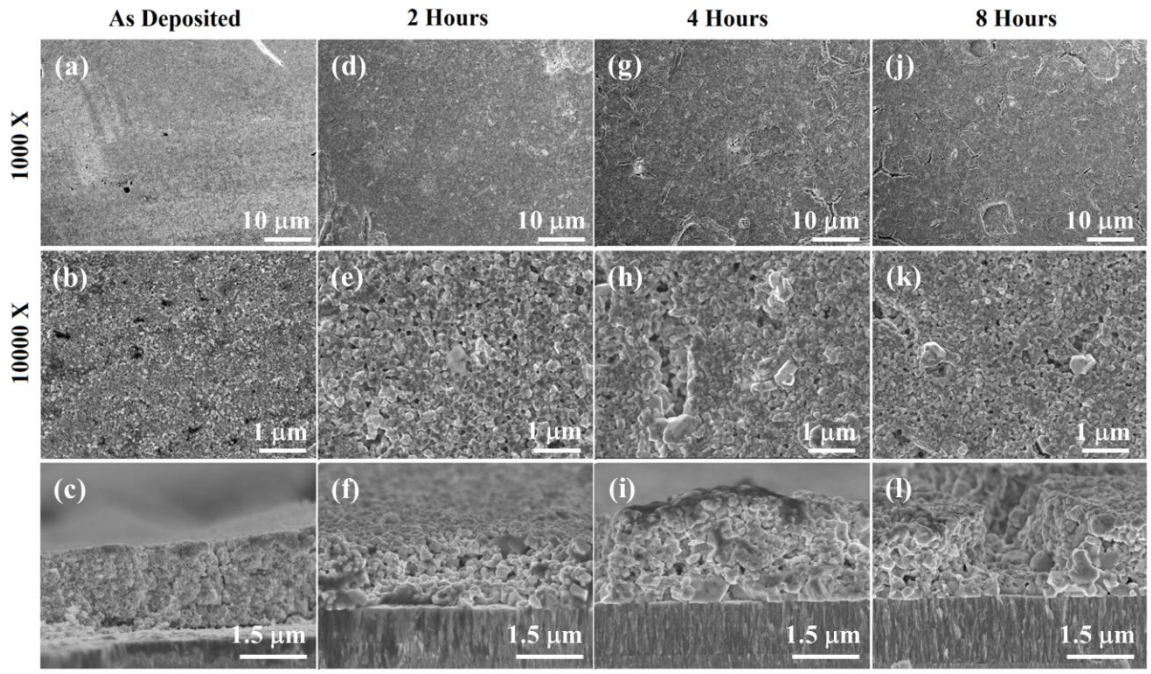

Figure 9.1. SEM micrographs of CZTS nanocrystal films **(a, b, c)** before annealing, and after annealing **(d, e, f)** for 2 hours, **(g, h, i)** for 4 hours, and **(j, k, l)** for 8 hours under 1 mg S vapor (~35 Torr). The rows **(a, d, g, j)** are the low-, and **(b, e, h, k)** are the high-magnification top-view SEM micrographs, and **(c, f, i, l)** are the cross-sectional SEM micrographs.

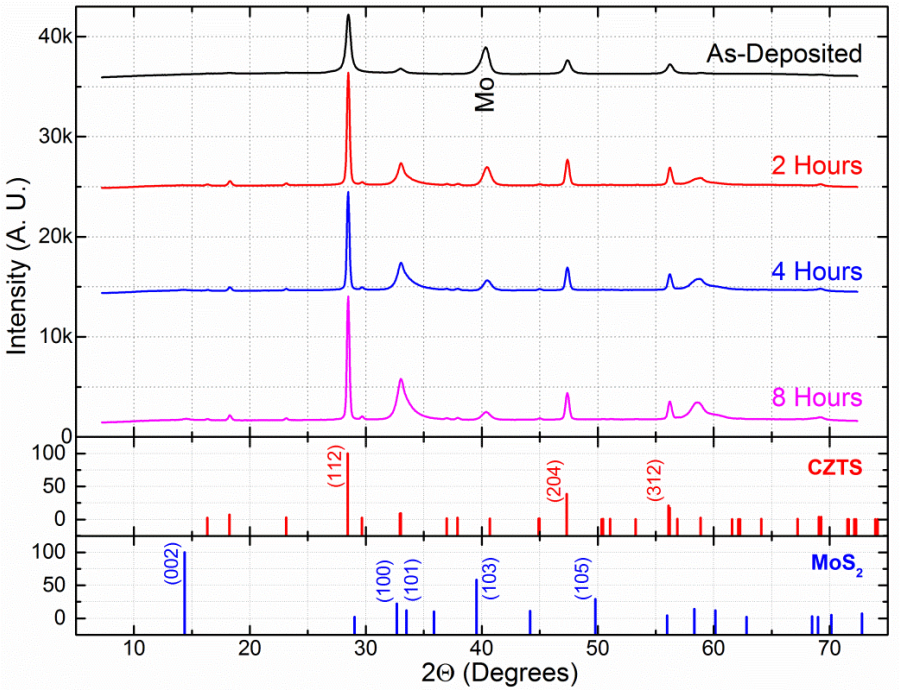

Figure 9.2. X-ray diffraction patterns from as deposited nanocrystal film, and after annealing for 2 hours, 4 hours, and 8 hours under 1 mg S vapor.

The second observation is that the Mo coating on the SLG substrate reacts with sulfur vapor and forms MoS_2 film at the interface with the CZTS film. The unit cell of MoS_2 (PDF#00-037-1492) is 4 times larger than that for Mo's (PDF#00-042-1120), which results in an expansion of the underlying Mo film as MoS_2 film grows thicker with increasing annealing time. For example, MoS_2 thickness reaches to ~1 μm by 2 hours (Figure 9.1(f)), and increases to ~2 μm by 8 hours (Figure 9.1(l)) with approximately 50 % sulfidation of the initial ~1 μm thick Mo. The x-ray diffraction intensity from (100) and (101) planes of MoS_2 increases with annealing time (Figure 9.2). Raman scattering peaks at 383 cm^{-1} and 407 cm^{-1} are also consistent with the MoS_2 film.[173,174]

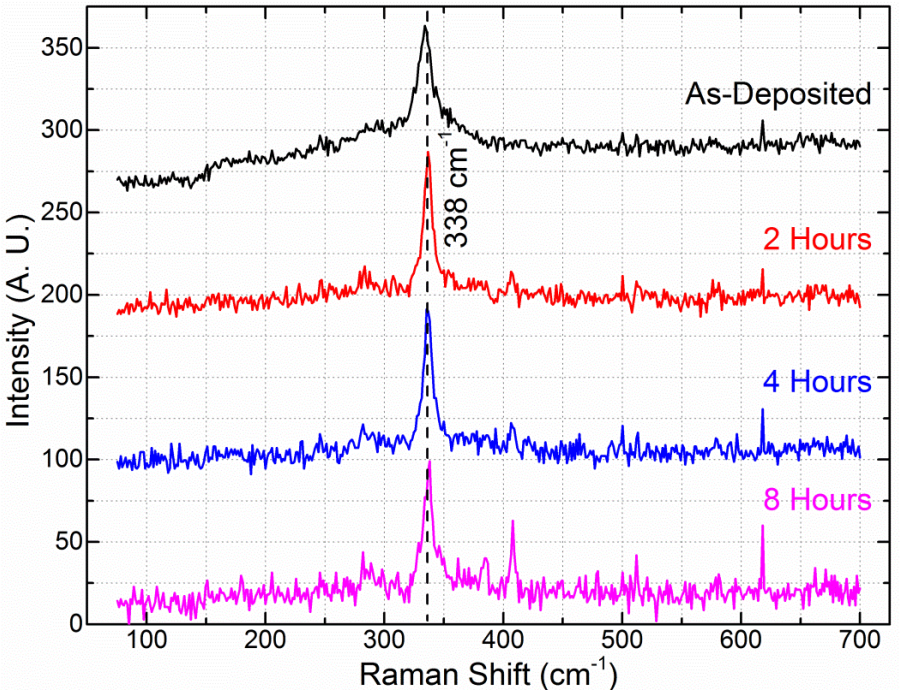

Figure 9.3. Raman spectra of the as deposited nanocrystal films, and after annealing for 2 hours, 4 hours, and 8 hours under 1 mg S vapor.

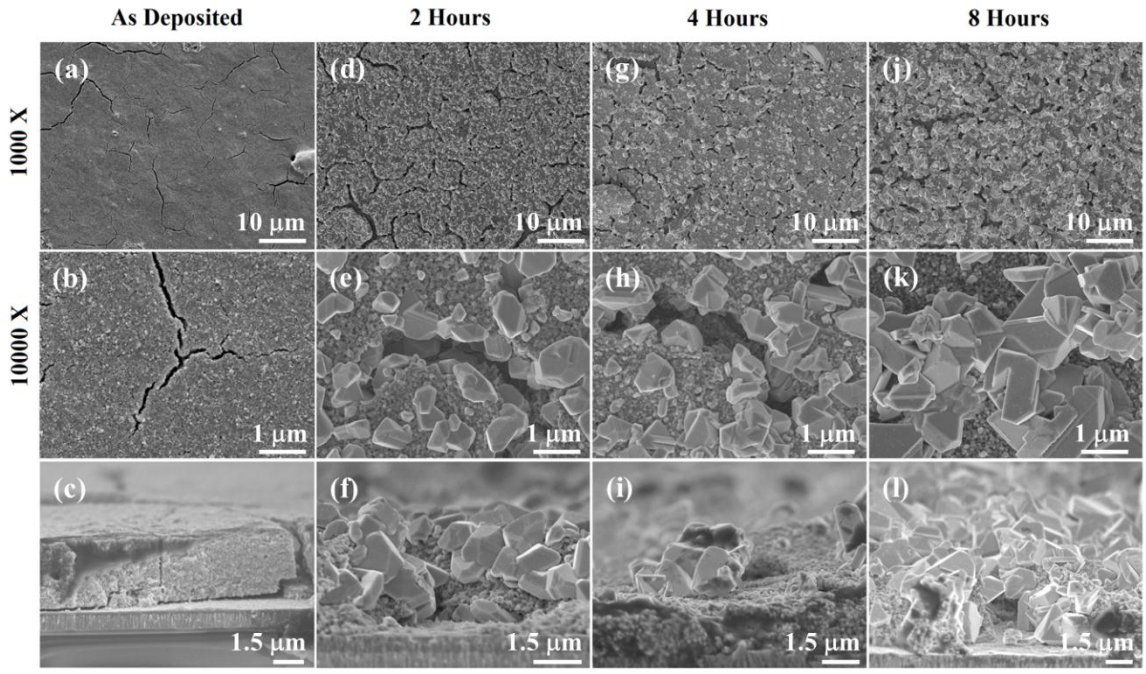

Figure 9.4. SEM micrographs of CZTS nanocrystal films **(a, b, c)** before annealing, and after annealing **(d, e, f)** for 2 hours, **(g, h, i)** for 4 hours, and **(j, k, l)** for 8 hours under 1 mg S and 1 mg Sn vapor. The rows **(a, d, g, j)** are the low magnification, and **(b, e, h, k)** are the high magnification top-view SEM micrographs, and **(c, f, i, l)** are the cross-sectional SEM micrographs.

Figure 9.4 shows the SEM of CZTS nanocrystal films annealed at 600 ºC with 1 mg of S and 1 mg of Sn in the ampoule. At 600 °C, S vapor reacts with Sn and forms $SnS_{2(s)}$.[175] Above ~25 °C and certainly at 600 ºC, $SnS_{2(s)}$ decomposes by a series of reactions, ($SnS_2 \leftrightarrow Sn_2S_3 \leftrightarrow Sn_4S_5 \leftrightarrow SnS$; release or addition of S and Sn_yS_x is assumed to balance the reactions, but not shown in here), and releases S and SnS vapors.[163,164,168,175,176] The reaction of 1 mg S (~31 μmol) and 1 mg Sn (~8.4 μmol) results in ~16 Torr S vapor and ~10 mTorr saturated SnS vapor pressures at 600 °C in the ampoule.[176]Annealing CZTS nanocrystal films under ~10 mTorr SnS and ~16 Torr S drastically changes the microstructure of the annealed films. Specifically, we observe a bomodal crystal size distribution characteristic of abnormal grain growth.[175] The SEMs of films annealed for 2 hours show 1.63 μm ± 0.73 μm size grains (Figure 9.4(d-f)). After 4 hours, the grains grow larger to 2.46 μm ± 0.37 μm. By 8 hours, the grain size reaches to 3.87 μm ± 0.77 μm. The average crystal size of the normal crystals are 155 nm ± 31 nm,

167 nm ± 35 nm, and 178 nm ± 77 nm by the end of 2, 4, and 8 hours, respectively. During this growth the nanocrystals are consumed. The stoichiometry of film compositions is confirmed to be ~$Cu_{1.95\pm0.10}ZnSnS_{3.85\pm0.25}$ by EDS for all films and does not change during annealing within the detection limits of EDS. The x-ray diffraction patterns, shown in Figure 9.5, are consistent with CZTS. The 2D XRD from ~4.0 μm size crystals is spotty as shown in Figure 9.6. The Raman scattering peak at 338 cm^{-1} confirms the CZTS phase for all films. Thus, we concluded that CZTS grains grow by ripening without decomposition.

Under ~16 Torr S and ~10 mTorr SnS, thinner MoS_2 is observed. The MoS_2 (100) XRD intensity increases with the annealing time. SEM shows that the thickness of MoS_2 film is ~0.2 μm by 2 hours, and less than 0.4 μm by the end of 8 hours. This is substantially thinner than the MoS_2 films formed during annealing with S vapor (~35 Torr) alone. This is partially attributed to lower S vapor (~16 Torr) because some S is consumed by Sn to form SnS_2 and SnS. The MoS_2 is also detected by Raman scattering at 407 cm^{-1} (Figure 9.7).[173,174] However, recently, different facets of the large CZTS crystals has also showed Raman peaks at 407 cm^{-1}.[171]

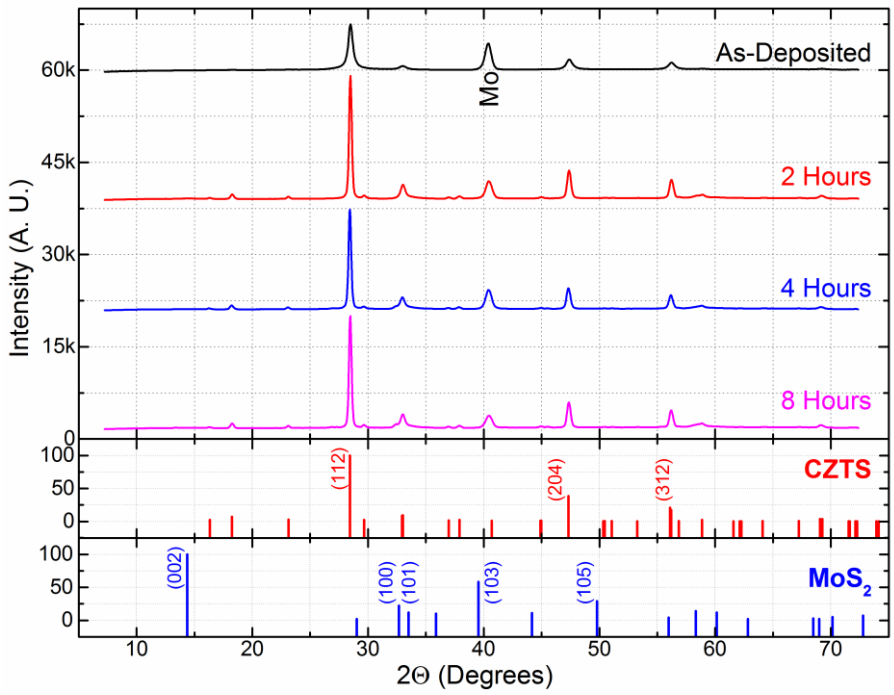

Figure 9.5. X-ray diffraction patterns from as deposited nanocrystal film, and after annealing for 2 hours, 4 hours, and 8 hours under 1 mg S and 1 mg Sn vapor.

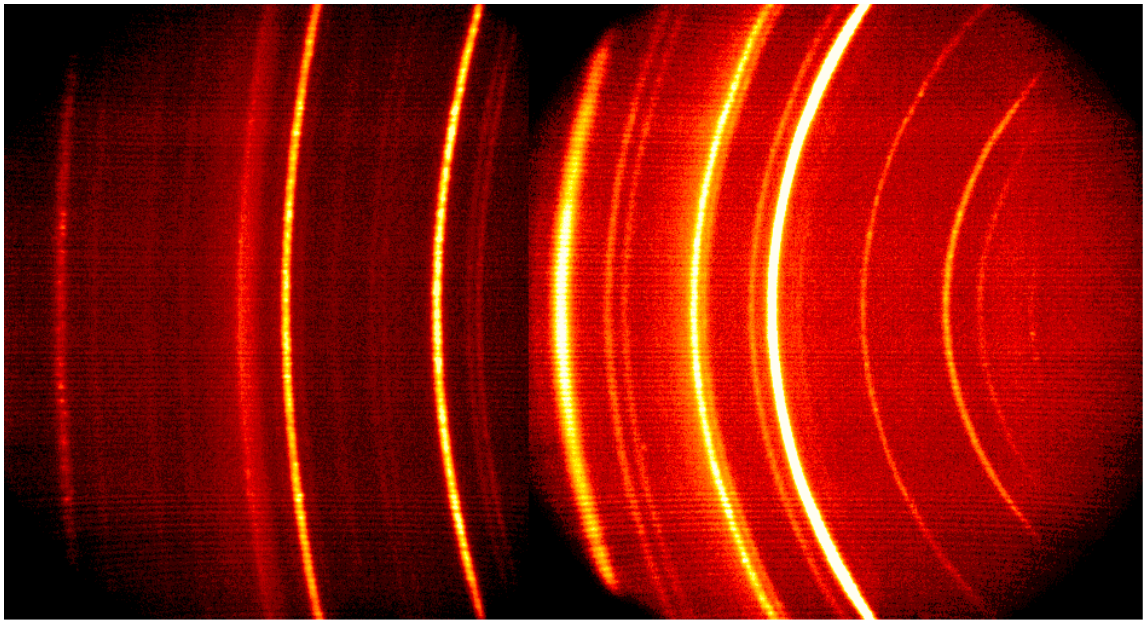

Figure 9.6. 2D X-ray diffraction patterns from 7-73º 2Θ (degrees) of CZTS nanocrystal film after annealing for 8 hours under 1 mg S and 1 mg Sn vapor.

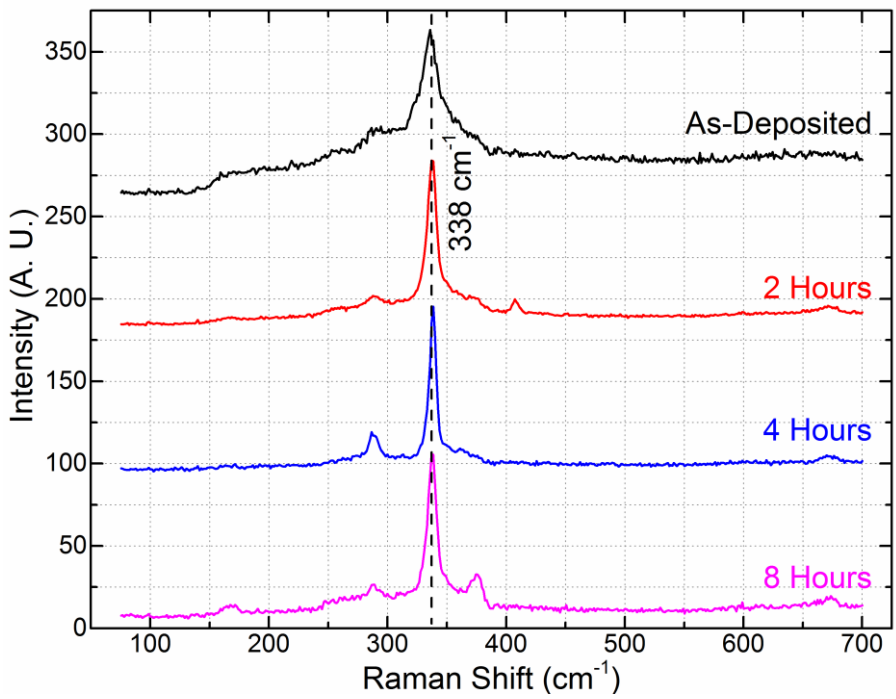

Figure 9.7. Raman spectra of the as deposited nanocrystal films, and after annealing for 2 hours, 4 hours, and 8 hours under 1 mg S and 1 mg Sn vapor.

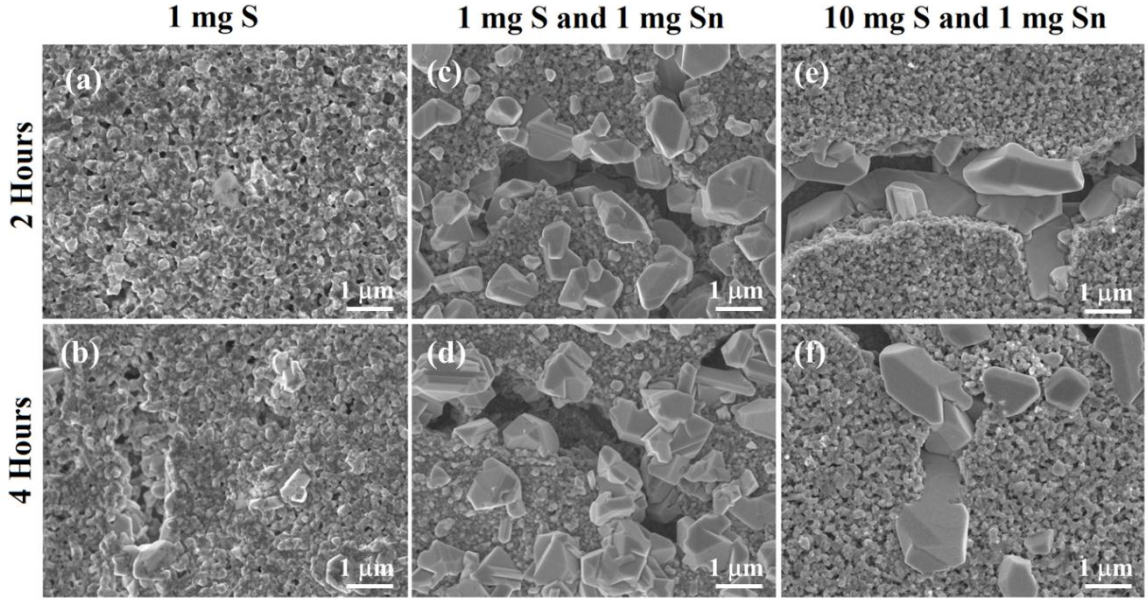

Figure 9.8. SEM comparison of CZTS nanocrystal films after annealing for 2 hours and 4 hours **(a, b)** under 1 mg S vapor, **(c, d)** under 1 mg S and 1 mg Sn vapor, and **(e, f)** under 10 mg S and 1 mg Sn vapor, respectively.

The microstructure evolution of CZTS nanocrystal films during annealing appears to involve two mechanisms, normal grain growth and abnormal grain growth, which are operative under different annealing conditions. The comparison of the SEMs, shown in Figures 9.1 and 9.4, suggests that microstructure evolves through sintering and the normal grain growth when only S is present in the annealing tube. On the other hand, abnormal grain growth is observed when SnS is present.

Figure 9.8 shows the films annealed using 10 mg S in the annealing tube (P_S~331 Torr) and 1 mg Sn (P_{SnS}~10 mTorr) show both normal grain growth (188 nm ± 43 nm after 4 hours) and the abnormal grain growth (3.77 μm ± 0.92 μm after 4 hours). Annealing with ~10 mTorr SnS vapor and ~331 Torr S vapor results in abnormal grain growth by 2 hours, the abnormal grain sizes have reached to 3.42 μm ± 0.85 μm compared to 1.63 μm ± 0.72 μm for films annealed at ~10 mTorr SnS and ~16 Torr S. However, the average size of larger grains grows very slowly from 2 hours to 4 hours (3.77 μm ± 0.92 μm). In addition, the normal grain size is calculated to be 154 nm ± 49 nm by the end of 2 hours, and this increases to 188 nm ± 43 nm by 4 hours. We surmise that ~190 nm grain size is the critical size for Ostwald ripening mechanism, grains above this diameter do not dissolve to be re-deposited onto larger crystals. Hence, the abnormal grain growth slows, and becomes diffusion limited due to enhanced normal grain growth under higher S pressure.

9.4. Conclusions

We deposited CZTS thin films from water dispersed nanocrystal inks on Mo coated SLG glass. We studied the evolution of grain growth as a function of time by annealing at 600 °C in a sealed quartz ampoule under different S and SnS vapor pressures. We observed two growth mechanism, normal grain growth and abnormal grain growth, which appear to be competing with each other. The normal grain growth is observed to be operative when annealing in S only (P_S~ 35 Torr). On the other hand, abnormal grain growth is observed to be operative when SnS vapor is present (P_{SnS} ~10

mTorr) in the presence of P_S ~16 Torr. The competition between abnormal grain growth and normal grain growth is seen in 10 mg S and 1 mg Sn annealing results. The abnormal grain size reaches to >3.5 μm by 2 hours and drastically slows after the normal grains reach to critical size ~190 nm for Ostwald ripening.

REFERENCES

1 U.S. Energy Information Administration (EIA), International Energy Outlook (2011).

2 U.S. Energy Information Administration (EIA), Annual Energy Outlook (2011).

3 Wadia, C, Alivisatos, A.P. Kammen, D.M., *Environ. Sci. Technol*. **43**, 2072-2077 (2009).

4 Norris, D.J., Aydil, E.S., *Science* **338**, 625-626 (2012).

5 Earth Policy Institude, World Solar Photovoltaics Production, 1975-2010 (2011), www.earth-policy.org/datacenter/xls/inidicator12_2011_1.xls.

6 International Energy Agency, Electricity Information 2012 (2012), www.oecd-ilibrary.org/energy/electricity-information-2012_electrocity-2012-en.

7 Birkmire, R.W., Eser, E., *Annu. Rev. Mater. Sci.* **27**, 625 (1997).

8 NBC News, http://www.minbcnews.com/news/story.aspx?id=510364#.UY8Xc5WihpY, May (2013).

9 Kemell, M., Ritala, M., Leskela, M., *Crit. Rev. Solid State* **30:1**, 1-31 (2005).

10 Li, J.B., Chawla, V., and Clemens, B.M., *Adv. Mater.* **24**, 720 (2012).

11 Singh, U.P., Patra, S.P., *International Journal of Photoenergy* **2010**, 468147 (2010).

12 DuPont Photovoltaic Solutions, http://www2.dupont.com/Photovoltaics/en_US/news_events/article20110825.html?src=pvsecvideo_WK-solar, May 2013.

13 http://www.smg-indium.com/Docs/IndiumPriceCharts.pdf, May 2013.

14 Wennerberg, J., Kessler, J., Stolt, L., *Sol. Energy Mater. Sol. Cells* **75,** 47-55 (2003).

15 Spiering, S., Hariskos, D., Schonder, S., Powalla, M., *Thin Solid Films* **480-481**, 195-198 (2005).

16 Powalla, M., Dimmler, B., *Thin Solid Films* **387**, 251-256 (2001).

17 Igalson, M., Wimbor, M., Wennerber, J., *Thin Solid Films* **403-404**, 320-324 (2002).

18 Deibel, C., Dyakonov, V., Parisi, J., Palm, J., Zweigart, S., Karg, F., *Thin Solid Films* **403-404**, 325-330 (2002).

19 Carcia, P.F., McLean R.S., Hegedus, S., *Sol. Energy Mater. Sol. Cells* **94**, 2375-2378 (2010).

20 Tosun, B.S., Feist, R., Gunawan, A., Mkhoyan, K.A., Campbell, S.A. Aydil, E.S., *Thin Solid Films* **520**, 2554-2561 (2012).

21 Tosun, B.S., Feist, R., Gunawan, A., Mkhoyan, K.A., Campbell, S.A. and Aydil, E.S., *Sol. Energy Mater. Sol. Cells* **101**, 270-276 (2012).

22 Tosun, B.S., Feist, R., Campbell, S.A. and Aydil, E.S., *J. Vac. Sci. Technol. A*, **30(4),** 04D101 (2012).

23 Burton, L.C., Hench, T.L., *Appl. Phys. Lett.* **29**, 612 (1976).

24 Yamaguchi, T., Yamamoto, Y., Tanaka, T., Yoshida, A., *Thin Solid Films* **343**, 516 (1999).

25 Nakada, T., Furumi, K., Kunioka, A., *IEEE Trans. Electron. Dev* **46**, 2093 (1999).

26 Nakada, T., Mizutani, M., *Jpn. J. Appl. Phys.* **2**, 41, L165 (2002).

27 Nakada, T., Hongo, M., Hayashi, E., *Thin Solid Films* **431**, 242 (2003).

28 Sartale, S. D., Sankapal, B. R., Lux-Steiner, M., Ennaoui, A., *Thin Solid Films* **480**, 168 (2005).

29 Bhattacharya, R. N., Contreras, M. A., Teeter, G., *Jpn. J. Appl. Phys.* **2**, 43 L1475 (2004).

30 Ennaoui, A., Bar, M., Klaer, J., Kropp, T., Saez-Araoz, R., Lux-Steiner, M. C., *Prog. Photovoltaics* **14**, 499 (2006).

31 Bhattacharya, R.N., Ramanathan, K., *Sol. Energy* **77**, 679 (2004).

32 Kundu, S., Olsen, L.C., *Thin Solid Films* **471**, 298 (2005).

33 Yagioka, T., Nakada, T., *Appl. Phys. Express* **2**, 072201 (2009).

34 Dona, J.M., Herrero, J., *Thin Solid Films* **268**, 5 (1995).

35 Pudov, A., Sites, J., Nakada, T., *Jpn. J. Appl. Phys.* **2**, 41, L672 (2002).

36 Bhattacharya, R.N., Contreras, M.A., Egaas, B., Noufi, R.N., Kanevce, A., Sites, J.R., *Appl. Phys. Lett*, **89**, 253503 (2006).

37 Tosun, B.S., Pettit, C., Campbell, S.A. and Aydil, E.S., *ACS Appl. Mater. Interfaces* **4**, 3676-3684 (2012).

38 Tosun, B.S., Abrahamson, J.T., Cheng, C., Campbell, S.A. and Aydil, E.S., *39th PVSC Proceedings* - accepted June 17th-21st (2013).

39 Tosun, B.S., Abrahamson, J.T., Cheng, C., Campbell, S.A. and Aydil, E.S., *Prog. Photovoltaic Res. Appl.* - submitted (2013).

40 Mitzi, D.B., Gunawan, O., Todorov, T.K., Wang, K., and Guha, S., *Sol. Energy Mater. Sol. Cells* **95**, 1421 (2011).

41 Katagiri, H., *Thin Solid Films*, **480-481**, 426 (2005).

42 Shockley, W., Queisser, H.J., *J. Appl. Phys.* **32**, 510 (1961).

43 Wadia, C., Alivisatos, A.P., Kammen, D.M., *Environ. Sci. Technol.* **43**, 2072-2077 (2009).

44 Repins, I., Contreras, M.A., Egaas, B., DeHart, C., Scharf, J., Perkins, C.L., To, B., Noufi, R., *Prog. Photovoltaics* **16,** 235 (2008).

45 Platzer-Björkman, C., Scragg, J., Flammersberger, H., Kubart, T., Edoff, M. *Sol. Energ. Mater. Sol. C.* **98,** 110–117 (2012).

46 Panthani, M.G., Akhavan, V., Goodfellow, B., Schmidtke, J.P., Dunn, L., Dodabalapur, A., Barbara, P.F., and Korgel, B.A., *J. Am. Chem. Soc.* **130**, 16770 (2008).

47 Tosun, B.S., Chernomordik, B.D., Gunawan, A.A., Williams, B., Mkhoyan, K.A., Francis, L.F., and Aydil, E.S., *Chem. Comm.* **49**, 3549 (2013).

48 Tosun, B.S., and Aydil, E.S., *Nanotechnology* – in preparation (2013).

49 Gubbins, M.A., Casey, V., Newcomb, S.B., *Thin Solid Films* **405,** 270 (2002).

50 Martel, A., Caballero-Briones, F., Bartolo-Perez, P., Iribarren, A., Castro-Rodrigues, R., Zapata-Navarro, A., Pena, J.L., *Surf. Coat.Technol.* **148,** 103 (2001).

51 Kim, T.W., *Mater. Res. Bull* **36,** 349 (2001).

52 Kim, T.W., D.U. Lee, D.U., Jung, M., Lee, J.H. , Choo, D.C., Cho, J.W., Seo, K.Y., Yoon, Y.S., *Appl. Surf. Sci.* **182,** 69 (2001).

53 Chang, W.C., Lee, S., Qi, X., *J. Electrochem. Soc.* **157,** J245 (2010).

54 Jager, S., Szyszka, B., Szczyrbowski, J., Brauer, G., *Surf. Coat.Technol.* **98,** 1304 (1998).

55 Lee, S.U., Hong, B., Choi, W.S., *J. Vac. Sci. Technol. A* **27,** 996 (2009).

56 Montero, J. , Herrero, J., Guillen, C., *Sol. Energy Mater. Sol. Cells* **94,** 612 (2010).

57 Senthilkumar, V., Vickraman, P., Prince, J.J., Jayachandran, M., Sanjeeviraja, C., *Phil. Mag. Lett.* **90,** 337 (2010).

58 Korber, C., Agoston, P., Klein, A., *Sensor Actuat. B-Chem.* **139,** 665 (2009).

59 Diana, T., Devi, K.N., Sarma, H.N., *Indian J. Phys.* **84,** 687 (2010).

60 T.P. Niesen, T.P., De Guire, M.R., *Solid State Ionics* **151,** 61 (2002).

61 Ansari, S.G., Dar, M.A., Dhage, M.S., Kim, Y.S., Ansari, Z.A., Al-Hajry, A. , Shin, H., *Rev. Sci. Intrum.* **80,** 0451121 (2009).

62 Serin, T., Serin, N., Karadeniz, S., Sari, H., Tugluoglu, N., Pakma, O., *J. Non-Cryst. Solids* **352,** 209 (2006).

63 Pan, X.Q., Fu, L., *J. Appl. Phys.* **89,** 6048 (2001).

64 Alaf, M., Guler, M.O., Gultekin, D., Uysal, M., Alp, A., Akbulut, H., *Vacuum* **83,** 292 (2009).

65 Pan, S.S., Li, G.H., Wang, L.B., Shen, Y.D., Wang, Y., Mei, T., Hu, X., *Appl. Phys. Lett.* **95,** 222112 (2009).

66 Korber, C., Suffner, J., Klein, A., *J. Phys. D: Appl. Phys.* **43,** 055301 (2010).

67 Ma, H.L., Hao, X.T., Ma, J., Yang, Y.G., Huang, J., Zhang, D.H., Xu, X.G., *Appl. Surf. Sci.* **191,** 313 (2002).

68 Behr, M.J., Mkhoyan, K.A., Aydil, E.S., *ACS Nano* **4,** 5087 (2010).

69 Drake, C., Seal, S., *Appl. Phys. Lett.* **90,** 233117 (2007).

70 Manifacier, J.C., De Murcia, M. , Pillard, J.P., *Thin Solid Films* **41,** 127 (1977).

71 Bruneaux, J., Cachet, H., Froment, M., Messad, A., *Thin Solid Films* **197,** 129 (1991).

72 Shirakata, S., Yokoyama, A., Isomura, S., *Jpn. J. Appl. Phys.* **2 (35),** L722 (1996).

73 Korotkov, R.Y., Farran, A.J.E., Culp, T., Russo, D., Roger, C., *J. Appl. Phys.* **96,** 6445 (2004).

74 Oprea, A., Moretton, E., Barsan, N., Becker, W.J., Wollenstein, J., Weimar, U., *J. Appl. Phys.* **100,** 033716 (2006).

75 Sang, B.S., Nagoya, Y., Kushiya, K., Yamase, O., *Sol. Energy Mater. Sol. Cells* **75,** 179 (2003).

76 Malmstrom, J., Wennerberg, J., Stolt, L., *Thin Solid Films* **431-432,** 436 (2003).

77 Schmidt, M., Braunger, D., Schaffler, R., Schock, H.W., Rau, U., *Thin Solid Films* **361-362,** 283 (2000).

78 Yanagisawa, T., Kojima, T., Koyanagi, T., *Microelectronics Reliability* **44,** 229 (2004).

79 Pern, J., Sundaramoorthy, R., Dehart, C., Glynn, S., Li, X., Repins, I., Mansfield, L., Contreras, M., Noufi, R., Gessert, T., *NREL CIGS Cell-Level Reliability Task and Studies*, http://www1.eere.energy.gov/solar/pdfs/pvrw2010_poster_pern.pdf, May 22nd 2011.

80 Lin, W., Ma, R., Xuw, J., Kang, B., *Sol. Energ. Mat. Sol. C.* **91,** 1902 (2007).

81 Guillen, C., Herrero, J., *Surf. Coat. Tech.* **201,** 309 (2006).

82 Allsop, N.A., Hansel, A., Visbeck, S., Niesen, T.P., Lux-Steiner, M.C., Fischer, Ch.-H., *Thin Solid Films* **511-512,** 55 (2006).

83 Egerton, R.F., in E*lectron Energy-Loss Spectroscopy in the Electron Microscope*, (Springer, third edition, New York, 2011).

84 Mkhoyan, K.A., Babinec, T., Maccagnano, S.E., Kirkland, E.J., Silcox, J., *Ultramicroscopy* **107,** 345 (2007).

85 Mkhoyan, K.A., S.E. Maccagnano-Zacher, S.E., Kirkland, E.J., Silcox, J., *Ultramicroscopy* **108,** 791 (2008).

86 Green, M. A., Emery, K., Hishikawa, Y., Warta, W., *Prog. Photovoltaics* **18**, 346 (2010).

87 Jager-Waldau, A., *Sol. Energ. Mat. Sol. C.* **95**, 1509 (2011).

88 Siebentritt, S., Walk, P., Fiedeler, U., Lauermann, I., Rahne, K., Lux-Steiner, M. Ch., Niesen, T. P., Karg, F., *Prog. Photovoltaics* **12**, 333 (2004).

89 Beyer, W., Hupkes, J., Stiebig, H., *Thin Solid Films* **516**, 147 (2007).

90 Penn, F.J., Noufi, R., Li, X., DeHart, C., To, B., *Proceedings of the 33rd IEEE Photovoltaics Specialist Conference*, p.1, (2008).

91 Penn, F.J., Glick, S.H., Sundaramoorthy, R., To, B., Li, X., DeHart, C., Glynn, S., Gennett, T., Noufi, R., Gessert, T., *Proceedings of the 35th IEEE Photovoltaics Specialist Conference*, p.1166, (2010).

92 Penn, F.J., Glick, S.H., Li, X., DeHart, C., Gennett, T., Contreras, M., Gessert, T., *Proc. SPIE*, 7412, 74120K-I.

93 Swank, R.K., *Phys. Rev.* **153**, 844 (1967).

94 Gratzel, M., *Nature* **414**, 338 (2001).

95 Yamada, A., Matsubara, K., Sakurai, K., Ishizuka, S., Tampo, H., Fons, P.J., Iwata, K., Niki, S., *Appl. Phys. Lett.* **85**, 5607 (2004).

96 Kılıc, C., Zunger, A., *Appl. Phys. Lett.* **81**, 73 (2002).

97 Trani, F., Causà, M., Ninno, D., Cantele, G., Barone, V., *Phys. Rev. B* **77**, 245410 (2008).

98 Cox, D.F., Fryberger, T.B., Semancik, S., *Phys. Rev. B* **38**, 2072 (1988).

99 Jackson, P., Hariskos, D., Lotter, E., Paetel, S., Wuerz, R., Menner, R. Wischmann, W. Powalla, M. *Prog. Photovoltaics* **19**, 1894 (2011).

100 Baer, M., Repins, I., Contreras, M. A., Weinhardt, L. Noufi, R., Heske, C., *Appl. Phys. Lett.* **95**, 052106 (2009).

101 Green, M. A., Emery, K., Hishikawa, Y., Warta, W., *Prog. Photovoltaics* **20**, 12 (2012).

102 Wolden, C.A., Kurtin, J., Baxter, J. B., Repins, I., Shaheen, S. E., Torvik, J. T., Rockett, A.A., Fthenakis, V.M., Aydil, E.S., *J. Vac. Sci. Technol. A* **29**, 030801 (2011).

103 O'Brien, P., McAleese, J. *J. Mater. Chem.***8**, 2309 (1998).

104 Mokili, B., Charreire, Y., Cortes, R., Lincot, D., *Thin Solid Films* **288**, 21 (1996).

105 Nakada, T., Mizutani, M., Hagiwara, Y., Kunioka, A., *Sol. Energ. Mater. Sol. Cells* **67**, 255 (2005).

106 Contreras, M.A., Romero, M.J., Hasoon, B.T.E., Noufi, R., Ward, S., Ramanthan, K. *Thin Solid Films* **403**, 204 (2002).

107 Enriguez, J.P., Mathew, X., *Sol. Energ. Mater. Sol. Cells* **76**, 313 (2003).

108 Herrero, J., Gutierrez, M.T., Guillen, C., Dona, J.M., Martinez, M.A., Chaparro, A. M., Bayon, R., *Thin Solid Films* **361**, 28 (2002).

109 Sibentritt, S., *Sol. Energy* **77**, 767 (2004).

110 Dona, J.M., Herrero, J., *J. Electrochem. Soc.***144**, 4081 (1997).

111 Ruffner, J.A., Hilmel, M.D., Mizrahi, V., Stegeman, G.I., Gibson, U., *J. Appl. Opt.* **28**, 5209 (1989).

112 Aboundi, A., Diblasio, M., Bouchara, D., *Phys. Rev. B* **50,** 11677 (1994).

113 Nakada, T., *Thin Solid Films* **346,** 361 (200).

114 Xian, H., Benalloul, P., Barthou, C., Benoit, J., *Thin Solid Films* **248**, 193 (1994).

115 Goto, F., Ichimura, M., Arai, E., *Jpn. J. Appl. Phys.* **36**, 1146 (1997).

116 Kavanagh, Y., Alam, M. J., Cameron, D. C., *Thin Solid Films* **85**, 447 (2004).

117 Bakke, J.R., Jung, H.J., Tanskanen, J.T., Sinclair R., Bent, S.F., *Chem. Mater.* **22,** 4669 (2010).

118 Nakada, T., Mizutani, M., *28th IEEE Photovoltaic Specialist Conference*, 529 (2000).

119 Chu, T.L., Chu, S.S., Britt, J., Ferekides, C., Wu, C.Q., *J. Appl. Phys.***70**, 2688 (1991).

120 Tanaka, K., Minemoto, T., Takakura, H., *Sol. Energy* **83,** 477 (2009).

121 Herz, K., Ericke, A., Kessles, F., Wachter, R., Powalla, M., *Thin Solid Films* **431-432**, 392 (2003).

122 Li, Z. Q., Shi, J. H., Liu, Q. Q., Wang, Z. A., Sun, Z., Huang, S. M., *Appl. Surf. Sci.* **257**, 122 (2010).

123 Vallejo, W., Hurtado, M., Gordillo, G., *Electrochimica Acta* **55**, 5610 (2010).

124 Islam, M. M., Ishizuka, S., Yamada, A., Sakurai, K., Niki, S., Sakurai, T., Akimoto, K., *Solar Energ. Mater. Sol. Cells* **93**, 970 (2009).

125 Gal, D., Hodes, G., Hariskos, D., Braunger, D., Schock, H.-W., *Appl. Phys. Lett.* **73,** 3135 (1998).

126 Song, J., Li, S.S., Chen, L., Noufi, R., Anderson, T. J., Crisalle, O.D., *Photovoltaic Energy Conversion, Conference Record of the 2006 IEEE 4th World Conference*, p.1, 534, (2006).

127 Gloeckler, M., Sites, R. S., *Thin Solid Films* **480-481**, 241 (2005).

128 Padam, G.K., Malhotra, G.L., Rao., S.U.M., *J. Appl. Phys.* **63**, 770 (1998).

129 Zhang, Y., Dang, X. Y., Jin, J., Yu, T., Li, B. Z., He, Q., Li, F. Y., Sun, Y., *Appl. Surf. Sci.* **256**, 6871 (2010).

130 Dona, J. M., Herrero, J., *J. Electrochem. Soc.***141**, 205 (1994).

131 Kaur, L., Pandya, D.K., Chopra, K.L., *J. Electrochem, Soc.* **127**, 943 (1980).

132 Naghavi, N., Hubert, C., Etchberry, A., Bermudez, V., Hariskos, D., Powalla, M., Linot, D., *Prog. Photovolt. Res. Appl.* **17,** 1 (2009).

133 Hodes, G., *Chemical Solution Deposition of Semiconductor Films,* (Marker Dekker Inc., New York, 2003).

134 Wright, K., Gale, J.D., *Phys. Rev. B.* **70**, 035211 (2004).

135 Nakada, T., Mizutani, M., Hagiwara, Y., Kunioka, A., *Sol. Energy Mater. Sol. Cells* **67,** 255 (2001).

136 Guo, Q, Ford, M. G., Yang, W.-C., Walker, B., Stach, E. A., Hillhouse, H. W., Agrawal, R., *J. Am. Chem. Soc.* **132**, 17384 (2010).

137 Chamberlin, R. R., Skarman, J. S., *J. Electrochem. Soc.* **113**, 86 (1966).

138 McPeak, K.M., Opasanont, B., Shibata, T., Ko, D.-K., Becker, M.A., Chattapadhyay, S., Bui, H. P., Beebe, T.P. Jr., Bunker, B.A., Murray, C.B., Baxter, J. B., *Chem. Mater.* 25, 297 (2013).

139 Bai, G., Bee, J. S., Biddlecombe, J. G., Chen, Q., Leach, W. T., *Int. J. Pharm.* **423**, 264 (2012).

140 Halasz, G., Gyure, B., Janosi, I. M., Szabo, K. G., Tel, T., *Am. J. Phys.* **75**, 1092 (2007).

141 Barkhouse, D.A.R., Gunawan, O., Gokmen, T., Todorov, T.K., Mitzi, D.B., *Prog. Photovoltaics* **20**, 6 (2012).

142 Wang, K., Gunawan, O., Todorov, T., Shin, B., Chey, S.J., Bojarczuk, N.A., Mitzi, D., Guha, S., *Appl. Phys. Lett.* **97**, 143508 (2010).

143 Repins, I., Beall, C., Vora, N., DeHart, C., Kuciauskas, D., Dippo, P., To, B., Mann, J., Hsu, W.-C., Goodrich, A., Noufi, R., *Sol. Energy Mater. Sol. Cells* **101**, 154 (2012).

144 Katagiri, H., Sasaguchi, N., Hando, S., Hoshino, S., Ohashi, J., Yokota, T., *Sol. Energy Mater. Sol. Cells* **49**, 407 (1997).

145 Katagiri, H., Jimbo, K., Maw, W.S., Oishi, K., Yamazaki, M., Araki, H., Takeuchi, A., *Thin Solid Films* **517**, 2455 (2009).

146 Cheng, A.-J , Manno, M., Khare, A., Leighton, C., Campbell, S., Aydil, E.S., *J. Vac. Sci. Technol. A* **29**, 051203 (2011).

147 Hillhouse, H.W., Beard, M.C., *Curr. Opin. Colloid Interface Sci.* **14**, 245 (2009).

148 Akhavan, V.A., Goodfellow, B.W., Panthani, M.G., Steinhagen, C., Harvey, T.B., Stolle, C.J., Korgel, B.A., *J. Solid State Chem.* **189**, 2 (2012).

149 Guo, Q., Hillhouse, H.W., Agrawal, R., *J. Am. Chem. Soc.* **131**, 11672 (2009).

150 Riha, S.C., Parkinson, B.A., Prieto, A.L., *J. Am. Chem. Soc.* **131**, 1254 (2009).

151 Steinhagen, C., Panthani, M.G., Akhavan, V., Goodfellow, B., Koo, B., Korgel, B.A., *J. Am. Chem. Soc.* **131**, 12554 (2009).

152 Khare, A., Wills, A.W., Ammerman, L.M., Norris, D.J., Aydil, E.S., *Chem. Commun.* **47**, 11721 (2011).

153 Narayan, S., Muldoon, J., Finn, M.G., Fokin, V.V., Kolb, H.C., Sharpless, K.B., *Angrew. Chem. Int. Ed.* **44,** 3275 (2005).

154 Nag, A., Kovalenko, M.V., Lee, J.S., Liu, W., Spokoyny, B., Talapin, D.V., *J. Am. Chem. Soc.* **133**, 10612 (2011).

155 Pein, A., Baghbanzadeh, M., Rath, T., Haas, W., Maier, E., Amenitsch, H., Hofer, F., Kappe, C.O., Trimmel, G., *Inorg. Chem.* **50**, 193 (2011).

156 Dale, P., Peter, L., in *Photoelectrochemical Materials and Energy Conversion Processes*, Volume 12, Alkire, R.C., Kolb, D.M., Lipkowski, J., Ross, P.N., Ed. (Wiley-VCH Verlag GmbH & Co. KGaA, Weinheim, Germany, 2010), chap. 1.

157 Scragg, J.J., in *Copper Zinc Tin Sulfide Thin Films for Photovoltaics: Synthesis and Characterization by Electrochemical Methods*, (Springer-Verlag Berlin Heidelberg, 2011), chap. 1.

158 Tanaka, T., Kawasaki, D., Nishio, M., Gu, Q. X., Ogawal, H., *Phys. Status Solidi C* **3 (8)**, 2844 (2006).

159 Ennaoui, A., Lux-Steiner, M., Weber, A., Abou-Ras, D., Kotschau, I., Schock, H.W., Schurr, R., Holzing, A., Jost, S., Hock, R., Voss, T., Schulze, J., Kirbs, A., *Thin Solid Films* **517**, 2511 (2009).

160 Han, J., Shin, S.W., Gang, M.G., Kim, J.H., Lee, J.Y., *Nanotechnology* **24**, 095706 (2013).

161 Bodeg Ård, M., Granath, K., Stolt, L., *Thin Solid Films* **361-362**, 9 (2000).

162 Rockett, A., Britt, J.S., Gillespiec, T., Marshall, C., Al Jassim, M. M., Hasoon, F., Matson, R., Basole, B., *Thin Solid Films* **372**, 212 (2000).

163 Scragg, J.J., Ericson, T., Kubart, T., Edoff, M., Platzer-Björkman, C., *Chem. Mater*. **23**, 4625 (2011).

164 Scragg, J.J., Watjen, J.T., Edoff, M., Ericson, T., Kubart, T., Platzer-Björkman, *J. Am. Chem. Soc.* **134,** 199330 (2012).

165 Thimsen, E., Barysley, S.B., Martison, A.B.F., Elam, J.W., Veryovkin, I.V., Pellin, M.J., *Chem. Mater*. **25**, 313 (2013).

166 Weber, A., Krauth, H., Perlt, S., Schubert, B., Kotschau, I., Schorr, S., Schock, H.W., *Thin Solid Films* **517,** 2524 (2009).

167 Weber, A., Mainz, R., and Schock, H.W., *J. Appl. Phys.* **107**, 013516 (2010).

168 Redinger, A., Berg, D.M., Dale, P.J., and Siebentritt, S., *J. Am. Chem. Soc.* **133**, 3320 (2011).

169 Friedlmeir, T.M., Wieser, N., Walter, T., Dittrich, H., Schock, H.W., Proc. 14th PVSEC, P4B.10, (1997).

170 Jimbo, K., Yamada, S., Kamimura, T., Maw, W.S., Katagiri, H., Fukano, T., Ito, T., Motohiro, T., Proc. 22nd EUPVSEC, 3BV.5.16, (2007).

171 Chernomordik, B.D., Aydil, E.S., *under preparation* (2013).

172 Fernandes, P.A., Salome, P.M.P., da Cunha, A.F., *J. Alloy. Compd.* **509**, 7600 (2011).

173 Li, H., Zhang, Q., Yap. C.C.R., Tay, B.K., Edwin, T.H.T., Oliver, A., and Baillargeat, D., *Adv. Funct. Mater.* **22**, 1385 (2012).

174 Windom, B.C., Sawyer, W.G., Hahn, D.W., *Tribol Lett*. **42,** 301 (2011).

175 Sharma, B.R., Chang, Y.A., *Bulletin of Alloy Phase Diagrams* **7**, 3 (1986).

176 Piacente, V., Foglia, S., Scarda, P., *J. Alloy. Compd.* **177,** 17(1991).

177 Luther, J.M., Law, M., Song, Q., Perkins, C.L., Beard, M.C., Nozik, A.J., *ACS Nano* **2**, 271 (2008).

178 Wu, N., Fu, L., Su, M., Aslam, M., Wong, K.C., Dravid, V.P., *Nano Lett.* **4**, 383 (2004).

179 Shukla, N., Liu, C., Jones, P.M., Weller, D., *J. Magn. Magn. Mater.* **266,** 178 (2003).

180 Thistlewaite, P.J., Hook, M.S., *Langmuir* **16**, 4993 (2000).

181 Efrat, R., Abramov, Z., Aserin, A., Garti, N., *J. Phys. Chem. B* **114**, 10709 (2010).

182 Gopiyron, A., Devillepin, J., Novak, A., *J. Raman Spectrosc.* **9**, 297 (1980).

183 Senna, T., Ikemiya, N., Ito, M., *J. Electroanalytical Chem.* **511**, 115 (2011).

184 El-Kabbany, E., Said, G., Badr, Y., Taha, S., *Phys. Sat. Sol. (a)* **67**, 339 (1981).

185 Baran, J., *J. Mol. Struct.* **172**, 1 (1988).

186 Sawatari, Y., Sueoka, T., Shingaya, Y., Ito, M., *Spectrochimica Acta* **50A**, 1555 (1994).

APPENDIX I

Chapter 7: Supporting Information

Figure AI.1 shows the spatial variation of the film thickness and digital photographs of $Zn_xCd_{1-x}(S,O)$ films are deposited by CF-CBD with and without EDTA. The thickness of the alloy films decrease with increasing Cd^{+2} concentration in the solution, because the total metal ion concentration decreases as the relative Cd^{2+} ion concentration increases.

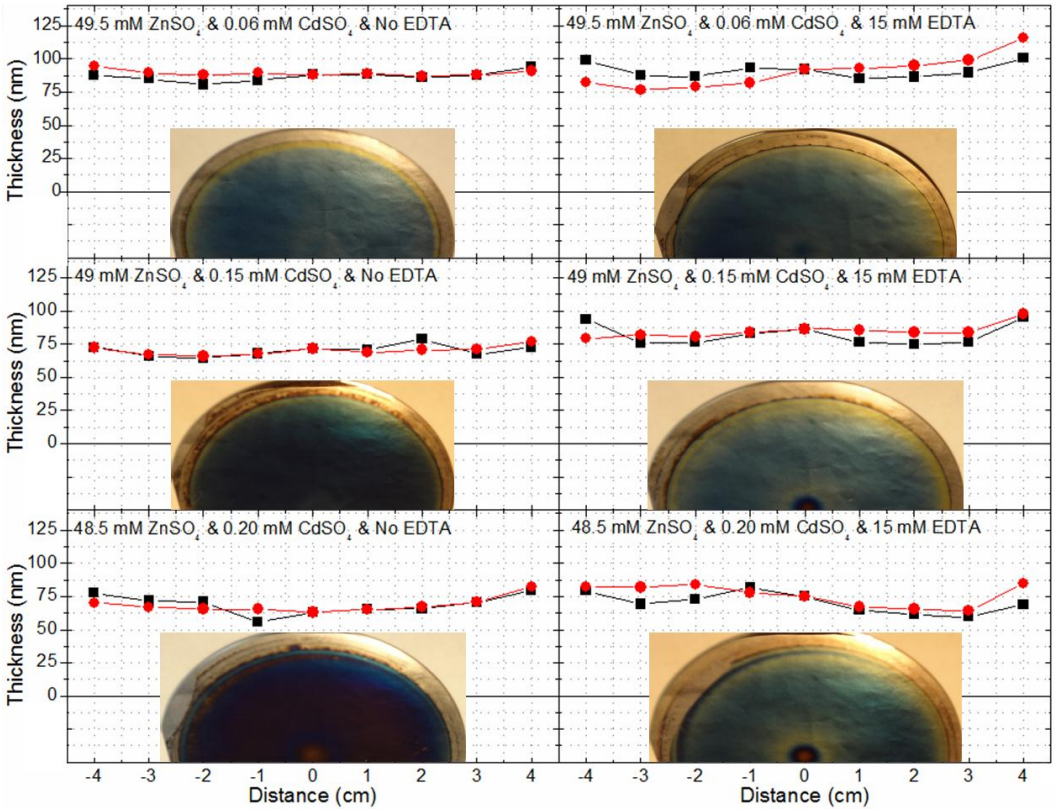

Figure AI.1. The spatial variation of the film thickness from $Zn_xCd_{1-x}S$ films deposited using CF-CBD at 85 °C with **(a)** 49.5 mM $ZnSO_4$ and 0.05 mM $CdSO_4$, **(b)** 49.0 mM $ZnSO_4$ and 0.15 mM $CdSO_4$, **(c)** 48.5 mM $ZnSO_4$ and 0.20 mM $CdSO_4$ with no EDTA in the solution, and **(d)** 49.5 mM $ZnSO_4$ and 0.05 mM $CdSO_4$, **(e)** 49.0 mM $ZnSO_4$ and 0.15 mM $CdSO_4$, **(f)** 48.5 mM $ZnSO_4$ and 0.20 mM $CdSO_4$ with 15 mM EDTA in the solution.

The total thicknesses of the CF-CBD grown $Zn_{0.88}Cd_{0.12}S$ alloy deposited at 85 °C using 49.0 mM $ZnSO_4$, 0.15 mM $CdSO_4$, and 15 mM EDTA in the deposition solution are also confirmed by the cross-sectional scanning electron microscopy, Figure AI.2.

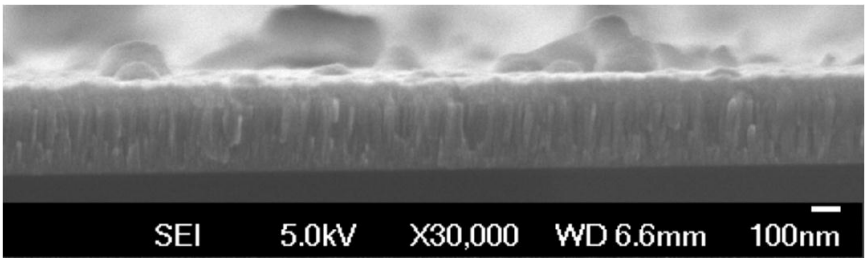

Figure AI.2. Cross sectional scanning electron micrograph from CF-CBD grown $Zn_{0.53}Cd_{0.47}(S,O)$ films deposited at 85 °C using 49.0 mM $ZnSO_4$, 0.15 mM $CdSO_4$, and 15 mM EDTA in the solution.

Films deposited with CF-CBD, Figure AI.3 and AI.4, also showed uniform spatial composition profiles. Below, in Figure AI.3, the Auger depth profiles from two different locations of $Zn_{0.88}Cd_{0.12}(S,O)$ film deposited with EDTA in the CF-CBD solution shows the same elemental profile, even though the film in the edge region is thicker. Similarly, uniform spatial elemental profiles are also observed in $Zn_{0.53}Cd_{0.47}(S,O)$, Figure AI.4.

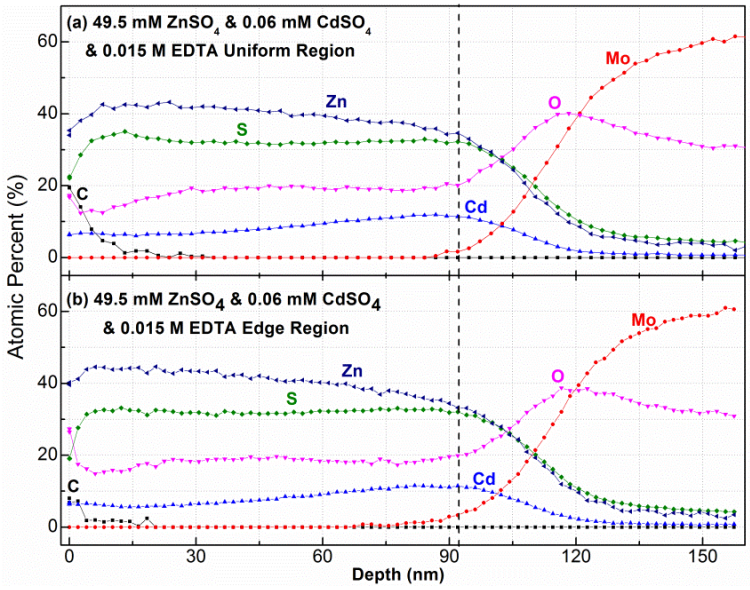

Figure AI.3. Auger depth profiles from CF-CBD grown $Zn_{0.88}Cd_{0.12}(S,O)$ films deposited at 85 °C at **(a)** the center, and **(b)** the edge of the substrate.

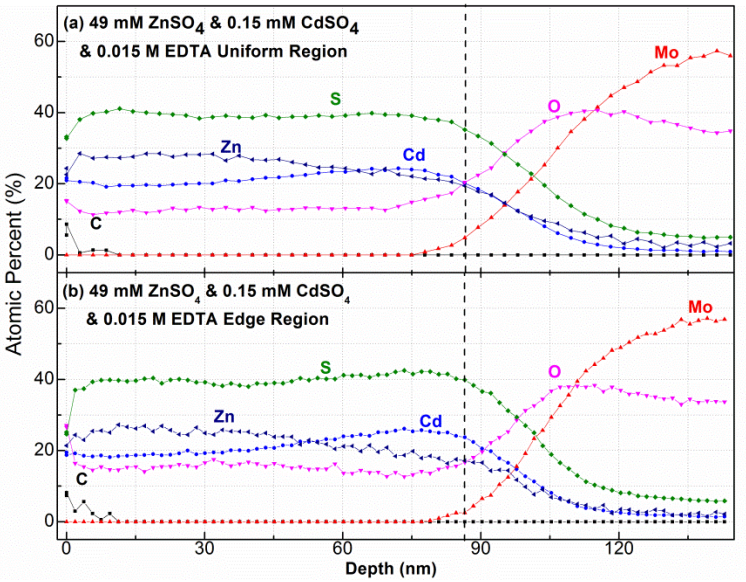

Figure AI.4. Auger depth profiles from CF-CBD grown $Zn_{0.53}Cd_{0.47}(S,O)$ films deposited at 85 °C at **(a)** the center, and **(b)** the edge of the substrate.

APPENDIX II

Chapter 8: Supporting Information

Experimental Procedures

Extraction **-** The CZTS nanocrystals were synthesized as described by Khare *et al.* (reference 14 in the manuscript) and dispersed in toluene. Typically, ~10 ml of oleic acid was added to the toluene dispersion to increase the shelf life of the dispersion in toluene. To extract these nanocrystals into formamide, 2 mL of formamide was mixed with either 100 µL of 1.28 g/mL or 150 µL of 1.92 g/mL K_2S solution in deionized water and added to 1 mL of CZTS nanocrystals (~ 2 mg/mL) dispersed in toluene. The two different amounts of K_2S correspond to 0.061 and 0.134 g/ml K_2S concentration in the polar solvent phase (> 93% by volume formamide and <7% by volume water). The two-phase mixture was stirred vigorously for 20, 60 or 180 minutes. In some experiments, we also carried out this step up to 16 hours. The transfer of nanocrystals to the formamide phase was detected visually. The solution with the CZTS nanocrystals appears black. While the formamide phase begins to get darker after stirring for 20 minutes, a thick emulsion remains visible between the polar and nonpolar phases, indicating incomplete extraction. Stirring longer slowly thins the emulsion and the formamide phase gets darker. After the stirring is stopped 1 mL toluene is added to the mixture and the polar and non-polar phases are allowed to separate by letting the vial sit for 5 minutes. Separation and breaking of the emulsion is easier for those extractions where the mixture has been stirred for one hour or longer. Emulsion completely disappears if the stirring is carried out for 16 hours. We believe that the nanocrystals covered with both alkly ligands and S^{2-} stabilizes the emulsion at the toluene-formamide interface. When the nanocrystals are mostly covered with S^{2-} they prefer to transfer to the formamide phase and the

emulsion breaks up. Following, the toluene phase is removed from the top using a pipette and the nanocrystals are separated by precipitation from formamide containing K_2S by the addition of 2 mL of acetonitrile and centrifuging. The supernatant is decanted and the particles are redispersed in 2 ml of fresh formamide by vortexing and sonicating for a minute, each. This is the first step of the cleaning procedure. In a second cleaning step, the CZTS nanocrystals are again precipitated out of formamide by the addition of 2 mL each of acetonitrile, acetone and toluene. The liquid phase is decanted after centrifugation, and the nanocrystals are redispersed in 2 ml of formamide. This cleaning step can be repeated as many as six times and removes excess K_2S. In the final step, the particles are dispersed either in formamide or DI water by sonication.

XRD and Raman Characterization - The nanocrystals are drop cast and dried on bare or molybdenum-coated Si (100) substrates for structural characterization with X-Ray Diffraction (XRD) and Raman spectroscopy. The drop-cast CZTS nanocrystal films from toluene were dried in air, at ambient conditions, while the nanocrystal films cast from formamide and DI water were dried in vacuum at ambient temperature. The nanocrystal films cast from formamide were dried for 10 hours, while those cast from DI water were dried for 1 hour. Even when the films after cast from dispersions that were prepared by cleaning the nanocrystals three times, there is still excess K_2S in the dispersions and one could observe K_2S crystals on the CZTS nanocrystal films. These crystals were removed by rinsing the film with ~10 mL of DI water and drying the film again in vacuum before all XRD and Raman measurements.

Raman Spectra were collected using a Witec Alpha300 R confocal Raman microscope. Raman scattering from an Argon ion laser (514.5 nm) was collected using a UHTS300 spectrometer that consisted of a monochromator with 1800 lines/mm grating and a DV401 CCD detector. Accumulation time was 1 second per frameand the scattered intensity was integrated for 10 frames with 0.02 cm^{-1} spectral resolution.

XRD patterns from drop cast films were collected and recorded using a Bruker-AXS microdiffractometer equipped with a Cu-Kα X-ray source using 0.8 mm spot size.

Transmission Electron Microscopy – CZTS suspensions (0.03 mg/ml) were dropcast on carbon grids for Transmission Electron Microscopy (TEM) characterization. The specimen grids were stored overnight under 10^{-8} Torr vacuum to remove the residual solvent prior to loading the grids into the microscope. Transmission electron microscopy (TEM) analysis was conducted using an FEI Tecnai F-30 microscope with a Schottky field-emission electron gun operated at 200 keV.

Attenuated Total Reflection Fourier Transform Infrared Spectroscopy (ATR-FTIR) - The ligand coverage on the surfaces of the CZTS nanocrystals was determined using ATR-FTIR spectroscopy. The spectra were collected using Nicolet Magna 550 Spectrometer equipped with an ATR-FTIR attachment (Harrick Scientific). Fixed and identical volumes (~300 µL) of colloidal CZTS suspensions in identical concentrations (~2 mg/mL) were cast onto a trapezoidal-shaped (45^{o} bevels) Ge ATR crystal ($5 \times 1 \times 0.1$ cm^3) and allowed to dry until all the solvent phase infrared absorptions disappeared and the nanocrystal films appeared dry. For NC films cast from dispersions in water and toluene, this typically took 1 hour. For NC films cast from dispersions in formamide, the Ge ATR crystal was dried in vacuum overnight. Spectra were collected in the differential mode where the spectrum of the NC film is referenced with respect to the spectrum of the bare ATR crystal. In all cases enough nanoparticles were put on the ATR crystal such that the entire surface of the crystal (5 cm^2) was covered with a NC film and the film thickness was much larger than the penetration depth of the infrared radiation at 1000 cm^{-1} and above. That the film thickness had reached sufficient thickness was checked by doubling the NCs on the film and observing that the infrared spectrum and the intensities changed less than ~5%.

Absolute surface coverage of the ligands was estimated as follows. The absorbance of the ligand (oleic acid and oleylamine) was recorded by forming a liquid film on the Ge ATR crystal. When the film is thicker than the penetration depth the absorbance is given by

$$A_\ell = N_\ell \varepsilon A_{ATR} d_p^\ell \tag{AII.1}$$

where A_ℓ is the absorbance of the liquid, N_ℓ is the concentration of the liquid (*e.g.*, $N_\ell = 1.83\times10^{21}$ molecules/cm^3 for oleylamine and $N_\ell = 1.91\times10^{21}$ molecules/cm^3 for oleic acid), ε is the absorptivity, A_{ATR} is the surface area of the ATR crystal and d_p^ℓ is the infrared penetration depth into the liquid. For a nanocrystal film cast on to the ATR crystal

$$A_{NC} = N_s \varepsilon A_p \tag{AII.2}$$

where A_{NC} is the absorbance of the ligands on the nanocrystals surface, N_s is the surface coverage of ligands per unit area and A_p is the total surface area of the nanocrystals. Assuming spherical nanocrystals with radius r and a solid packing fraction, f_s, equation 2 can be written as

$$A_{NC} = \frac{3N_s f_s \varepsilon A_{ATR} d_p^{NC}}{r} \tag{AII.3}$$

where d_p^{NC} is the infrared penetration depth into the nanocrystal film. Both A_{NC} and A_ℓ are experimentally measurable quantities at characteristic absorption frequencies of the ligand molecules. Taking the ratio of equations 1 and 3 and assuming that the absorptivity of the ligand in liquid and when it is adsorbed onto the nanocrystal surface are the same, one obtains an expression for the surface coverage of the ligand molecules as

$$N_s = \frac{N_\ell A_{NC} r d_p^\ell}{3 A_\ell f_s d_p^{NC}}. \quad \text{(AII.4)}$$

The penetration depth in film *i* depends on the absorption wavelength, λ and the refractive index of the film, n_i, and can be calculated from

$$d_p^i = \frac{\lambda}{2\pi n_{Ge}\sqrt{\sin^2\theta - (n_i / n_{Ge})^2}} \quad \text{(AII.5)}$$

where λ is the total internal reflection angle. The refractive index of the nanocrystal film, n_{Ge}, is also a function of the packing fraction and can be calculated by assuming that it is a mixture of voids and CZTS using the Bruggeman effective medium theory. Thus, the only unknown in equation 4 is the solid packing fraction, f_s, which determines the quantity $d_p^\ell / f_s d_p^{NC}$. This quantity is plotted as a function of the solid packing fraction, f_s in Figure AII.1 for Ge as the ATR crystal. If the nanocrystals pack randomly then solid packing fraction is 0.63 and the quantity $d_p^\ell / f_s d_p^{NC}$ is 1.35. Thus, the surface coverage in ligand molecules per unit area can be calculated from

This

$$N_s = 0.45 N_\ell r \frac{A_{NC}}{A_\ell} \quad \text{(AII.6)}$$

A fractional coverage can be estimated by dividing this value by the site density of either the cations or the anions on (001) planes, 6.8×10^{14} cm^{-2}.

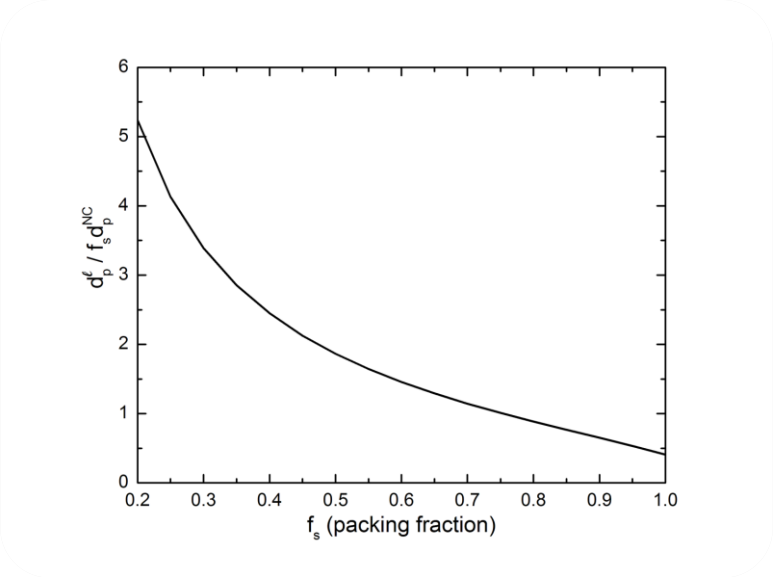

Figure AII.1. The quantity $d_p^{\ell} / f_s d_p^{NC}$ in equation 4 as a function of the solid packing fraction, f_s.

Dynamic Light Scattering Measurements (DLS) – Nanocrystal size distributions were determined using dynamic light scattering (Brookhaven ZetaPLUS) after diluting the typical dispersions to 0.1 mg/ml. The light wavelength was 657 nm and scattering was collected perpendicular to the laser propagation direction. Ten independent 45-second long consecutive measurements were combined to obtain the final log-normal size distributions shown in Figure AII.2.

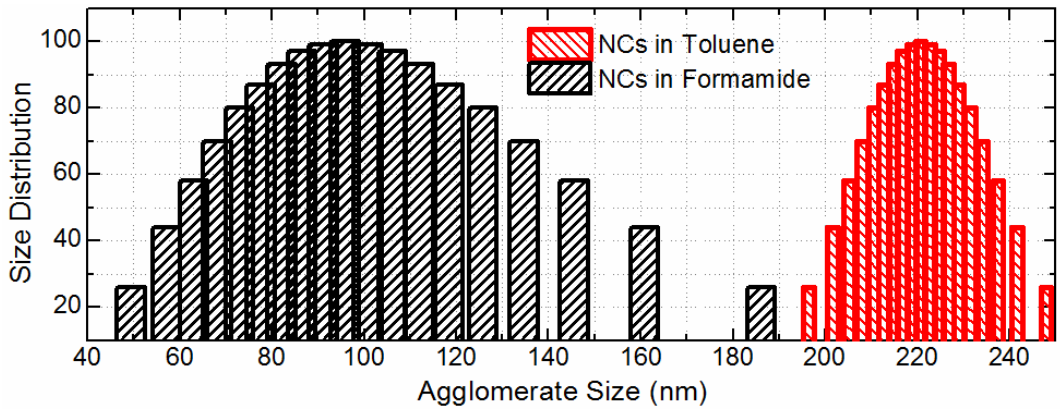

Figure AII.2. The size distributions of CZTS nanocrystals dispersed in toluene, before extraction and in formamide, after extraction.

Infrared Absorption Assignments – The major infrared absorptions in Figure 8.5 can be assigned to vibrations in K_2SO_4, $KHSO_4$ and in CH_2 and CH_3 groups in the oleic acid ligands that remain on the surface even after extraction into the polar solvent. Figure AII.3 shows the locations of these major absorptions and Table AII.1 lists their respective assignments based on literature. This data indicates that the surface of the air-dried CZTS nanocrystal is comprised of a combination of K_2SO_4, $KHSO_4$ in addition to the remaining oleic acid ligands.

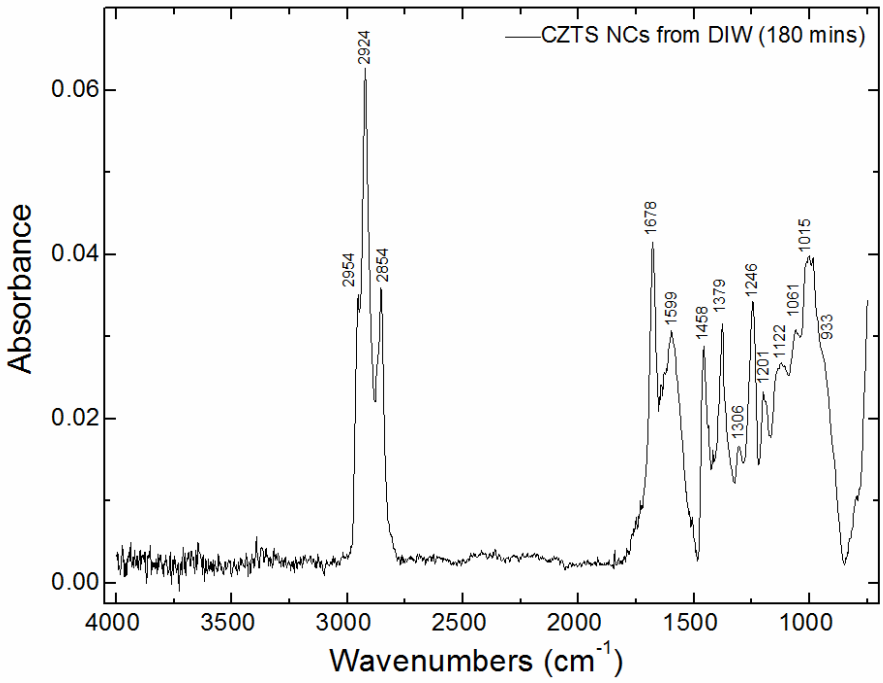

Figure AII.3. ATR-FTIR spectra of the CZTS nanocrystals drop cast from DI water with major infrared absorption peaks identified.

Table AII.1. Infrared absorption peak assignment for CZTS nanocrystals cast from water dispersions (See also Figure AII.3)

This Work (cm^{-1})	Literature value[reference]	Assignment
2954	2954[177-180]	C-H stretching in CH_3 in oleic acid and oleylamine
2924	2922[177-180]	C-H asymmetric stretch in CH_2 in oleic acid and oleylamine
2854	2854[177-180]	C-H symmetric stretch in CH_2 in oleic acid and oleylamine
1678	1647,[179] 1650[180]	C=O stretching of oleic acid and possible contribution from C=C stretching
1599	1450-1700[178,179]	Asymmetric stretch of the COO^- metal bidentate on the CZTS surface, possible contribution from oleylamine NH_2 scissoring mode at 1590-1600
1458	1463[180]	CH_2 deformation (δ) modes in oleic acid ligands
1379	1379[181]	CH_3 umbrella mode in oleic acid
1306	1292-1326[181]	SO asymmetric stretching in $KHSO_4$
1246	1255[181,182]	S-OH plane bending in $KHSO_4$
1201	1200[181,182]	Asymmetric SO_3 vibrations in HSO_4
1122	1080-1125[181-186]	Asymmetric SO_4 stretching in K_2SO_4 and $KHSO_4$
1061	1060[185,186]	Symmetric stretching of SO_4 group in $KHSO_4$
1015	1015[185,186]	Symmetric stretching of SO_4 group in $KHSO_4$
930	932[184,185]	Symmetric stretching of SO_4 group in $KHSO_4$ and K_2SO_4